ABSTRACT

Title of Document: APPLICATIONS OF MULTIPHOTON IMAGING TECHNIQUES TO THE STUDY OF PROTEIN INTERACTIONS.

Tilman Rosales, Ph.D., 2009

Directed By: Prof. Robert A. Walker
Dept of Chemistry and Biochemistry

Several recent improvements in microscopy have been driven by advances in ultrafast laser technology. The goal of the research described in this dissertation was to develop noninvasive, optically based methods to measure the mobility of macromolecules in biologically relevant systems. These methods exploit advances in ultrafast laser science and recent developments in multiphoton spectroscopy techniques. Each of the techniques described in this dissertation is validated and standardized using well characterized systems. We have explored the following techniques: First, 2-photon 2-color Fluorescence Cross Correlation Spectroscopy (FCCS) a powerful technique to measure dilute protein interactions in living cells. We have used FCCS to probe AR-Tif2

(Androgen Receptor - activating cofactor) interactions in the presence of casodex, an antagonist yielding decreased binding affinity.

On a much faster timescale, exploring rotational rather than translational diffusion, we used molecular dynamics simulations of the model probe perylene to show that there is 'room to wiggle' (sub-ps libration) within pure hexadecane.

Third, combining picosecond and microsecond scales, we built a system to measure both rotational and translational motion in one experiment, using advanced Time Correlated Single Photon Counting (TCSPC) techniques. We have tested our ability to measure and link simultaneously the translational rates and decay rates of Alexa488 dye and other biologically relevant fluorophores.

Next, exploiting non-linear vibrational spectroscopy, we have imaged the non-fluorescent molecule NAD^+ in DPPC vesicles, the C-H stretch of lipids in vesicles and polystyrene beads, and the O-H stretch of water inside living cells (vs. O-D) to demonstrate the chemically selective imaging capabilities of Coherent Anti-Stokes Raman Spectroscopy (CARS) Microscopy.

Most recently, we have built a STED (STimulated Emission Depletion) Microscope capable of extracting fluorescent images well below the diffraction limit. The STED microscope was tested using both 170nm fluorescent beads and a novel photochromic dye.

APPLICATIONS OF MULTIPHOTON IMAGING TECHNIQUES TO THE STUDY OF PROTEIN INTERACTIONS.

By

Tilman Rosales

Dissertation submitted to the Faculty of the Graduate School of the
University of Maryland, College Park, in partial fulfillment
of the requirements for the degree of
Doctor of Philosophy
2009

Advisory Committee:
Professor Robert A Walker, Chair
Dr. Jay R. Knutson, Ph.D. NIH advisor
Professor Michael Coplan
Professor Daniel Falvey
Professor Dorothy Beckett, Dean's Representative

Dedication

To my mom and Irene

Acknowledgements

I would like to thank my NIH advisor, Dr. Jay Knutson, for the great opportunity he has given me to work in his lab. Also, for believing in me and the leeway he gave me in selecting projects and performing experiments. He has been a great mentor and great inspiration to always look at the "big picture." On a lighter note, I would like to thank him for snapping my left kneecap back into place a few years ago after I slipped while pushing a rather large crate with a laser inside.

I thank my advisor, Dr. Robert Walker, for all his very insightful advice and the time that he has put in converting a jumble of different works into my dissertation document. I am sorry that we didn't get a chance to jog together (not that I would be able to keep up). I would also like to thank Dr. Cathy Royer (INSERM, France) for all her advice, patience and for "teaching me how to curse" (in English) when using FCS. I would also like to thank Dr. Jianhua Xu, for all the time spent teaching me laser "stuff." And I hope that he didn't mind all the time we spent re-aligning after "accidental" bumps to the occasional mirror. Also, I would like to thank my committee, Dr. Michael Coplan, Dr. Dorothy Beckett and Dr. Daniel Falvey for their insights, discussions of the findings and careful consideration of this research.

I would like to thank Dr. Christian Combs and Dr. Aleksandr Smirnov for helping with the initial setup of the FCS system. Also, I would like to thank Dr. Zuqin Nie and Dr. David Levens (National Cancer Institute) for the use of eGFP labeled c-myc protein mouse embryo fibroblast cells in the FCS experiments. Special thanks go to Dr. Xiongwu Wu and Dr. Milan Hodoscek for starting me with the molecular dynamics and quantum mechanical simulations. Many thanks to Dr. Lesley Davenport and her lab at CUNY

(Brooklyn College) for her 6MI labeled DNA samples and NAD^+/NADH filled vesicles used in experiments for this dissertation. I would like to thank Dr. Ling Yi and Dr. Venkatesan (National Institute for Allergy and Infectious Diseases) for providing HeLa cells used in CARS imaging experiments and general cell culture advice.

Lastly, I would like to thank my partner, Irene and my parents for their encouragement and support, my sister and brother who have always been an inspiration.

Table of Contents

List of Tables

List of Figures

List of Abbreviations

ACF	Auto-Correlation Function
ADH	Alcohol Dehydrogenase
AR	Androgen Receptor
CARS	Coherent Anti-Stokes Raman Spectroscopy
CFP,GFP,YFP	Cyan/Green/Yellow Fluorescent Protein
CHARMM	CHemistry at Harvard Molecular Mechanics
CSLM	Confocal Scanning Laser Microscope
D_r	rotational diffusion coefficient
D_t	translational diffusion coefficient
E-CARS	Epi-detected Coherent Anti-Stokes Raman Spectroscopy
eCFP, eGFP,eYFP	Enhanced Cyan/Green/Yellow Fluorescent Protein
F-CARS	Forward (trans)-detected Coherent Anti-Stokes Raman Spectroscopy
FCCS	Fluorescence Cross-Correlation Spectroscopy
FCS	Fluorescence Correlation Spectroscopy
FIFO	First-In First-Out
FLIM	Fluorescence Lifetime Imaging Microscopy
FM-CARS	Frequency Modulated Coherent Anti-Stokes Raman Spectroscopy
FRET	Förster Resonance Energy Transfer
GUI	Graphical User Interface

IBA	Iso-butyramide
ICS	Image Correlation Spectroscopy
IR	Infra Red
MD	Molecular Dynamics
MEF	Mouse Embryo Fibroblast
NAD^+	Nicotinamide Adenine Dinucleotide
NADH	reduced form of Nicotinamide Adenine Dinucleotide
NIR	Near-Infra Red
NR	Nuclear Receptor
PCH	Photon Counting Histogram
RESOLFT	Reversible Saturable Optically Linear (Fluorescence) Transition
RICS	Raster scanning Image Correlation Spectroscopy
SHG	Second Harmonic Generation
STED	STimulated Emission Depletion
THG	Third Harmonic Generation
TM	Transition Moment
TPFCS	Two-Photon excitation Fluorescence Correlation Spectroscopy
TPTCFCCS	Two-Photon, Two-Color Fluorescence Cross Correlation Spectroscopy
TREA	Time Resolved Emission Anisotropy
TTR	Time-Tag Recording

Chapter 1: Introduction

1.1. Historical Background

In the 1700s Robert Hooke used his 'looking glass' to observe "minute objects"[1,2] by focusing light of an oil lamp to illuminate his sample of cork tissue. He was the first to observe and coin the term "cell" for this tissue since the structures resembled monks' quarters or cells. During the same period, Anthony van Leeuwenhoek observed 'minute worms' in pepper water[3]. Their detailed descriptions using these revolutionary instruments (at the time) started the field of microscopy. With continued advances in optics, microscopes have become indispensable tools for scientists. In the realm of molecular biophysics, microscopy is addressing questions about cell functions and mechanisms, about how cells can be observed without disruption to cellular processes and how small an object can be resolved under a microscope. Currently, the new frontiers in microscopy are defined by increasing the specificity and sensitivity of molecular tags, decreasing or removing the invasiveness of such tags and improving instrumental spatial and temporal resolution through the development of new techniques.

One of the great advances in microscopy was the ability to first stain and later tag particular structures (or cellular species) with chromophores. In particular, the development of fluorophores[4] that allow high specificity to a target structure against an otherwise dark background revolutionized the field of microscopy. Many fluorescent molecules with high quantum yields and durable photostability that can be covalently attached to target proteins have been developed in the last few decades. More recently, advances in genetic engineering[5] and the discovery of the naturally fluorescent green

fluorescent protein (GFP)[6] from Aq. Victoria algae has permitted *in vivo* labeling of specific proteins. Recombinant DNA techniques are used to attach the DNA sequence for the fluorescent protein (FP) into DNA at the C or N terminal end of the protein and introduce the engineered DNA into the cell, yielding 'chimeric' proteins. Presently there are many GFP mutants covering almost every color of the spectrum.[7] To emphasize the importance of these technological and scientific advances, the Nobel Prize in chemistry in 2008 was awarded to the researchers who discovered, characterized and engineered GFP.

Research described in this dissertation develops and applies novel techniques in microscopy in order to learn more about protein interactions in live cells and image/characterize different aspects of cellular structure and function. An important principle underlying much of this work is the ability of light to be mixed constructively and destructively via nonlinear processes. A nonlinear optical effect occurs when the response of a material system to an applied optical field depends in a nonlinear manner on the strength of the optical field.[8] Two light waves that are in phase will constructively interfere or "add up." Similarly, two light waves completely out of phase may cancel each other out. One nonlinear effect important for this dissertation research arises when two light waves with different frequencies constructively interfere in matter to produce new frequencies). The wave mixing phenomenon is used to access electronic and vibrational states in molecules that otherwise would require highly energetic or highly intense light. We make use of nonlinear processes to extend the potential of linear (conventional) microscopy. The next section reviews briefly how microscopy has been changed by the use of multi-photon techniques. This review will enable us to understand

the advantages and disadvantages of multi-photon techniques over single photon methods.

1.2. Linear and non-linear excitation in microscopy

1.2.1. Principles

For most of the 20th century, simple light microscopes made use of linear interactions of light with matter. The response of a molecule to an applied field is linear when the response is directly proportional to the incident field strength. One of the first linear interactions of light with matter exploited in microscopy was absorption. For example, dyes that stain particular structures or sections in a cell were developed as contrast enhancing agents for white light visualization. The absorption of light is still widely used and has many biological applications[9]. The second interaction of light with matter that became widely used over the years was fluorescence. The use of high intensity light from Mercury or Xenon lamps with discrete excitation lines allowed for the photoselection of particular fluorophores that specifically tagged a molecule. The same strategy[10] was followed by the first lasers as they were used as coherent, highly polarized and monochromatic light sources (to directly replace weaker incoherent light sources).

Fluorescence experiments take advantage of the discrete quantized energy levels (eigenstates) of molecules and the selection rules that determine whether or not a molecule will change its eigenstates through absorption or emission of light. Practical molecular fluorescence in biological environments is a superposition of many subtly

different energies ("heterogeneous line broadening"), so these states actually appear as broad bands.

Using single photon excitation in linear spectroscopy (Figure 1.1A), with a mercury lamp or an Ar^+ ion laser, a molecule or atom can be taken from a ground state to a first excited state by absorbing one quantum of energy (photon) equal to that transition energy gap. One way for the molecule or an atom to relax or decay back to the ground state is by *spontaneous* emission. If the photon emitted is less energetic than the photon used to excite the molecule or atom, the energy difference is called a Stokes shift. If the emitted photon is more energetic, the energy difference is called an anti-Stokes shift. Fluorescence is almost always Stokes shifted because molecular interactions with the solvent lead to energy loss.

While the molecule or atom is in the excited state, another photon matching the energy difference between ground and excited states may *stimulate* emission of a second photon with the same polarization and direction (coherent) as the initial photon, relaxing the molecule to the ground state.

The third linear interaction of light with matter is scattering of light. If the scattered light has the same energy (or color) as the incident light, this elastic process is called Rayleigh scattering[11]. If the scattered light has a different wavelength, this inelastic process is called Raman scattering. Five years after its prediction[12], in 1928 Sir Chandrasekhara Venkata Raman[13] observed that an incident beam of monochromatic light produced an array of colors as it traversed various different liquids and "vapors". Most of the scattered light arose from Rayleigh scattering, but there were weaker contributions from different wavelengths. These contributions are due to incoherent

transfer of energy between vibrational modes by inelastic scattering. The scattered components give rise to Stokes and anti-Stokes shifts through inelastic scattering of a photon from an atom or molecule and are independent of the energy of the incident light. The molecular motions observed by Raman correspond to vibrational modes of individual chemical bonds in the molecules. While spontaneous fluorescence requires a residence time or lifetime for the photon to be emitted, Raman scattering is produced instantaneously and at any frequency of applied light. Unfortunately, the Raman effect is very weak[14] as only one event in a million produces an inelastic scattered photon. This limitation makes application of this technique to biological samples extremely difficult. As we later explain, nonlinear methods can help overcome this crippling disadvantage.

In 1931 Maria Göppert-Mayer developed a theory using Dirac's perturbation method to describe how multiple photons might be absorbed simultaneously to excite an atom.[15] Her theory can be applied to explain multi-photon effects such as two-photon absorption, two-photon emission, Stokes and anti-Stokes Raman effects.[16] A multi-photon process involves the simultaneous interaction of more than one photon with a molecule or atom via an intermediate, virtual state. This state is a superposition of states and not an eigenstate of the molecule or atom (Figure 1.1B). Because the probability of multi-photon excitation is very low, high intensity fields with high peak powers are required to observe such phenomena. Such fields only came about with the development of the laser.[17] Thirty years after Maria Göppert-Mayer's paper, Kaiser and Garrett[18] generated blue fluorescence at 425 nm by irradiating crystals of $CaF_2:Eu^{2+}$ with red light at 694 from a ruby optical maser, proving two-photon absorption. Technological advances in microscopy led to the development in 1978 of the first nonlinear scanning

laser microscope in Oxford, England. Sheppard *et al.*[19,20] and Gannaway *et al.*[21] used a CW neodymium YAG laser (1 Watt) to raster scan slabs of thin crystals and other materials to demonstrate optical sectioning by second-harmonic generation.

The development of mode-locked femtosecond lasers[22] in the 1980's provided the tools that allowed researchers to begin exploiting multi-photon effects in microscopy. For example, since two-photon excitation is proportional to the square of the intensity (or photon density) halving the pulse duration (for the same average power), increases two photon absorption efficiency will increase by a factor of four. Femtosecond lasers provided the necessary peak power required for the multi-photon effect. The combination of ultrashort pulses and high repetition rates provides an optimal light source for multi-photon excitation.

The processes that are available through linear interaction of light with matter (absorption, fluorescence and scattering of light) are also accessible by nonlinear effects. The cost of using nonlinear techniques is the higher peak power of the incident light required for the absorption probability to produce the nonlinear effect. This problem is overcome by the use of femtosecond or picosecond lasers capable of delivering high peak power with high repetition rates.[16] In the next section, we describe some of the advantages and applications of multi-photon techniques that are relevant to this dissertation.

Figure 1.1 Jablonski diagrams of single photon and an example of multi-photon excitation.. A) Single photon excitation fluorescence, B) Two-photon excitation fluorescence making using of a virtual state to reach the first excited state S1. (V=virtual state).

A)

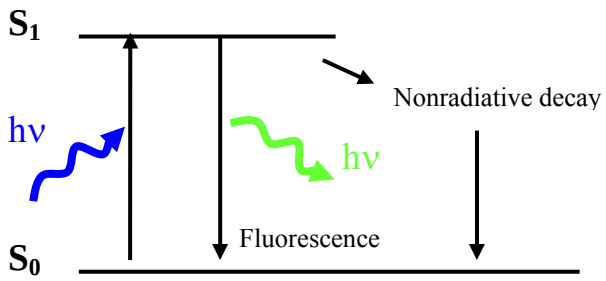

B)

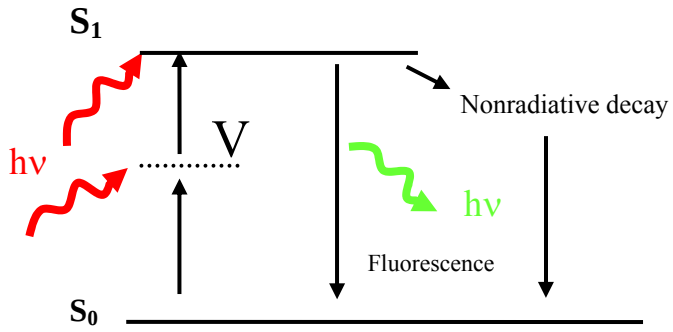

1.2.2. Applications

Before the development of the femtosecond laser, the most common use of CW lasers in microscopy was for confocal scanning laser microscopy (CSLM)[23]. This technique is based on the use of a conjugate pinhole to reject light that is not emitted from the focal point. With multi-photon excitation this requirement is obviated because the fluorophore can only be excited at the focus, where the multi-photon (e.g. two-photon) absorption probability density is large enough for nonlinear effects to be seen[24].

This ability to do 3D sectioning without the alignment of a pinhole has become one of the main advantages of multi-photon excitation (a nonlinear process) over single photon excitation (a linear process). For example, the two-photon excitation scheme applied to microscopy (developed in 1990 by Webb *et al.*[25]) excites different endogeneous (auto-fluorescent) and exogeneous fluorophores in live cells by using a near infrared (NIR) femtosecond pulsed laser. In this type of experiment, an excitation volume (defined by the squared intensity absorption probability of the fluorophore) is created that is just a fraction of a femtoliter (Figure 1.2). The fact that the probability scales as the square of the laser intensity provides 3D sectioning capability without the need of a pinhole. The use of near infrared (NIR) up to infrared (IR) light provides this experiment with other advantages, namely low tissue absorption probabilities and reduced Rayleigh scattering. On the other hand, live cells or tissue can suffer significant damage[8,26] because of the large powers used to create the excitation volume – on the order of 10^{20} to 10^{30} photons/cm^2 sec. Most of the damage is generally concentrated at the focal point. In

single photon excitation, the damage and bleaching of the fluorophore occurs along the whole beam path.

Figure 1.2 Drawing of two photon excitation. A) Drawing of the intensity field created in two-photon excitation as an example of multi-photon excitation. The focused light reaches photon intensities high enough to produced two-photon excitation in a small volume. B) One photon and two-photon excitation of a concentrated solution of fluorescein (50 μM) using 380 and 760nm light, respectively. The image was obtained from Dr. Zhen-Li Huang[36], University of Central Florida.

A)

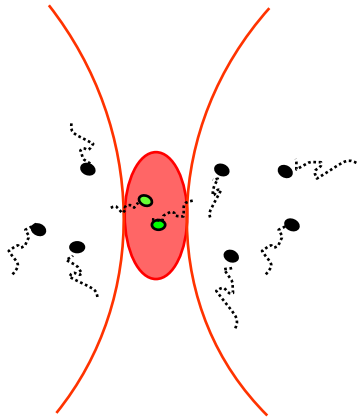

B)

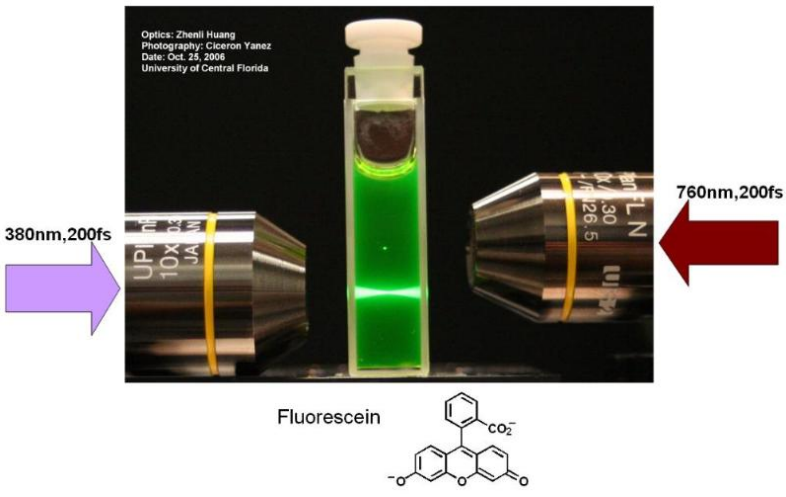

A technique widely used to study live cells that takes advantage of multi-photon excitation is two-photon Fluorescence Correlation Spectroscopy (TPFCS). In general, FCS observes the small fluorescence fluctuations due to particles moving into and out of the tiny volume created by the two photon absorption probability. The data can be analyzed to obtain the concentration and mobility of the fluorescent particles (i.e., diffusion coefficient). An autocorrelation function is created from the observed tiny fluorescence fluctuations. After fitting to an appropriate model, the concentration and diffusion time characteristic of the fluorescing particle are extracted. FCS has been applied *in vivo*[27-29] and *in vitro*[30-33] to study many different biological systems and has also been used to acquire Image Correlation Spectroscopy (ICS)[34] where correlation is performed over an entire frame. An associated technique Raster ICS (RICS)[35] makes use of the fast scanning speed (~10 μs/pixel) of the CSLM to create correlation profiles on each pixel similar to autocorrelation functions seen in FCS.

Techniques like FCS can make use of the spatially confined volume of two-photon excitation, while other techniques like Coherent Anti-Stokes Raman Spectroscopy[37,38] (CARS) also take advantage of the ability to access chemically specific transitions such as vibrational modes. Recently, the application of CARS to microscopy[39] has brought chemical specificity to multi-photon microscopy. CARS microscopy allows one to image molecules without the need of labeling or tagging the target molecule with a fluorophore (reducing disruption to the system under observation, Figure 1.3a). Therefore, CARS is non-invasive, provides 3D sectioning (because of its multi-photon origins) and has no equivalent in single photon excitation. To carry out a CARS

experiment, one overlaps two laser pulses in time and space so their beating will exactly match a specific vibrational state, i.e. C-H stretch. A third pulse inelastically scatters from the beating oscillators to produce a signal spectrally distinct from the incident beams, an anti-Stokes signal. In 1999, CARS was first applied to microscopy by Zumbusch *et al.*[39] Xie *et al.* have demonstrated the application of this technique to many observations of cellular systems. Some of their studies included visualizing lipids by looking at the C-H stretch in brain cells[40] and by looking at the O-H stretch of water in cells.[41] Another use of this technique was performing CARS correlation spectroscopy[42,43] by observing the C-H stretch of polystyrene beads. The CARS technique has recently been refined; first by including time gating of the signal[44] to separate the background from the prompt CARS photon, and second by adaptive optics[45] to help generate a clear focus while penetrating deep into tissue (~200μm).

Another technique exploiting quantum mechanical principles that will be important in this dissertation research is Stimulated Emission Depletion (STED)[46]. A STED experiment is carried out using confocal microscope where a very short pulse (~5 ps) is used to excite the fluorophore. This pulse is immediately followed by a depletion beam in the emission band of the fluorophore that causes stimulated emission. If the depletion beam is made into the shape of a ring or donut (with zero intensity at the center), the remaining un-quenched fluorophores that survive at the center give a sub-diffraction spot that can be detected conventionally. There are many ways to create "rings" or "donuts" of depletion using phase plates.[47] These objects are pieces of glass that have a thin-film coated onto them that give portions of an incident beam different

relative phase. When the laser beam is focused, destructive interference of the beam creates a 'zero' at the center of the beam (Figure 1.3b).

Using STED, recently a spatial resolution of 30 nm has been achieved by Meyer *et al.*[48] in the study of proteins in fixed neurons. Other applications of this technique include studies of the dynamics of lipids in the plasma membrane of a living cell[49] and nanoparticle assemblies[50] of supramolecular aggregates in a cell membrane and colloidal nanoparticles.

Figure 1.3 CARS and STED. A) Jablonski diagram of Coherent Anti-Stokes Raman Spectroscopy.[51] The process can be broken down into three separate steps: 1) Creation of the fluorescent state by exciting the desired Raman mode, 2) Pumping of the vibrational state and 3) Emission of anti-Stokes energy (blue shifted) back to ground state. B) Jablonski diagram of Stimulated Emission Depletion. C) STED process: as in single photon excitation, the fluorescent molecule is brought to the first excited state. Before any fluorescence takes place, a beam in the shape of a donut (overlapped with the initial excitation beam) quenches the excited molecules to the ground state leaving behind a diffraction limited spot in the center.

A)

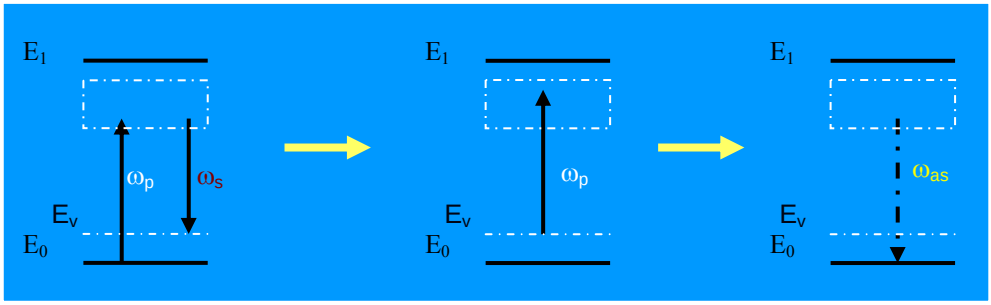

1. Need to populate the vibrational state first: Vibration at $\omega_v = \omega_p - \omega_s$

i.e. CH stretch

2. Excite the vibrational state E_v with ω_p

3. Anti-Stokes signal from the excited vibrational state of a molecule at $\omega_v = 2\omega_p - \omega_s$

B)

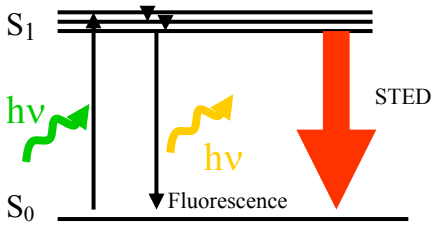

C)

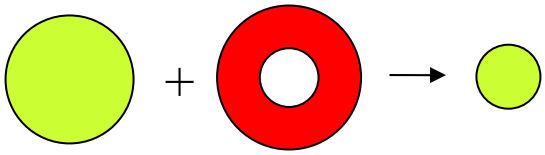

1.3. The translational and rotational diffusion coefficients

The first observation of diffusion (a stochastic process of motion by inertia) can be traced back to the botanist Robert Brown, who in 1827 observed pollen particles randomly moving about with a constant jiggle. One of his most interesting observations was that the magnitude of the 'jiggle' was temperature dependent.[52] This 'jiggle' was found to be the motion of the pollen particles performing a 'random walk' or diffusing in water. Considered to represent intrinsic transport properties of a molecule, the rotational and translational diffusion coefficients describe a molecule's random walk as it rotates (about itself) and moves laterally through solution. The studies in this dissertation that measure diffusion are limited to the low Reynolds number regime[53] ($Re << 1$), where viscous forces are stronger than inertial forces. As one aside, we have seen that at very early times (on the order of hundreds of femtoseconds), there are subdiffusive motions ('librational', see Chapter 3) that precede diffusion. The low Reynolds number restriction prevents us from including in our treatment processes that are turbulent or non-stochastic in nature such as active transport.

A primary motivation for measuring the diffusion coefficient has been to obtain the hydrodynamic radius of the molecule and, by inference, the molecular weight or shape. The hydrodynamic radius is the apparent radius of the molecule plus any 'hydration shell' that appears to "stick" to the surface of the molecule as it moves in the solvent. The relationship between the hydrodynamic radius of the molecules and the diffusion coefficients is given by the application of the Stokes-Einstein (SE) relation for spheres[54,55]; and Perrin's equations[56] for ellipsoids of revolution. The SE relation for the translational and rotational diffusion of a perfect sphere are[57]:

$$D_t = \frac{k_B T}{6\pi\eta r}$$
$$D_r = \frac{k_B T}{8\pi\eta r^3} \qquad (1.1)$$

where D_t and D_r are the diffusion coefficients, k_B is Boltzman's constant, η is the viscosity of the solvent and r is the hydrodynamic radius of the molecule.

The determination of the precise shape of a molecule (esp. a protein) using the diffusion coefficients is ill conditioned and thus often restricted to modeling the molecule with different types of ellipsoids, i.e. prolate (cigar-like) or oblate (disk-like).

1.4. Scope of dissertation

Our efforts have centered on developing techniques that will enable us to explain and better understand problems of molecular motion and association in biophysics. In particular, we have focused on several fluorescent techniques that have become more effective in the last decade, like two-photon fluorescence correlation spectroscopy (FCS).[58] This technique has given us the opportunity (through collaborations) to consider interesting biological questions. In Chapter 2, we will focus on two systems that we have explored in depth and that demonstrate the capabilities of FCS. The first system studies the interaction in the nucleus of COS-7 cells of a cyan fluorescent protein (CFP) tagged Tif2 protein and yellow fluorescent protein (YFP) tagged Androgen Receptor (AR) under different drug treatments. The first part of this chapter concerning the AR-Tif2 studies was published in 2007.[59]

Another project of interest used GFP tagged c-myc protein for studies of the endogeneous and transfected levels in mouse embryo fibroblast cells (MEF). These

studies showed that the relatively high levels of protein generated by transfection shift the apparent diffusion coefficient (likely decreasing the fractional population of c-myc bound to chromatin as concentration increases). We have presented this work in posters and a manuscript is in preparation.

In Chapter 3, to complement our experimental approaches, molecular dynamics (MD) and quantum mechanical simulations (QM-MM) of two well studied molecules, perylene and tetracene in n-hexadecane, were performed. They were compared to the femtosecond upconversion studies[60] previously performed in our lab that revealed a fast in plane 'libration' of around 400 femtoseconds. The perylene studies were published in 2008.[61]

In Chapter 4, we combined two-photon excitation in a microscope with electronics selected to obtain simultaneously Time Correlated Single Photon Counting (TCSPC) and FCS data of various fluorophores. We are able to measure many fluorophores' lifetimes reproducibly in a microscope using concentrations as low as 20 nM of a free dye (like Alexa 488, Invitrogen Inc). We have explored the two-photon excitation of the enzyme co-factor NADH and the changes in lifetime upon binding to horse liver alcohol dehydrogenase (HLADH) in the presence of isobutyramide (an inhibitor that locks the co-factor in place). Another fluorophore we used is 6-MI (a guanosine nucleotide analog) to study the structural changes of a single stranded DNA that can form a G-quadruplex. A slight change in the diffusion coefficient is seen when the highly stable 'cage' is formed in the presence of high salt concentration.

In the fifth chapter, we use *three* photon epi-CARS (E-CARS) to i) image using the C-H stretch (~2900 cm^{-1}) in either lipids or polystyrene beads, ii) image lipid vesicles

containing NAD^+ by targeting the 1034 cm^{-1} mode of the ring moiety nicotinamide (a first attempt to measure NAD^+ and NADH ratios) and iii) to visualize water in a cell by targeting the 3300 cm^{-1} O-H band. We also describe how we most recently developed a Stimulated Emission Depletion (STED) microscope and tested its capabilities using 170nm beads and a proprietary dye.

Other small projects (attached as appendices) include the coding of a graphical user interface (GUI) and the rewriting of the FORTRAN code to run as a dynamic link library for the program BIOEQS (A global rate analysis suite for complex equilibria) published in 2008[62] and the heating of Au nanoparticles by lasers to trigger a power dependent melting of dsDNA and consequent release of fluorophore labeled ssDNA.

Chapter 2: Tif2/AR and c-myc protein studies using Two Photon Fluorescence Correlation Spectroscopy

2.1. Introduction

The concept of FCS was developed in 1972 by Magde *et al.*[63] to measure the fluctuations arising from the binding of ethidium bromide, an intercalating dye, to DNA. The fluorescence of ethidium bromide strongly increases when it binds DNA. However, because of limitations of detection sensitivity and the length of time required to acquire data, FCS was not used for many decades. Only in the last few decades has this technique become more popular, thanks to improvements in laser technology, photo-detectors with very low dark counts and high sensitivity, and new microscope techniques. These technological advances allowed sample volumes to be reduced and consequently the size of the fluctuations increased.

It is now possible to observe the translational motion of fluorescently labeled molecules using this technique. The volumes (interrogated using either one or two photon excitation) are on the order of or less than one femtoliter. At nanomolar concentrations, only a few molecules traverse this volume giving rise to a Poissonian distribution of the particle number. Other established methods such as Dynamic Light Scattering (DLS)[64] can measure the translational diffusion coefficient, but there are many advantages to FCS. For example, FCS directly measures the self diffusion coefficient while dynamic light scattering measures the mutual diffusion coefficient, requiring extrapolation to 'infinite' dilution. Also, the small volumes interrogated in FCS are useful for observing samples that have spatially confined compartments (like cells). Another important advantage is

that any changes such as binding that can affect the emitted fluorescence can be interrogated (as originally shown by Magde *et al.*[63] with the ethidium bromide/DNA enhancement experiments).

Fluorescence correlation spectroscopy can be used to study concentrations, interactions and conformational changes of molecules at very low concentrations (typically less than 1 μM). The most basic application of FCS, and the one most commonly used to study bio-molecular associations involves fluctuations due to the local changes in concentration. These intensity fluctuations are recorded over time at a specific sampling rate faster than the motions under observation (Figure 2.1). The statistical analysis performed on the 'strip chart' is the autocorrelation function. The analysis is performed by applying a varying time delay to the initial strip chart and comparing the similarity of this delayed strip chart to the original chart. As the shift in delay increases, the probability that the initial and the time delayed strip are similar decreases to zero. The parameters recovered from this analysis are: 1) the amplitude at delay time zero that can be related to the number of particles diffusing in the small volume and 2) the translational diffusion time (see Figure 2.1). To obtain the translational diffusion coefficient, the autocorrelation function must be analyzed with a particular physical model such as 3D diffusion, anomalous diffusion or diffusion with binding.

Figure 2.1 ACF data and collection and analysis. A) Example of data collected for two channels (Ch1: blue line and Ch2: green dot) of Alexa 488 (90nM) excited with 780nm light collected at a sampling rate of 100kHz.. (Only a short segment of the whole data set is shown). B) Autocorrelation of ch1(blue) and ch2(green) and crosscorrelation(red). ACF is the result of applying Eq 2.7 to the whole data set in a). The amplitude (red parenthesis) is inversely proportional to the particle number and the blue double arrow (τ_D) gives the diffusion time.

A)

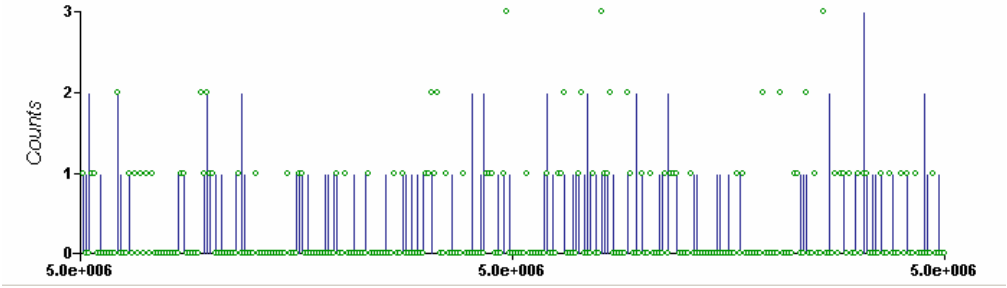

B)

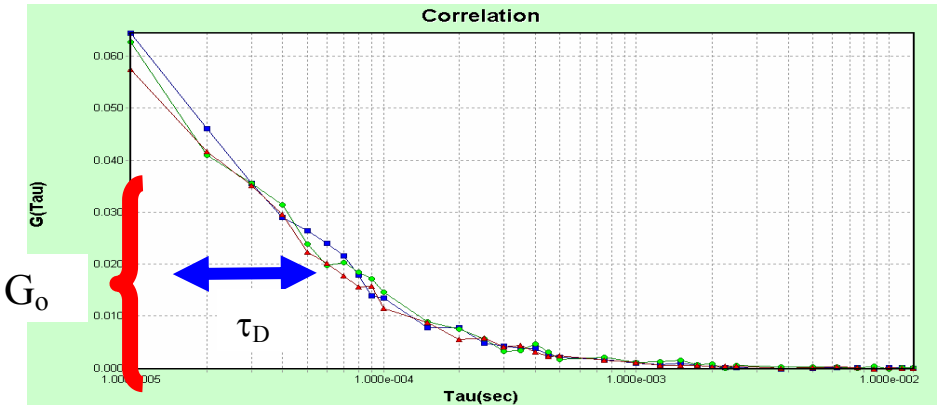

If one can arrange to excite simultaneously two fluorophores that emit at different wavelengths (e.g. by two photon excitation, Figure 2.2), it is possible to cross-correlate the intensity *vs.* time traces of these molecules in two detectors. This technique is called Two Photon Two Color Fluorescence Cross Correlation Spectroscopy (TPTCFCCS) and

is a variation of single channel FCS[65,66]. If the two fluorescent species are non-interacting and hence do not diffuse together, the fluctuations in intensity due to their number fluctuations will be entirely uncorrelated. If on the other hand, there is 100% complex formation, the fluctuations will be 100% correlated in time. Therefore, TPTCFCCS, in principle, can yield direct, very low background, quantitative measurements of protein-(intermediary)-protein interactions in living cells.

As explained earlier, the ability to tag cellular proteins with fluorescent markers has made it possible to observe protein interactions in vivo. Förster Resonance Energy Transfer (FRET) is the technique most widely used to demonstrate protein interactions. FRET makes use of "donor" quenching in the presence of an "acceptor" fluorophore when the pair is within ~100Å of each other. In comparison to FRET, FCCS is not so dependent on this close proximity and general geometric arrangement of the proteins. Because of this ability to go beyond 'close contact' interactions, FCS can provide direct, very low background, quantitative measurements of protein-protein interactions in living cells.

In this chapter, we examine two systems that involve protein interactions in the nucleus, Androgen Receptor (AR) and Tif2 protein interactions using TPTCFCCS and c-myc protein concentration levels. These studies demonstrate the capabilities of FCS to measure protein co-mobility and measure low protein concentrations *in vivo*. In the next section, we will explain the general theory related to the Autocorrelation Function Analysis specifically related to two photon excitation. The third section includes the Materials and Methods used. The fourth section provides results and discussion for each study.

Figure 2.2. Single photon A) and two photon excitation B) Jablonski diagrams. V denotes a virtual state between the ground and the first excited state.

A)

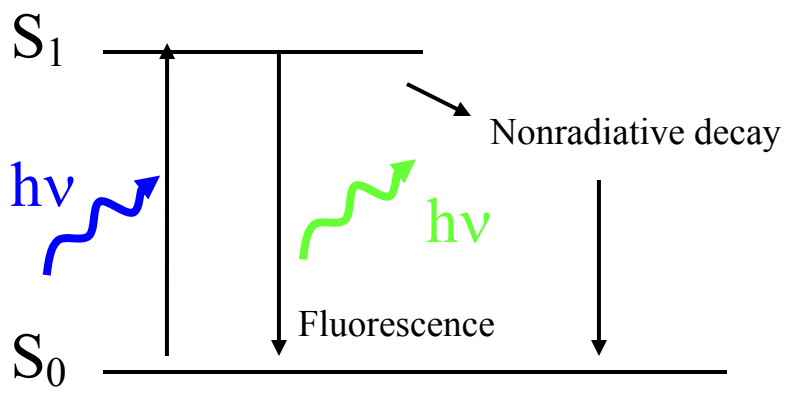

B)

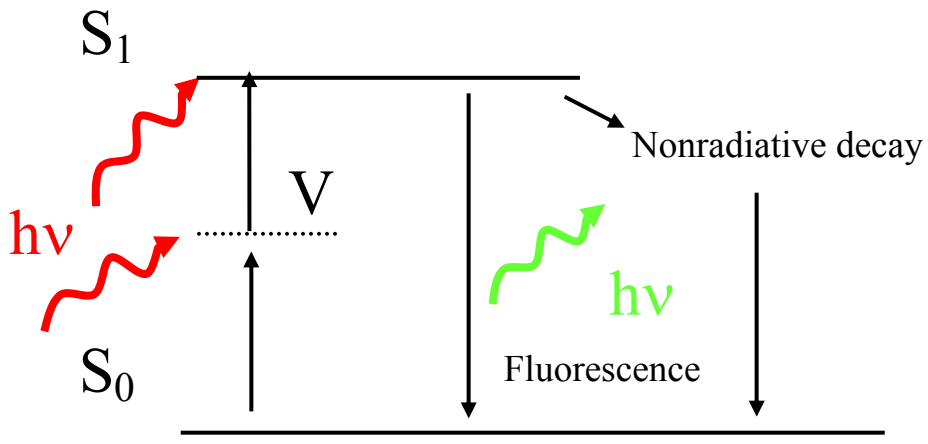

2.2. Theory

2.2.1. One and two photon cross-section

If we assume arbitrary polarized light $\vec{E}(\omega,t) = Ee^{-i\omega t} + c.c.$ and that the dipole moment interaction between states *m* and ground state g is given by μ_{mg}, then the probability of transition to the excited state from the ground state for large t is (Boyd)[8]:

$$p_m^{(1)}(t) = \frac{2\pi\left|\mu_{mg}\cdot E\right|^2 t}{\hbar^2}\rho_f\left(\omega_{mg}=\omega\right) \tag{2.1}$$

where ρ_f is the density of final states (or atomic lineshape function) evaluated at frequency ω of the incident laser light.

The linear absorption rate is given by (special case of Fermi's golden rule):

$$R_{mg}^{(1)} = \frac{p_m^{(1)}(t)}{t} = \frac{2\pi\left|\mu_{mn}\cdot E\right|^2}{\hbar^2}\rho_f\left(\omega_{mg}=\omega\right) \tag{2.2}$$

The linear absorption can be written as:

$$R_{mg}^{(1)} = \sigma_{mg}^{(1)} I \tag{2.3}$$

where $I = 2n\varepsilon_O\left|\vec{E}\right|^2$ is the intensity of the light to give for the linear cross section σ:

$$\sigma_{mg}^{(1)}(\omega) = \frac{p_m^{(1)}(t)}{t} = \frac{\pi\left|\mu_{mn}\right|^2}{n\varepsilon_O c\hbar^2}\rho_f\left(\omega_{mg}=\omega\right) \tag{2.4}$$

Similarly, use of second order perturbation theory to calculate the two-photon absorption probability from ground state *g* to an excited *n* through virtual states *m* is given by (Boyd)[8]:

$$p_n^{(2)}(t) = \left|\sum_m \frac{\mu_{nm}\mu_{mg}E^2}{\hbar^2\left(\omega_{mg}-\omega\right)}\right|^2 2\pi t\rho_f\left(\omega_{ng}=2\omega\right) \tag{2.5}$$

The sum of the states is over all possible virtual states as developed by Maria Göppert-Mayer. Also, a two-photon cross-section whose intensity (given in photons cm^{-2} sec^{-1}) can be derived:

$$\sigma_{ng}^{(2)}(\omega) = \frac{\omega^2}{4n^2\varepsilon_0^2c^2}\left|\sum_m \frac{\mu_{nm}\mu_{mg}}{\hbar(\omega_{mg}-\omega)}\right|^2 2\pi\rho_f(\omega_{ng}=2\omega) \qquad (2.6)$$

with $R_{ng}^{(2)} = \sigma_{ng}^{(2)} I^2$ and $I = \frac{2n\varepsilon_O c}{\hbar\omega}|E|^2$ for the two-photon absorption rate and the intensity respectively.

2.2.2. Selection rules

A wavefunction (with even orbital angular momentum quantum number) is said to have even parity (*gerade)* if the wavefunction is unchanged upon coordinate inversion. It is said to have odd parity (*ungerade*) if the wavefunction changes sign upon coordinate inversion. Recall that the interaction energy (dipole moment) is given by $\vec{\mu} = -e\vec{r}$ (where e is the electron charge and $\vec{r}$ is the direction of the incident light). Using braket notation, we can say that the dipole transition probability from a ground state to an excited state is given by[67]:

$$P_{fi} = \left|\langle f|e\vec{r}|i\rangle\right|^2 \qquad (2.7)$$

Because $\vec{r}$ operator acts to invert the coordinate axes of the wavefunction, $P_{fi} \neq 0$ only if states $\langle f|$ and $|i\rangle$ have different parity. The selection rules for these electronic transitions (g→u and u→g) are called "allowed" transitions while (u→u and g→g) are called "forbidden transitions".

For a two-photon process, the transition probability is given by[68]:

$$P_{fi} = \sum_m \left| \langle f | e\vec{r} | m \rangle \langle m | e\vec{r} | i \rangle \right|^2 \quad (2.8)$$

So, in this case transitions that are one-photon forbidden become accessible using two-photon absorption.

2.2.3. The Autocorrelation Function

The instantaneous rate for absorption of photon pairs is given by:[24,25,69]

$$W(\vec{r},t) = \frac{\sigma_2 I^2(t) S^2(\vec{r})}{2} \quad (2.9)$$

where σ_2 is the two photon absorption crosssection, I(t) is the peak laser intensity and S(r) is point spread function or spatial profile. Assuming that the fluctuations occur on time scales longer than the laser pulse width and repetition rate, then the average excitation rate is given by[24]:

$$\langle W(\vec{r}) \rangle = f_p \int W(\vec{r},t) dt \quad (2.10)$$

where f_p is the laser pulse repetition rate.

The change in fluorescence is given by the beam intensity and fluctuations in concentration:

$$F(t) = \alpha \int d\vec{r} W(\vec{r}) C(\vec{r},t) \quad (2.11)$$

where α is related to the efficiency of the system and the fluorescence quantum yield, C(r,t) is the local molecular concentration of the fluorophore and the integration is over the observation volume. Continuing the derivation by Berland *et al.*[69] we define the observation volume not as a physical volume but rather as a probability given by[70]:

$$V_{psf} = \frac{1}{\langle W(0) \rangle} \int W(\vec{r}) d\vec{r} \qquad (2.12)$$

where <W(0)> is the unit volume generated by molecules located at the center of the focused laser beam. Because of the non-uniform fluorescence signal arising from the excitation source, i.e. Gaussian profile, another parameter is needed, the gamma factor[70]:

$$\gamma = \frac{\int \langle W(\vec{r}) \rangle^2 d\vec{r}}{\int \langle W(\vec{r}) \rangle d\vec{r}} \qquad (2.13)$$

The gamma factor for a Gaussian beam is equal to $2^{-3/2} \sim 0.35$ (=$1/\sqrt{8}$).

Note that we can rewrite Eq. 2.11 using Eq. 2.12 to give $F = \psi \langle C \rangle V_{psf}$ where ψ is the molecular brightness. This quantity is related to the ability of the whole system to detect the fluorescence in the detector(s).

For constant illumination, we can define now the fluorescence fluctuations arising from the concentration fluctuations by[70-72]:

$$\delta F(t) = \alpha \int d\vec{r} W(\vec{r}) \delta C(\vec{r}, t) \qquad (2.14)$$

where δC(r,t) are the local concentrations fluctuations from the average concentration.

Fluorescence fluctuations are time-correlated to generate the autocorrelation function **G(τ)**, defined as:

$$G(\tau) = < \delta F(\tau) \delta F(\tau + t) > / < F(\tau) >^2 \qquad (2.15)$$

with **τ**, being lag time.

For a system in 3D described by Brownian motion (simple diffusion), we have that changes in concentration are given by:

$$\frac{\partial(\delta C(\vec{r}, t))}{\partial t} = D \vec{\nabla}^2 \delta C(\vec{r}, t) \qquad (2.16)$$

where D is the translational diffusion coefficient. The kernel or point solution (Green's function) is given by:

$$\delta C(\vec{r},t) = \langle C \rangle (4\pi Dt)^{-3/2} \exp\left(-|\vec{r}|^2 / 4Dt\right) \tag{2.17}$$

We anticipate the volume for our V_{psf} is a "prolate ellipsoidal" gaussian. The beam profile is then:

$$W(\rho, z) = e^{-\left(2\rho^2\right)/w_0^2} e^{-\left(2z^2\right)/w_z^2} \tag{2.18}$$

with $\rho=\sqrt{x^2+y^2}$, w_o and z_o are the $1/e^2$ radial and axial beam waists.

Combining this result with the solution to concentration (Eq 2.8.2), for one diffusing species the autocorrelation function (Eq. 2.15) for a two photon system becomes:

$$G_D(\tau) = \frac{\gamma}{\langle C \rangle V} \frac{1}{\left(1 + 8D\tau / w_o^2\right)\left(1 + 8D\tau / w_z^2\right)^{1/2}} \tag{2.19}$$

So, at time $\tau=0$, we get that the $G_D(0)$ is inversely proportional to the concentration (or particle number).

2.2.4. The Cross Correlation Analysis

By exciting simultaneously two fluorophores which emit at different wavelengths, and simultaneously detecting their emission in two separate channels, *i* and *j*, under ideal conditions with no cross-talk (channel *i* only detects species 1 and species 12 while channel *j* only detects species 2 and 12), the cross-correlation function then becomes:

$$G_{ij}(\tau) = \frac{< \delta F_i(\tau) \delta F_j(\tau + t) >}{< F_i(t) >< F_j(t) >} \quad (2.20)$$

If we assume that the species present are the two free species, 1 and 2 and the complex 12, then Eq. 19 becomes:

$$G_{ij}(\tau) = \frac{\left(\langle C_{12} \rangle\right) M_{12}(\tau))}{\left(V\left(\langle C_1 \rangle + \langle C_{12} \rangle\right)\left(\langle C_2 \rangle + \langle C_{12} \rangle\right)\right)} \quad (2.21)$$

where $\mathbf{C_1}$, $\mathbf{C_2}$ and $\mathbf{C_{12}}$ are the concentrations of the free and interacting species, respectively and $\mathbf{M_{12}}$ is the term describing the diffusion of the complex**:**

$$M_{12} = \frac{1}{\left(1 + \frac{\tau}{\tau_{d12}}\right)\left(1 + \frac{r_o^2 \tau}{z_o^2 \tau_{d12}}\right)^{\frac{1}{2}}} \quad (2.22)$$

The amplitude at time 0 of the cross-correlation function is:

$$G(0)_x = \frac{\langle C_{12} \rangle}{\left(V \langle C_{1T} \rangle \langle C_{2T} \rangle\right)} \quad (2.23)$$

where $<C_{1T}> = (<C_1> + <C_{12}>)$ and $<C_{2T}> = (<C_2> + <C_{12}>)$.

Simultaneous excitation of two fluorophores can be achieved either using two coaxially aligned laser beams of different wavelengths[73] or alternately through two photon excitation using a femtosecond pulsed IR laser at a single wavelength[74]. The very broad two-photon cross-sections of many fluorophores are due to the selection rule relaxations mentioned above for specific two-photon transitions, and these conditions permit simultaneous excitation of fluorophores even if these fluorophores have large wavelength differences in their one-photon absorption peaks. The unintended consequence of using a single beam to excite two fluorophores or more is the possible overlap of emission by the fluorophores leading to “bleed-through” or cross-talk. The

best strategy to pursue requires fluorophores that have largely separable emissions or selecting filters that rigorously separate the emissions. Unfortunately, in many cases such solutions are not possible and the total amount of bleedthrough needs to be treated explicitly.

To correct for the "bleed-through" (cross-talk) of the CFP fluorescence signal in the YFP channel, we used the equations of Kim and co-workers[75]. The amplitude at time 0 of the autocorrelation correlation functions from the blue (b) and yellow (y) channels was defined respectively as

$$G(0)_b = \frac{\sum_i \eta_{i,b}^2 C_i}{V\left(\sum_i \eta_{i,b} C_i\right)^2} \tag{2.24}$$

and

$$G(0)_b = \frac{\sum_i \eta_{i,y}^2 C_i}{V\left(\sum_i \eta_{i,y} C_i\right)^2} \tag{2.25}$$

and the cross correlation amplitude at time 0 was

$$G(0)_b = \frac{\sum_i \eta_{i,y} \eta_{i,y} C_i}{V\left(\sum_i \eta_{i,y} C_i\right)\left(\sum_i \eta_{i,b} C_i\right)} \tag{2.26}$$

The molecular brightness values, $\eta_{i,b}$ and η_{iy}, of the species in each channel are taken into account, and the sums are over the three species, free eCFP-AR, free eYFP-Tif2 and the double labeled eCFP-AR/eYFP-Tif2 complex. The molecular brightness values of the eCFP and eYFP constructs in both channels were determined by separate

analysis of the photon counting histograms[76,77], using the ISS Inc. software for data taken under identical illumination and detection conditions.

2.3. Materials and Methods

2.3.1. Instrumentation

Two photon imaging and FCS measurements were carried out using a system assembled in the laboratory (Figure 2.3). The excitation source was a fs pulsed tunable titanium sapphire wide band laser (Spectra-Physics-Newport, Mai Tai) set at 920 nm. This wavelength proved to yield the best intensity ratios between the CFP and YFP signals. The excitation power was set at a level (< 25 mW at the microscope entrance) below which no further increase in the correlation amplitude was observed. The low power ensured minimal photobleaching and avoided excitation saturation effects[78]. The microscope was a Zeiss Axiovert 135 using an E700 SP 2P dichroic filter (Chroma Technology Corporation) to eliminate the IR exciting light. The objective was a 100X Plan-Neofluar oil objective (Zeiss) with a 1.3 numerical aperture. The microscope was equipped with a piezo-electric stage for x-y control (Mad City Labs, Inc.) and the objective was also equipped with a piezo-electric device for z-control (also from Mad City Labs, Inc). Detection was carried out using the Alba 2 fluorescence correlation system (ISS, Inc.).

Figure 2.3. Instrument setup for FCS. Maitai laser beam was telescoped to 8x its diameter. The beam was steered to a Zeiss Axiovert 135M microscope. The epi-detection was done using a 700SP dichroic. The autofluorescence was directed to the Alba II spectrometer. Two APD detectors were used with the necessary dichroic to split the light. DM= Dichroic mirror, DET=APD detectors (2 channels), F=Filters and L=Lens.

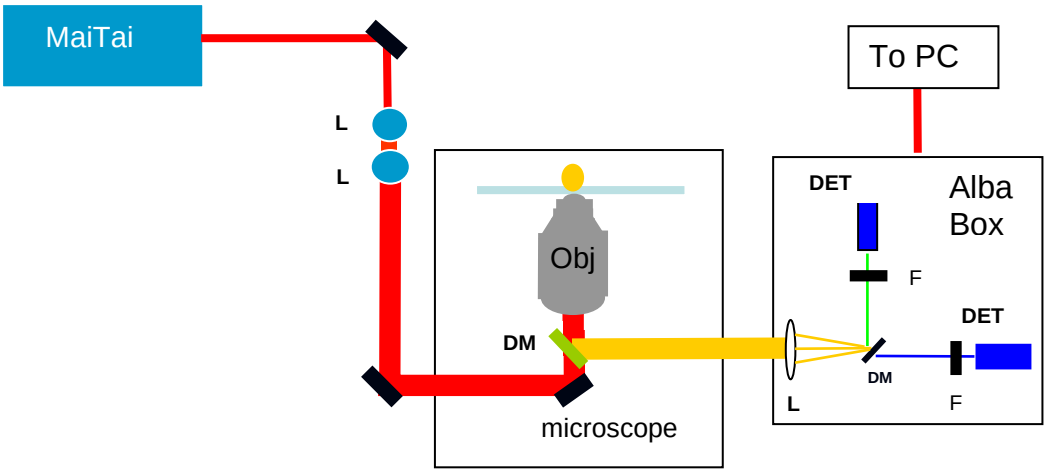

2.3.1.1. Tif2-AR studies

A 515 nm dichroic mirror was used to split the detected light onto two channels, and an additional 550 +/- 20 nm bandpass emission filter was placed before channel 1 to minimize the contribution of the eCFP signal. Excitation volumes were calibrated by measuring the diffusion of rhodamine 110 using an excitation wavelength of 920 nm. The beam waist, $2w_o$, was found to be 0.5 µm, while the z_o was 1.2 µm. FCS and imaging data on Cos-7 cells were acquired at light levels for which photobleaching was not evident. These settings precluded collecting data in regions of the cells exhibiting punctate distribution patterns of fluorescence and exhibiting very slow diffusion. Such

punctate structures were particularly evident in the presence of the antagonist, casodex, as has been previously demonstrated[79], and these structures were avoided in data acquisition. The two-photon imaging scan rate was 1 ms/pixel.

2.3.1.2. C-myc studies

A 495 nm dichroic mirror was used to split the detected light onto two channels, and an additional 520 +/- 40 nm bandpass emission filter was placed before channel 1 for eGFP detection and channel 2 had a 450 +/- 40 nm bandpass to detect mainly the autofluorescence. Excitation volumes were calibrated by measuring the diffusion of Alexa 488 and eGFP (Biovision Inc) using an excitation wavelength of 970nm. The$1/e^2$ beam waist, w_o, was found to be 0.34 μm, while the z_o was 1.4 μm.

2.3.2. Sample preparation

2.3.2.1. Tif2-AR studies

2.3.2.1.1. Plasmids and ligands

The fusion proteins, eCFP-AR and eYFP-Tif2 were expressed by insertion of the sequences encoding AR and Tif2 in PC1-ECFP and PC2-EYFP vectors from Clonetech, bearing the appropriate fluorescent protein sequence. Plasmid preps were carried out using DH5α cells grown on kanamycin by Dr. Cathy Royer. The ligands, R1881 and casodex, were the kind gift of Dr. Gordon Hager.

2.3.2.1.2. Cell culture and transfections

Cos-7 cells were cultured in DMEM medium (Invitrogen) supplemented with 10% fetal calf serum (Atlanta Biologicals), penicillin (100 microgram/ml) and streptomycin (100μg/ml) in a humidified atmosphere containing 5% CO_2 at 37 degrees C. For imaging and FCS, cells were plated on chambered coverglass (0.17 mm thick) (Labtek, grown to approximately 60% confluency, then transfected with 1-2 μg total of plasmid using Fugene 6 (Roche Applied Science) and grown overnight. The cells were prepared by Dr. Cathy Royer while on sabbatical at the NIH. The cells were then washed several times with PBS and the medium replaced with phenol red free medium containing charcoal stripped serum. Ligands were added where necessary at a concentration of 10nM. Hepes buffer at 10 mM was also added to help maintain the intracellular pH during imaging. Cells were incubated with ligands for at least 2 hours prior to imaging. Imaging was carried out for only 15 minutes at a time per sample, and during imaging unused chambers were stored in a CO_2 incubator at 37 degrees C.

2.3.2.1.3. Confocal microscopy

Confocal microscopy was carried out using an LSM 510 META confocal system equipped with 405-Vis lasers from Carl Zeiss, Inc (Jena, Germany). Cells were viewed with a 63x, 1.4-numerical-aperture Plan-Apochromat oil immersion objective. Images were acquired sequentially using a 458-nm laser line and emission between 470-500nm for eCFP and a 514-nm laser line and emission between 530-600nm for eYFP. Overlay images were assembled using Imaris 4.0 software form Bitplane AG (Zurich, Switzerland). The microscope was operated by Dr. Daniela Malide from NHLBI/NIH.

2.3.2.2. C-myc studies

2.3.2.2.1. Cell cultures and transfections

EGFP was fused in-frame with exon III at the murine c-myc locus in ES-cells. These cells were injected into blastocysts, and the progeny of chimeric mice were checked for germ-line transmission. Embryonic fibroblasts from mice homozygous for the correctly targeted allele were cultured for analysis. In some experiments, a plasmid vector transiently directing the expression of the same MYC-EGFP fusion was transfected into these same homozygous or non-targeted (wild-type) fibroblasts. The MEF cells were provided by Dr Zuqin Nie from Dr. David Levens lab at NCI/NIH.

2.4. Results and Discussion of nuclear protein interactions and transport

2.4.1. Tif2 and AR studies

2.4.1.1. Overview of Tif2 and AR proteins

Nuclear Receptors (NRs) constitute a large family of ligand dependent transcriptional regulators. They represent one of the major molecular strategies for the control of development, differentiation, growth and homeostasis in metazoans. Mutations or other malfunctions of the NR are implicated in a variety of human diseases including cancers (breast, prostate, uterine and certain leukemias), cardiovascular disease and obesity, among others. Binding by agonist or antagonist ligands specifically and differentially influences the cellular localization of these receptors. Ligands also modify NR structural dynamics, thereby modulating their ability to interact with their cellular

partners, such as molecular chaperones, DNA target sequences, and specific transcriptional coregulators. (see Nettles *et al.*[80]). The Androgen Receptor (AR), a member of the steroid hormone receptor sub-family, mediates the role of androgens in male sexual development. Certain mutations in the androgen receptor result in full or partial androgen insensitivity and incomplete development of the male sexual organs.

Indeed, conditional knock-out studies demonstrated that the expression of AR in Sertoli cells is required for spermatogenesis[81,82]. Moreover, abnormalities in AR function and interaction with co-regulators have been implicated in the development and progression of prostate cancer[83-86], and anti-androgens appear to be among the most promising therapeutic strategies in the treatment of the disease[87].

As with the other NRs, AR function is mediated by its interactions with transcriptional co-regulators, including the well-characterized p160 family of coactivators that exhibit histone acetyl transferase activity, allowing for the de-condensation of chromatin. These co-activators also recruit components of the general transcription machinery[88,89]. Post-translational modifications and the expression levels of these coregulators modulate the hormonal response in a tissue specific manner, thus allowing the integration of multiple signaling pathways[88,90,91].

Recently, Ye and coworkers[92], using bigenic mice harboring an AR activity indicator and either SRC-1+/- or Tif2+/- mutant alleles, demonstrated that Tif2 serves as the preferential AR coactivator in testes and that the two proteins coexist in Sertoli cells. This study highlighted the importance of *in vivo* characterization of the expression levels and interactions between nuclear receptors with various putative partners for understanding the specific signaling pathways coupled to specific physiological

responses. Nevertheless, it is difficult to probe structure-function relationships *in vivo*, given the relatively elaborate protocols for transgenic manipulation. In contrast, the description of the molecular mechanisms of ligand modulation of NR function, particularly interactions with coregulators, has seen significant progress in recent years due to high resolution structural studies, coupled with transient transfection and *in vitro* protein-protein interaction studies[93,94]. *In vitro* studies are nonetheless limited by the ability to express, purify and, for structural studies, crystallize reasonably large quantities of these proteins; in fact, no structure of a full-length receptor has been solved to date.

Even *in vitro* interaction studies, particularly those aimed at quantitative characterization, are hampered by the biochemical difficulties inherent in such complex systems. Moreover, it is difficult to address the role of post-translational modification or the competition or synergy with other protein partners. Beyond the *in vivo* and *in vitro* studies mentioned above, the elucidation of the subtle structure-function relationships underlying ligand-dependent modulation of nuclear receptor function will require direct quantification of the interactions between NRs and their cellular partners in an environment where 1) the full-length proteins can be used, 2) the role of post-translational modifications can be investigated, and 3) the effects of the expression levels of ternary partners and the impact of other factors (such as the cell cycle) can be assessed.

TPTCFCCS was first applied to the study of bio-molecular interactions *in vitro*[73]. Schwille's group first measured cholera toxin subunit interactions after endocytosis in live cells by TCTPFCCS[29], but only a small number of other live cell applications (by that group and others) of TPTCFCCS, either based on fluorescent protein fusions or micro-injections of labelled proteins, have appeared since then[75,95-97]. Applications based

on simultaneous two-color excitation using two coaxially aligned visible lasers have been published recently as well[98,99].The dimerization of the ligand binding domains of retinoid receptors was studied in live cells by one channel photon counting histogram analysis which is a variation of the analysis of fluctuation data[77]. This group has described a two colour version of the PCH experiment[100], recently applied to nuclear receptors ligand binding domain interactions[101]. In the present work, we describe the direct measurement of the ligand dependent interaction between full-length eCFP-labeled AR and eYFP-labeled Tif2 in live Cos-7 cells using TPTCFCCS.

2.4.1.2. Results and Discussion of the Tif2 and AR studies

Visible confocal microscopy of the Cos-7 cells (chosen because they do not express endogenous AR) co-transfected with expression plasmids bearing the eCFP-AR and eYFP-Tif2 fusion proteins confirmed the known ligand-dependent localization of the androgen receptor[79,102,103]. In the absence of ligand, eCFP-AR was localized predominantly in the cytoplasm, whereas eYFP-Tif2 was nuclear (Figure 2.4 panel A). Upon addition of the agonist, R1881, eCFP-AR translocated to the nucleus[104] and visually co-localizes with the eYFP-Tif2 (Figure 2.4, Panel B), confirming that the eCFP-AR fusion protein was competent for ligand binding. In the presence of the antagonist, casodex, this translocation of eCFP-AR occurrs, but was incomplete (Figure 2.4, Panel C). These observations were consistent with the previously demonstrated lower translocation efficiency of casodex[105] as compared to agonist ligands. The eYFP-Tif2, while remaining nuclear in the presence of antagonist, formed punctate structures which have been previously reported[79]. Two-photon images (Figure 2.5) of the Cos-7 cells co-

transfected with eCFP-AR and eYFP-Tif2 were similar to those obtained using visible confocal microscopy. As in the one-photon images, without ligand, eCFP-AR was cytosolic, while in the presence of either ligand, eCFP-AR moved into the nucleus (albeit to different extents for agonist *vs.* antagonist). Again, eYFP-Tif2 was nuclear in all cases. While both eCFP-AR and eYFP-Tif2 were found in the nucleus in the presence of both agonist and antagonist ligands, their protein-protein interaction was expected to be favored in presence of agonists. To differentiate between simple visual co-localization, and true physical interaction of eCFP-AR and eYFP-Tif2, we used TPTCFCCS.

As expected for a well-aligned system, the amplitude of the cross-correlation function of the cytoplasmic signals from channels 1 and 2 (emanating solely in this case from the eCFP-AR due to cross talk) in the absence of ligand was 100% because the ACF corresponded to eCFP-AR self-diffusion. Figure 2.6 shows examples of the auto-correlation and cross-correlation curves obtained in the nucleus of cells treated with the agonist R1881 (Figure 2.6a) and the antagonist casodex (Figure 2.6b). In the presence of agonist, the cross-correlation signal is essentially equal in amplitude to the lowest of the autocorrelation signals, the maximal cross-correlation achievable between the intensity fluctuations from the two channels. This relationship, in turn, demonstrated a maximal degree of interaction between the two proteins. In the presence of the antagonist, the amplitude of the cross-correlation is significantly reduced relative to the lowest auto-correlation amplitude (Figure 2.6b and c), consistent with a decrease in the interaction between eCFP-AR and eYFP-Tif2 when antagonist is present.

Figure 2.4. Confocal images of Cos-7 cells co-transfected with eCFP-AR and eYFP-Tif2. The first column corresponds to the eCFP channel, the second column to the eYFP channel and the third column is a merge of the two. Panel A represents cells imaged in absence of any ligand, Panel B corresponds to images of cells in presence of 10^{-8} M of the agonist R1881 and Panel C corresponds to images of cells in presence of 10^{-8} M of the antagonist, casodex.

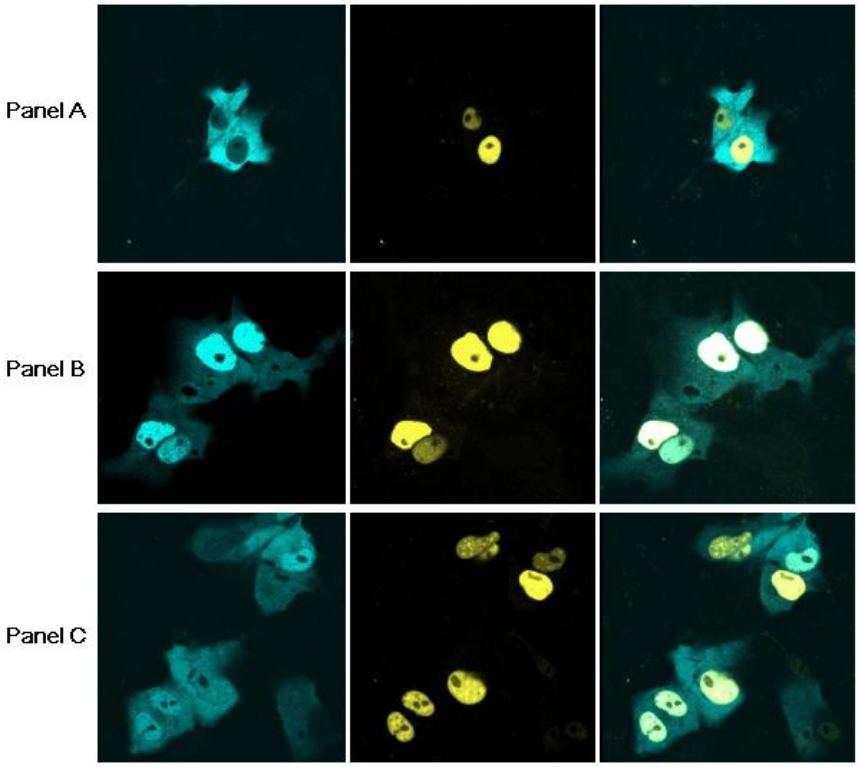

In principle, one can quantitatively determine the degree of interaction between the two proteins from the values of the auto and cross-correlation amplitudes at time zero according to equation 2.21[96]. The fluorescence detected in channel 1, however, includes intensity from both eCFP-AR and eYFP-Tif2. This bleed-through could lead to an overestimation of the concentration of eYFP-Tif2. Cells were chosen for imaging based on the high count-rate in channel 1 (predominantly eYFP) relative to that in channel 2 (eCFP) in order to limit this effect. For example, for the data in Figure 2.5a, the total intensity in the eCFP channel 2 was nearly 4-fold lower than that in the intensity in the eYFP channel l. In this situation, the bleed-through from eCFP into the eYFP channel amounted to only 10% of the total signal in the eYFP channel.

Figure 2.5. Two-photon images of Cos-7 cells co-transfected with eCFP-AR and eYFP-Tif2 (false color). The first column corresponds to the eYFP channel, the second column to the eCFP channel. Panel A corresponds cells in absence of any ligand, Panel B corresponds to images of cells in presence of 10^{-8} M of the agonist R1881 and Panel C corresponds to images of cells in presence of 10^{-8} M of the antagonist, casodex. The excitation wavelength was 920 nm.

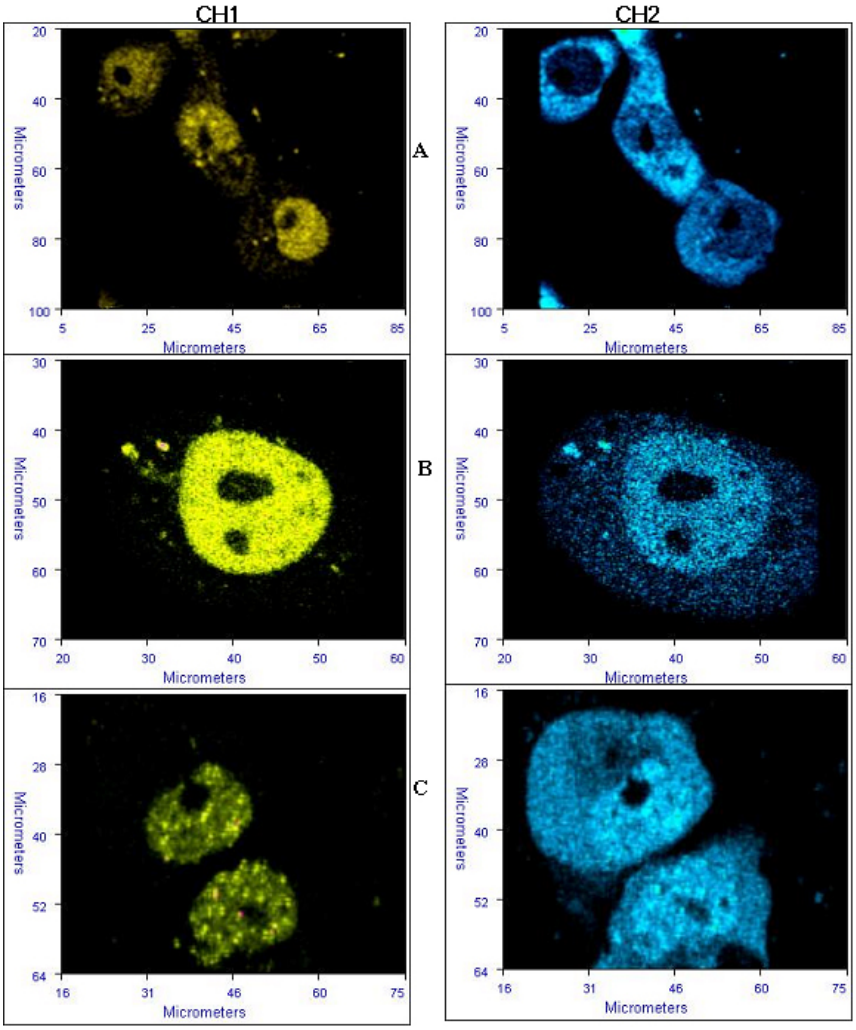

Figure 2.6. Auto and cross-correlation functions of the emission in the eYFP (channel 1) and eCFP (channel 2) channels for two-photon excitation of Cos-7 cells co-transfected with eCFP-AR and eYFP-Tif2. a) Curves correspond to profiles calculated from data obtained in the nucleus in presence of 10^{-8} M R1881 (Figure 2.5, Panel B), b) Curves correspond to profiles calculated from to data obtained in the nucleus in presence of 10^{-8} M casodex. (Figure 2.5, Panel C) and c) The cross-correlation profiles from a) and b) are re-plotted for direct comparison. Excitation was at 920 nm.

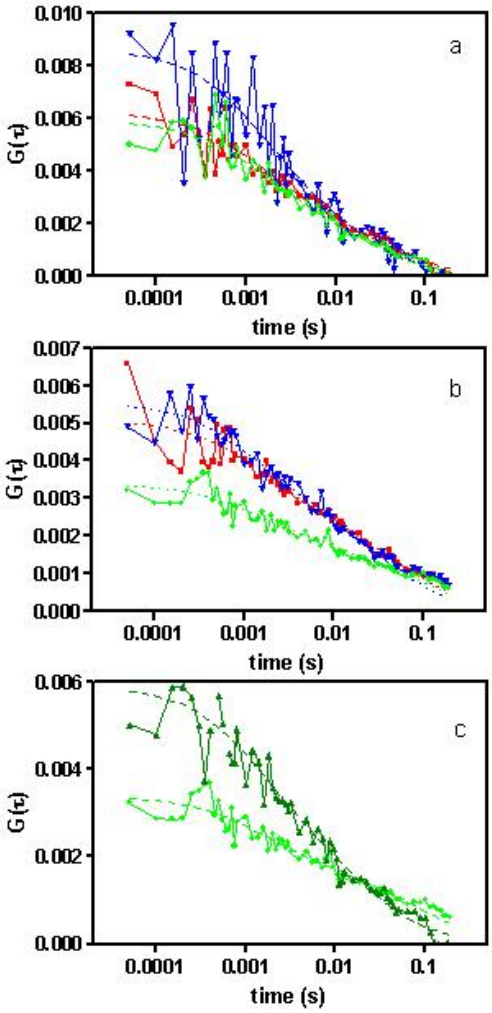

If the molecular brightness of each species in each channel is known (in counts per second per molecule, cpspm), then the actual concentrations of the species can be calculated by solving equations 7-9. The molecular brightness of the eCFP in both channels was determined by separate analysis of the photon counting histograms[100] derived from the photon fluxes of the emission from the cytoplasm. Since the eYFP-Tif2 is nuclear under all conditions, the signal from the cytoplasm in both channels arises only from eCFP-AR. The molecular brightness for eCFP-AR in the blue channel as determined by PCH analysis was 16040 cpspm, and in the yellow channel, 3850 cpspm. For eYFP, the molecular brightness in the yellow channel was determined from the PCH analysis of the photon flux from data taken in the nucleus in absence of ligand to be 36371 cpspm. In this case there is negligible eCFP contribution to the yellow channel, because very little eCFP-AR is localized in the nucleus in the absence of ligand. It was assumed for subsequent calculations that the brightness values of the eCFP and eYFP fluorescent proteins were unaltered by the formation of the complex. We note that previous studies using acceptor-bleaching methods indicated little or no FRET in this eCFP-AR/eYFP-Tif2 system under any conditions of ligation (V. Georget and J.C. Nicolas, unpublished results). Moreover, the fluorescent proteins contain fluorophores in a protected environment and do not participate in the structure of the receptor. Rather these fluorophores are attached by a peptide linker to the N-terminus and are much less likely to be quenched by interaction induced changes in protein structure than a small covalently attached dye molecule[75,96] . We also assumed that the eYFP did not contribute significantly to the blue channel, given its red-shifted spectrum.

The concentrations of the eCFP-AR and eYFP-Tif2 for the data in Figure 2.5 are given in Table 2.1, along with those corresponding to FCS data obtained for several different cells in two different transfection experiments. The total concentrations of eCFP-AR and eYFP-Tif2 vary by a factor of about 20-30 for the different cells imaged. The fractional complex formation is calculated with respect to the species of lowest total concentration (the limiting partner). On average for all of the cells imaged, the degree of binding is 81 ± 9 % in presence of agonist and 56 ± 5 % in presence of antagonist.

The time-dependence of both the auto and cross-correlation functions was clearly heterogeneous. The auto and cross-correlation curves could be reasonably well fit in all cases using two diffusing species, one reasonably fast, between 5 and 7 $\mu m^2/s$, and the other about 10-fold slower. No obvious difference in diffusion times could be observed as a function of ligation state for this slow component. Distinguishing by diffusion times complexes that differ in their molecular weight by a factor of 2 is possible *in vitro*, but the heterogeneous nature of the intra-cellular environment precludes such sophisticated analysis *in vivo*. This limitation underscores the difficulty of interpreting diffusion in live cells, and reinforces that notion that G_o, the amplitude at time t=0 of the cross-correlation signal can be more reliable than time-dependence for determining complex formation.

Table 2.1. Free protein and complex concentrations derived from analysis of the correlation amplitudes of AR-Tif2 studies. The errors were usually aroung 5%.

	[CFP-AR] (μM)	[YFP-Tif2] (μM)	[Complex] (μM)	% complex $[AR]_{total}$	% complex $[Tif2]_{total}$
Agonist					
(Figure 2.6)	0.3772	1.828	3.529	90.3	
	6.794	1.864	5.504		75
	1.813	0.1799	0.5592		76
	8.377	3.956	8.226		68
	2.967	10.04	12.85	81	
	2.966	0.4697	1.778		75
	2.937	0.1045	2.172		95
antagonist					
(Figure 2.6)	3.272	2.726	2.765		50
	4.054	1.844	2.211		55
	5.907	1.673	1.999		54
	6.158	1.726	1.941		53
	4.902	1.226	2.317		65
	8.771	4.050	5.065		56

2.4.1.3. Conclusions for AR and Tif2 studies

We provide here direct, quantitative measurements of the ligand-dependent interaction between AR and one of its physiological co-activators, Tif2, in live cells. Future studies will be carried out using fluorescent protein fusion pairs that eliminate cross-talk between detection channels. This adaptation should yield even more accurate quantification of the degree of interaction between these proteins under all conditions. The mRFP and variants constructs for example, were not available to us when we began this study[106,107]. A pair such as eCFP / mCherry would eliminate bleed-through phenomena that limited the accuracy of initial measurements. In spite of measurable cross-talk, the present results demonstrate that quantitative direct protein-protein interaction measurements can be carried out for nuclear receptors and their partners in living cells. These measurements using TPTCFCCS are more reliable than FRET, since they do not depend upon absolute or relative intensities or quaternary structures with inter-fluorophore distances within 7 nm.

Interestingly, we find that in the presence of antagonist, the interaction between AR and Tif2 is not eliminated. While the AF2 (Activation function 2) of the AR Ligand Binding Domain (LBD) is relatively weak; AF2 nonetheless binds to another member of the p160 co-activator family (SRC-1) in an agonist-dependent fashion[108]. However, even in the absence of the LBD, the N-terminal AF1 of AR also can interact with SRC-1 in a ligand-independent manner through the glutamine-rich motif present in the AR N-terminus[108]. This AR-AF1–Tif2 interaction is likely to be responsible for the significant degree of complex formation we observed in presence of the antagonist, casodex.

The possibility of performing quantitative determination of protein-protein complex formation in living cells in response to the addition of a drug opens a multitude of avenues for studying the therapeutic targets where protein-protein interactions play an important role. Such studies will be clearly useful in the detailed characterization of the structure-function relationships underlying the activity of pharmaceutics or other ligands. One could also imagine that such measurements could be used to determine the effective concentration of drugs in various cellular compartments, via their ability to promote or to abolish complex formation, as the case may be. TPTCFCCS may also be used to infer the influence of protein or other cofactors necessary for ligand function.

Expression levels of endogenous proteins could be determined, as well, through competition assays with the fluorescent proteins. In any case, given the importance of investigating the interactions of nuclear receptors with their multiple partners in the cellular environment, we expect that this relatively new technique (that allows direct access to free and bound concentrations in any desired cellular location) will prove to be extremely useful in investigating the functional mechanisms of ligand dependent transcription factors.

2.4.2. C-myc studies

2.4.2.1. Overview of c-myc regulation

C-myc is itself a highly regulated protein in charge of regulating many genes involved in the cell cycle, including cell growth, proliferation and apoptosis. C-myc belongs to a family of transcription factors that contain basic helix-loop-helix motifs and leucine zipper domains[109] which control cell growth and proliferation. C-myc needs

Max[110,111], also a member of the b-hlh family, to dimerize (as a tetramer of heterodimers) and bind to DNA specifically to the E-box sequences (CAYGTG) with transcriptional co-activators and their associated histone acetyltransferases or ATPases/helicases[111] in the promoter target genes[112]. C-myc is recognized to have the ability to activate and repress transcription[113,114] through direct protein-protein interactions with the transcriptional machinery. As expected, c-myc is tightly regulated by many mechanisms (i.e. the proteasome system[115]) and its deregulation is important in cancer[116].

The gene, MYC is considered an oncogene since in cancer, any disturbance of Myc regulation or function is considered to be the necessary angiogenic (blood vessel formation) switch. Interestingly, in normal cells, too much Myc pushes cells toward apoptosis through well known regulatory paths including the Bcl-2 family of proteins (at multiple levels) inside mitochondria and the ER[117,118].When conditions are favorable, the c-myc gene is one of the first to be activated producing a cascade in gene regulation. Its levels are known to be very stable through the cell cycle, despite its short lifetime of 20-30 minutes[119], until cell division when the daughter cells receive half the c-myc in the parent cell. Studies have shown that there is a short lived increase (up to five fold) in the total concentration of c-myc after a variety of stimuli including the inclusion of serum in the medium[120]. C-myc's mechanisms of regulation have been studied and are well documented.[1] For example, c-myc activity is not necessary for the survival of the cell, but its inactivity can increase the proliferation time threefold[121].

Unfortunately, very little work has looked at the c-myc levels *in vivo*. Relevant to studies presented in this chapter, recent results suggest that c-myc can have more than one source and can be divided into different populations at high concentration levels.

Tworkowsky *et al.*[122] argue that there are two populations that can be considered 'stable' and 'unstable' depending on their rate of degradation.

Also, Arabi *et al.*[115] propose that when c-myc concentration is high, c-myc co-localizes with the nucleoli. In the same study, FRAP and FLIP experiments demonstrated an 84% mobile fraction with a half life of 6 minutes, indicative of a very large complex or stable interaction with the nucleolus. They come to the conclusion that one of the possible regulatory mechanisms of c-myc is sequestration by the nucleoli, with futher degradation with proteasomes, leading to a long lived but dynamic interaction.

Fluorescence Correlation Spectroscopy (FCS) measures the fluctuations of concentrations in small volumes. In fact, the smaller the concentration that can be observed the larger the fluctuations that can be recorded and consequently the larger the signal. Hence the maximal correlation (G_o) is inversely proportional to the total concentration. For a protein expressed at the nanomolar level, like c-myc, FCS is one of the best methods available to detect dynamics *in vivo*.

2.4.2.2. Results of c-myc studies

2.4.2.2.1. C-myc steady state expression

Our first goal was to reliably detect the low levels of c-myc-eGFP in the MEF cells. We did this by using a narrow eGFP filter and exciting in the red at 970nm (hoping to avoid autofluorescence. We were careful to note the amount of autofluorescence that could be

Figure 2.7 MEF cells with eGFP-c-myc excited at 800 and 970nm. A) MEF cells with c-myc-eGFP excited at 800nm. B) Same cells excited at 970nm, this cell contains about 20nM of c-myc-eGFP by FCS. Note the diminished autofluorescence and the increased signal due to eGFP (barely visible). Red arrows point to general locations of nuclei.

A)

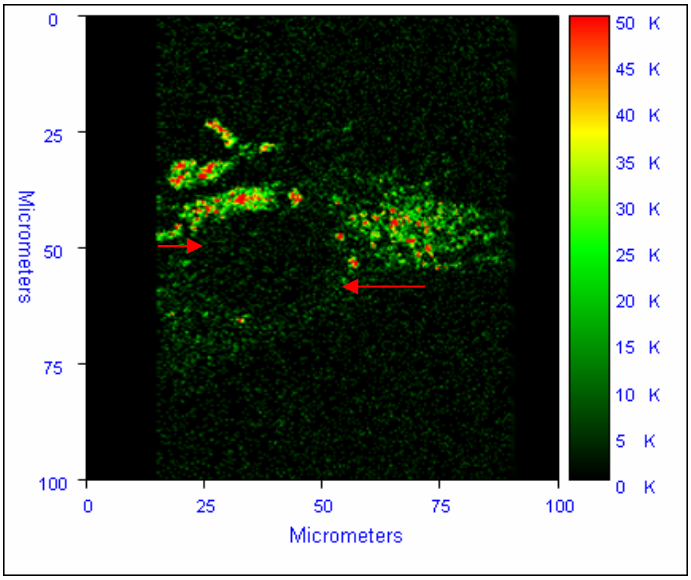

B)

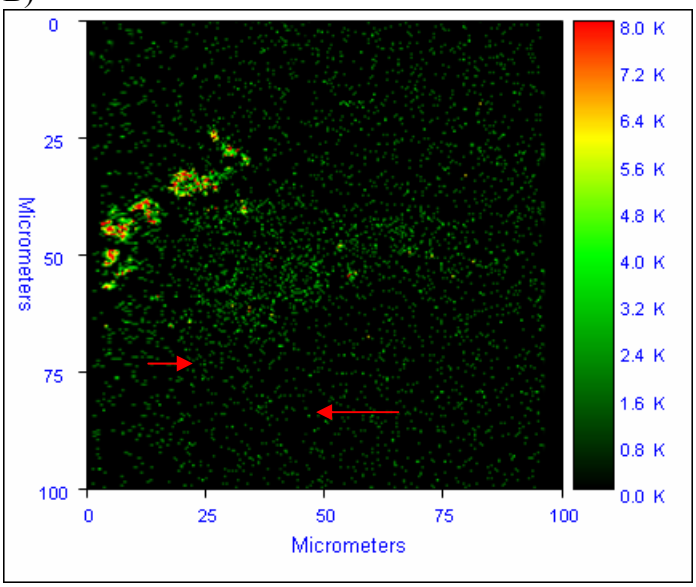

detected through a filter and noticed that in the nucleus there was very little autofluorescence signal (Figure 2.7a). As seen in Figure 2.7b, a high resolution scan was able to barely see the c-myc-eGFP present after 30 minutes in a serum stimulated MEF cell.

Figure 2.8. Autocorrelation function of MEF eGFP-cmyc. A) ACF of a MEF eGFP-c-myc cell excited at 970nm. The wildtype MEF (control/standard) has no clear ACF (in black). B) The two component fit performed for eGFP-cmyc ACF is shown.

A)

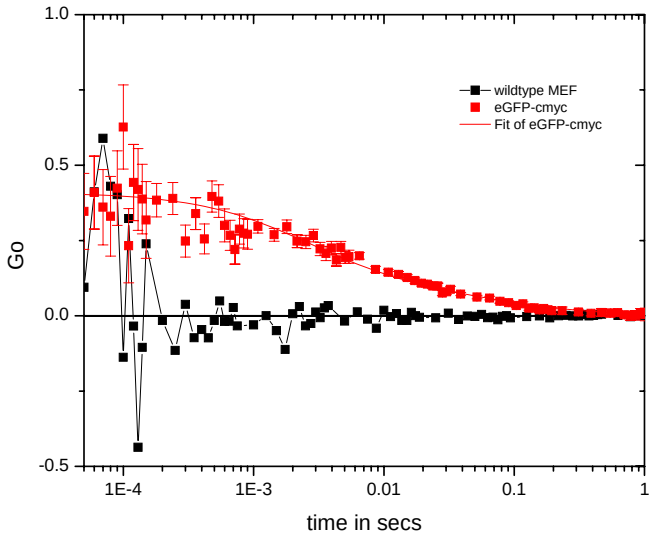

B)

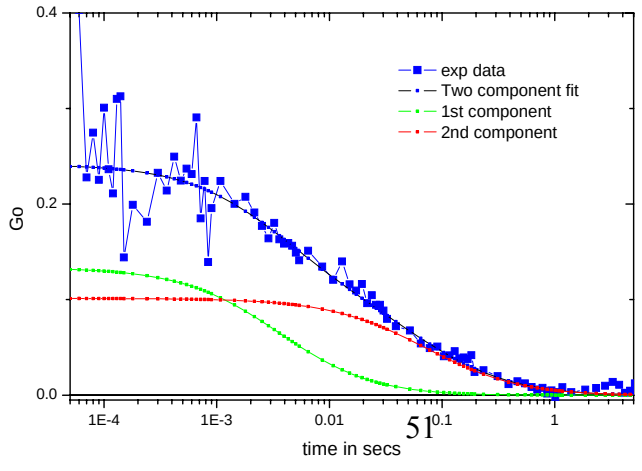

Note though that this level was higher than the steady state level measured (11 ± 2 nM). By using FCS (at very low powers), we were able to detect c-myc-eGFP at very low concentrations without causing visible damage to the cell or bleaching of the fluorophore. Figure 2.8a is the ACF of the c-myc-eGFP protein of a wild-type MEF. Note the long "tail" in the ACF of the c-myc-eGFP protein. At 970nm excitation, cells exhibiting weak autofluorescence had no apparent correlation (Figure 2.8b). We found that there are very stable populations of c-myc-eGFP in these MEF cells that can be divided according to their different diffusion coefficients. The two characteristic diffusion coefficients can be extracted reproducibly from the ACFs of different cell nuclei. Since the fitting of the data did not support a third component by use of a t-test, we chose to maintain two fractions, one 'mobile' and one 'less mobile'. This decision was made despite the fact that the "tail" could be very smooth at times pointing to multiple diffusion coefficients or other dynamic processes including binding. Figure 2.8b contains the ACFs for the two separate components with the appropriate $G_i(\tau)$'s; we described them as a 'faster' more 'mobile' fraction and a 'less mobile' or 'immobile' fraction. The diffusion coefficient recovered were 5.5 ± 0.93 μm^2/sec for the mobile fraction and 0.2 ± 0.06 μm^2/sec for the immobile fraction. Assuming a viscosity inside the nucleus of 4 cP[123], corresponding molecular weights can be calculated to be in the millions of Daltons. This result suggests that both fractions are either restricted somehow in their motion or in direct contact with chromatin. We believe the latter to be true and plan to examine this binding via the modulation of the protein Max in our upcoming studies. Since Max is necessary for c-

myc to bind to chromatin, we plan to block this step using siRNA, turning off production of Max protein in vivo.

Interestingly, Tworkowski *et al.* found that their 'unstable pool' contained MEK2 protein, which localizes exclusively to the cytoplasm and found histone H3, a core component of chromatin, in their 'stable pool'. This result suggests that both fraction we measured appear to be their 'stable' pool since the stable pool was enriched with chromatin. They suggest that their separation appears also at low levels of expression (endogeneous). Since their separation involved differential detergent extraction, quantifying relative populations of the two pools was not attempted or reported.

In some experiments, we used protein concentrations high enough to observe localization of c-myc in nucleoli as seen by Arabi *et al.* The original authors suggest that c-myc is sequestered at the nucleoli where proteasome degradation occurs. Unfortunately, we could not measure FCS at these locations because the intensity during correlation collections decreased due to bleaching, pointing to immobilization (e.g. massive clustering).

2.4.2.2.2. C-myc concentration over time

We also studied the accumulation of eGFP-c-myc over time after serum stimulation. The addition of drug MG132 was used to prevent the normal degradation of eGFP-c-myc, allowing us to follow the accumulation for 6-7 hrs. The results are shown in Figure 2.9, and match what is seen in the biochemical literature done by Mehmet *et al.*[124] There is a peak at 2-3 hrs for the cells without MG132 (with an increase of about 30% from the final steady state level of about 8 ±1.3 nM after 8hrs). For those with MG132,

we see further increase of the eGFP-cmyc concentration, with a peak at about 3 hrs and increasing again later. Also, the concentrations of both fractions increase; but the more mobile fraction rapidly becomes dominant.

Figure 2.9. The c-myc concentration of MEF cells treated (red) and non-treated (black) with MG132 over a period of 6-7hrs.

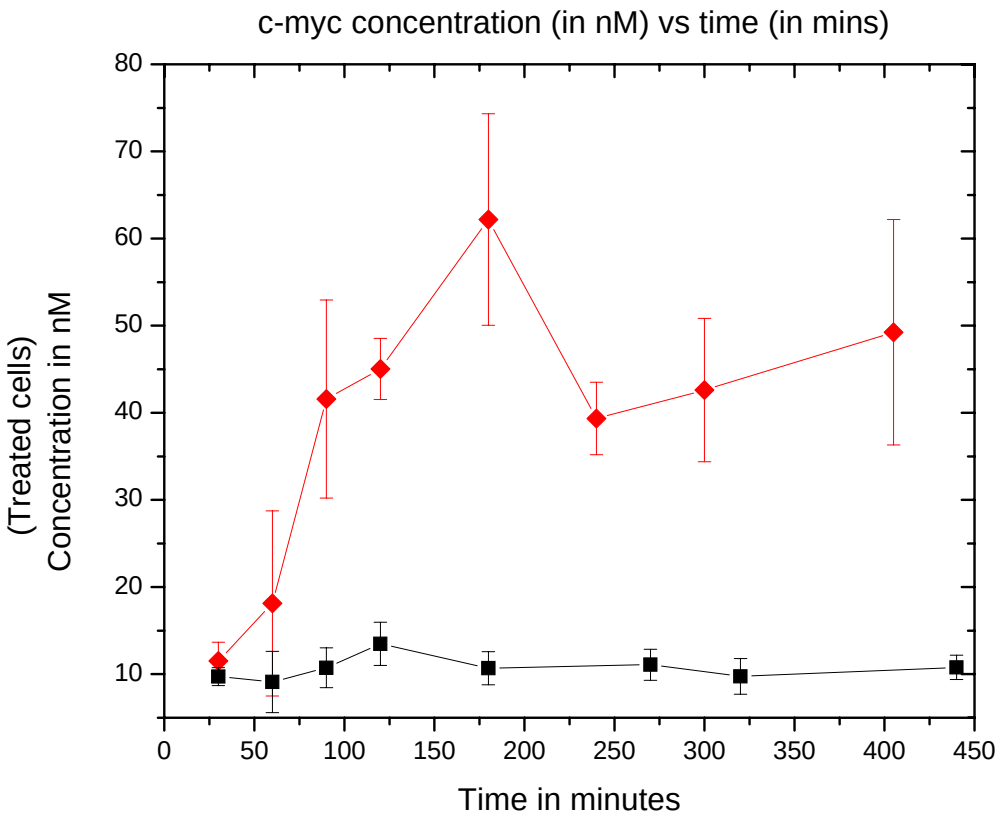

2.4.2.2.3. Bound vs. freely diffusing fractions

Figure 2.10a shows the apparent change in populations in three different cells manipulated to produce different concentrations of c-myc-eGFP. These manipulations included transient transfections of eGFP-cmyc to a wild-type or to the homozygous MEF cell line. The low levels of expression are demonstrated by Figure 2.10b, where a cell containing 100nM of c-myc-eGFP is barely visible. The image was taken at a 1 ms/pixel resolution (256 x 256 pixels). As can be seen in Figure 2.9c, the more "mobile" fraction increased with total concentration; while the "immobile" fraction remained nearly constant. At 100 nM, the more mobile fraction represents >90% of the total c-myc concentration.

Figure 2.10. Bound vs. freely diffusing fractions of eGFP-c-myc. A) ACF of three MEF cells with different concentrations of eGFP-cmyc. The concentrations are 10 (blue), 94 (red) and 400nM (black). All three ACFs have been normalized to G(blue) at t=1e-3 secs. B) Image of MEF cell at 970 excitation containing about ~100nM of eGFP-cmyc (high resolution,false color). C) The fractions of the mobile and immobile fractions obtained from several transfections of wild type and homozygous cells as a function of total increasing concentration.

A)

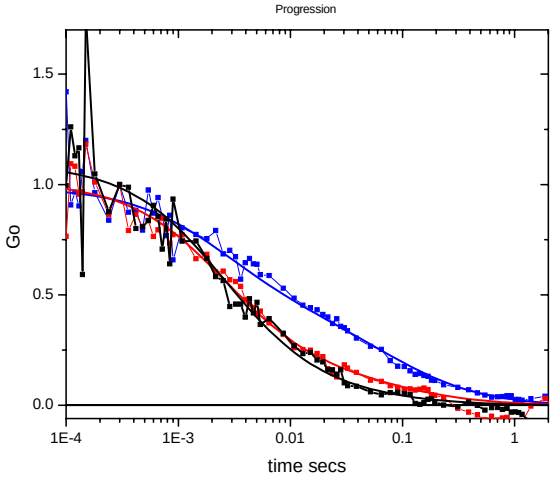

B)

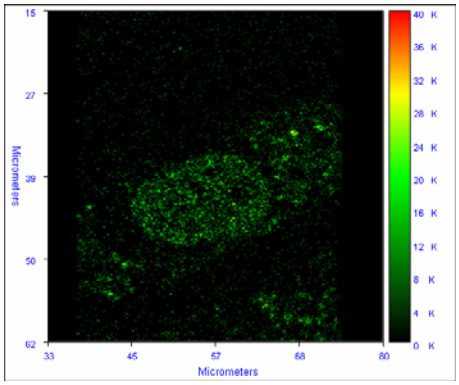

C)

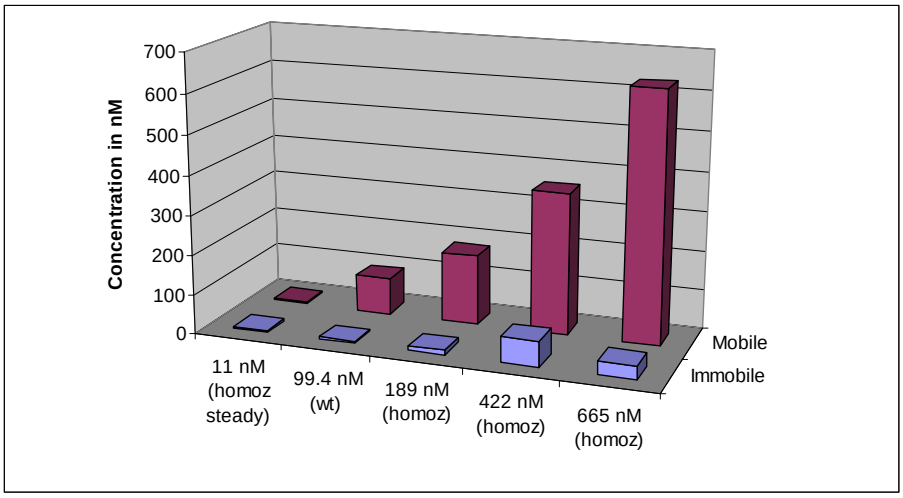

2.4.2.3. Conclusions for c-myc studies

We demonstrated the ability of FCS to measure *in vivo* very low (nM) levels of GFP-tagged c-myc. We were able to demonstrate an immobile fraction is present (probably chromatin bound) that, at few nM levels, must be an important pool in the regulation of the c-myc protein. There appeared to be saturation of those immobile c-myc sites when large concentrations of protein were introduced; this brings into question the use of over-expressing plasmids for c-myc. Because cancers often over-express c-myc, these results indicate a fundamental difference between c-myc dynamics in normal versus malignant cells.

We were able to reproduce features of the time profiles previously seen, e.g.: peak of about 2-3 hours of [c-myc] and the accumulation of c-myc in the presence of MG132. Further analysis will include the possibility of including anomalous diffusion, binding kinetics ("long tail") or using molecular biology techniques to disrupt c-myc/max interactions. Mehmet *et al.*[124] measurements performed by ELISA demonstrated that ~450 molecules of c-myc per cell are required in swiss 3T3 fibroblasts at steady state levels. To put the measured values of ~8 ± 1.3 nM in perspective, approximating the volume of a typical MEF nucleus as ~100 fL, gives approximately 600 molecules per cell.

Chapter 3: Molecular Dynamics Simulations of Perylene and Tetracene Librations: Comparison With Femtosecond Up-conversion Data

3.1. Introduction

The topics in this chapter were published[61] in 2008 and are mostly reproduced here.

3.1.1. Background

Historically, there has always been great interest in understanding the interactions of how a solute moves through its surroundings. Many techniques exploring different aspects of the transport properties of molecules in solution exist today, including NMR, light scattering, analytical ultracentrifugation and, in our case, fluorescence spectroscopy. Fluorescence spectroscopy is a well known technique used to measure the two transport properties of interest to many involved in protein interactions, the translational and rotational diffusion coefficients. In this Chapter, we will show how time resolved emission anisotropy (TREA) can measure rotational motion of molecules in solution and how classical molecular dynamics simulations can provide essential confirming information and unique molecular level insight into the origins of rotational diffusion.

3.1.2. TREA

In time resolved emission anisotropy, a brief light pulse is used to excite fluorescent molecules in a portion of a solution containing them, photoselecting a population with oscillators generally aligned with the excitation polarization axis.

Subsequent emission anisotropy decay is due to the ensemble of fluorescing molecules losing this initial alignment (especially due to rotational diffusion). The alignment decays with multi exponential time constants, and the time dependent emission anisotropy data obtained are fit to a sum of exponentials with a set of corresponding pre-exponential coefficients. These parameters subdivide the total fluorescence anisotropy. In non-viscous solvents such as water, small molecules may rotate in tens of picoseconds, meaning that very fast probing techniques are needed in order to observe the decay of their initial alignment with the exciting light pulse.

Time-resolved fluorescence emission anisotropy measurements are widely used to provide information on the dynamics of molecules in solution, and they have been recently extended to femtosecond resolution. Perylene (an oblate molecule) and tetracene (a prolate molecule) are planar molecules that have well defind "in-plane" and "out of plane" rotations[125] that may be discerned in emission anisotropy decay (See Figure 3.1). "In-plane" rotations occur along the molecular plane and "out-of-plane" rotations are perpendicular to the molecular plane.

Perylene anisotropy in viscous solvents had long been observed to have a bi-exponential decay on the nanosecond scale.[125,126] Prior experiments with > 100 ps resolution have frequently yielded $r_o < 0.4$, the so called "r_o defect".[126] The theoretical limit for the emission anisotropy (r_o) of parallel S_1 and S_o transition moments is 0.4. With femtosecond sum frequency generation (up-conversion) experiments, we are able to obtain a clearer picture of small molecules in solution, and are now able to time-resolve most of the "r_o defect" previously seen and/or speculated about in many reports. Earlier work by Brand *et al.*[126] pointed out that the pre-exponential associated with the in-plane

rotation is less than the expected 0.4 and the defect might be associated, as we observe, with an ultrafast in-plane rotation. The first few picoseconds can now be probed in great detail compared to previous analyses of perylene anisotropy decay.[126-131] Up-conversion permits observation of very fast motion of molecules in solution, down to perhaps 15% of laser pulse widths (which may themselves be ~200 fs). Motions of probe molecules such as perylene contain details of solvent structure that could not be observed with multipicosecond or nanosecond resolution.[129,132,133] Perylene may have solvent

Figure 3.1. A top view of the stick structures of perylene and tetracene. Perylene is shown on top and tetracene on bottom. Both structures have been geometrically optimized in GAUSSIAN 2003. "In-plane" rotations occur along the aromatic bonds plane. "Out of plane" motion is perpendicular to the molecular plane.

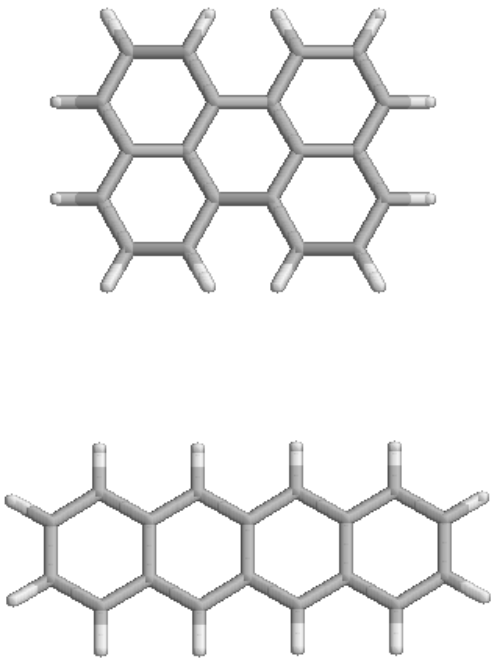

dependent variations in the character of its rotational motion. For example, perylene has previously been observed to follow "stick" boundary conditions in one type of solvent and then follow slip-like behavior in other solvents.[132] Further, perylene has been shown to make a transition from apparent "stick" boundary conditions to "slip" boundary conditions as the chain length increased in an n-alkane series of solvents.[134] Others reports claim that perylene and tetracene have sub-slip (faster than slip) behavior in alcohols that can be explained in the context of local solvent structures.[135]

The rotational relaxation of perylene and tetracene in hexadecane and glycerol has been measured in our lab using femtosecond upconversion fluorescence spectroscopy[60]. The theoretical value of 0.4 cannot be attained when these data are fit with a bi-exponential model. A third rotation term of ~500 fs has been found that is essentially independent of temperature and viscosity. This very fast rotation is believed to mostly be due to an "in-plane" femtosecond libration, or low frequency torsional motions, of molecules within their solvent pockets. Brocklehurst *et al.*[131] have described this libration as a more limited range rotation, (equivalent to slow libration) with the observation that out-of-plane rotations were more restricted in alcohols than in alkanes. The source of this libration, not observed directly on nanosecond time scales, has not been determined. Prior to the results of the picosecond experiments, researchers suggested that the r_o defect was oscillator dislocation rather than libration.[130] We have used molecular dynamics simulations to determine whether the defect is a reasonable consequence of rotations that yield little solvent displacement.

3.2. Theory

The results obtained from the various techniques exploring molecules in solution, like fluorescence spectroscopy, are usually analyzed by imposing a specific hydrodynamic model for comparison with experiment. The most basic hydrodynamic model is based upon the Einstein equation[136] that relates the friction coefficient "f" of a particle to its diffusion coefficient D:

$$D = \frac{k_B T}{f} \tag{3.1}$$

where k_B is the Boltzman's constant and T is the temperature. One of Einstein's insights was to relate the friction coefficient in Eq. 3.1 to the velocity dependent forces felt by small particles in solution, commonly known as Brownian motion.

The friction coefficient in Eq. 1 may be obtained by first calculating the force felt by a particle in solution using the Navier-Stokes equation[137,138] which is derived from the energy and momentum balance equations:

$$\rho\left(\frac{\partial}{\partial t} + \vec{u}\cdot\vec{\nabla}\right)\vec{u} = \rho\vec{K} + \eta\nabla^2\vec{u} + (\frac{\eta}{3} + \kappa)\vec{\nabla}\cdot\left(\vec{\nabla}\cdot\vec{u}\right) - \vec{\nabla}p \tag{3.2}$$

where ρ is the density, u is the velocity, K is the body force, η is the shear viscosity, κ is the bulk viscosity, p is the pressure and ∇ is the del operator. Eq. 3.2 applies to a particle submerged in a fluid that does not deform under pressure (a continuous incompressible Newtonian fluid) achieving a constant velocity under non-turbulent flow (commonly known as creeping or laminar flow). These conditions are satisfied at a small Reynolds

number. The Reynolds number is a dimensionless quantity given by $2\rho au/\eta$[139], where ρ, u and η are the density, mean velocity and viscosity of the fluid in a 'tube' of radius a. The Navier-Stokes equation simplifies to:

$$\rho \frac{\partial \vec{u}}{\partial t} = \rho \vec{K} + \eta \nabla^2 \vec{u} - \vec{\nabla} p \tag{3.3}$$

because an incompressible fluid is divergence free, i.e. $\nabla \cdot u = 0$. For small flow velocities, as in our case, the time derivative of the flow velocity u can be neglected. With the absence of any external force on the particle, we obtain the Stokes equation:[137]

$$\eta \nabla^2 \vec{u} - \vec{\nabla} p = 0 \tag{3.4}$$

which can be solved for the total force on the immersed particle. This force is exactly the amount of force needed to keep the particle stationary in a moving fluid. The friction arises from viscous resistance of the fluid to the movement of the particle (i.e. a sphere) and has a strong dependence on the particle's shape (calculated by Stokes for a sphere[140] and by Perrin for ellipsoids of revolution[141]). Using the Navier-Stokes equation, we obtain the appropriate friction coefficient depending on the type of interactions that the solute (i.e. sphere) has with the solvent.

Depending on boundary conditions[138] imposed on the interaction between the solvent and the solute, hydrodynamic theory for molecules in solution is often separated into two categories. "Stick" boundary conditions describe when the solute "drags" some of the solvent molecules with it as it diffuses in the solvent (usually a term imposed when the solute is larger than the solvent, i.e. so the solvent exhibits continuum behavior). Note that an underlying assumption is that the particle is in the "infinite dilution" limit. For Eq. 3.1, the friction coefficient for translation of a sphere under the "stick" condition is given

by $f=6\pi\eta r$ where η is the viscosity of the solvent and r is the radius; the comparable friction coefficient for rotation is given by $f=8\pi\eta r^3$. The natural units for the translational and rotational diffusion coefficient are then [Length]^2/[Time] and 1/[Time] (Hertz) respectively. Since hydrogen bonding is present, solvation in water is usually considered to cause "stick" boundary conditions. “Slip” boundary conditions apply when the solvent “rolls” on the surface of the solute and there is very little interaction between the two, usually occurring when solute and solvent are about the same size. An example is solvation, the attraction and association of molecules of a solvent with molecules or ions of a solute, of hydrophobic solutes in hydrocarbon solvents of larger size. Since there is very little interaction between solute and solvent, small rotations can occur with very little physical displacement of the solvent. Under “slip” conditions, the translational and rotational friction are given by $f=4\pi\eta r$ and $f=0$ respectively. For a perfectly slipping sphere the “slip” rotational diffusion coefficient (Eq. 3.1) becomes infinite. A third behavior can be thought of occurring when the solute rotates in gaps between the solvent and the solute molecules allowing for “sub-slip” rotation. At this shorter timescale, the structure of solvent pockets surrounding the solute molecules (and the gaps in between) increase in relevance. The application of hydrodynamics gives us clues about the interaction of the molecule with the surrounding solvent, the movement of the molecule and the structure of the solvent itself.

We can represent a generalized ellipsoid with different semi-axes[142], $a \geq b \geq c$ having relaxation times ρ_a, ρ_b, ρ_c with rotational friction coefficients C_a, C_b, C_c and rotational diffusion coefficients D_a, D_b, D_c. The diffusion coefficients and the friction

coefficients can be related in the same manner as in Eq. 3.1. The relation between the diffusion coefficients and the relaxation times is given by Perrin's formulae:[56]

$$D_a = \frac{1}{2}\left[\frac{1}{\rho_b} + \frac{1}{\rho_c} - \frac{1}{\rho_a}\right]$$
$$D_b = \frac{1}{2}\left[\frac{1}{\rho_a} + \frac{1}{\rho_c} - \frac{1}{\rho_b}\right]$$
$$D_c = \frac{1}{2}\left[\frac{1}{\rho_a} + \frac{1}{\rho_b} - \frac{1}{\rho_c}\right] \qquad (3.5)$$

As shown in Eq. 3.6, the emission anisotropy decay of a general rigid ellipsoid is described by a sum of five exponential terms:[143,144]

$$r(t) = \sum_{i=1}^{5} \beta_i \exp(-t/\varphi_i) \qquad (3.6)$$

where β_i are trigonometric functions of the angles between the transition dipoles and the symmetry axis of the ellipsoid and ϕ_i are the rotational correlation times. The five exponential terms are given by:

$$\varphi_1^{-1} = 3D + 3D_a$$
$$\varphi_2^{-1} = 3D + 3D_b$$
$$\varphi_3^{-1} = 3D + 3D_c$$
$$\varphi_4^{-1} = 6D - 2\Delta$$
$$\varphi_5^{-1} = 6D + 2\Delta \qquad (3.7)$$

where $D = (D_a + D_b + D_c)/3$ and $\Delta = (D_a^2 + D_b^2 + D_c^2 - D_a D_b - D_a D_c - D_b D_c)^{1/2}$

Since we are modeling molecules as ellipsoids of revolution, rotation about the unique axis in either a "prolate" or an "oblate" object is called $D_\parallel$ and the rotation along either of the other axes is referred to $D_\perp$. Additionally, we can make the simplification

that these five correlation times collapse to three for an axisymmetric ellipsoid, they are given by Eq 8:[144]

$$\varphi_1^{-1} = 6D_\perp$$
$$\varphi_2^{-1} = 2D_\perp + 4D_{||}$$
$$\varphi_3^{-1} = 5D_\perp + 1D_{||} \qquad (3.8)$$

Note that the first and third correlation times are very close to each other, making them practically indistinguishable. Hence, the anisotropy for an axisymmetric ellipsoid can be described adequately with two amplitudes and two rotational correlation times.[126] The β_i's, pre-exponential factors, are found to depend only on properties of the solute; i.e., the directions of the absorption and emission dipole. This model permits us to relate in-plane (aromatic bond plane) and out-of-plane motions to a specific set of amplitudes and correlation times.

The emission anisotropy decay of a system, r(t), is still calculated in the same way[127,128]; r(t) is obtained from measurements of the decays with parallel and perpendicular polarization with respect to the excitation direction:

$$r(t) = \left(\frac{I_{||}(t) - I_\perp(t)}{I_{||}(t) + 2I_\perp(t)} \right) \qquad (3.9)$$

The theoretical limit for the initial anisotropy, r_o, is 0.4 for single photon electronic transitions in fluorophores. An anisotropy of 0.4 indicates that the absorption and emission moments are collinear:

$$r_o = 0.2(3\cos^2\delta - 1) \qquad (3.10)$$

where δ is the angle between the absorption and emission transition moments. If instead of this intramolecular angle between oscillators, we use γ as the angle between the initial

excitation axis and the ultimate emission axis at time t, we obtain the emission anisotropy decay function for the ensemble:

$$r(t) = \left\langle 0.2(3\cos^2 \gamma(t) - 1) \right\rangle \tag{3.11}$$

3.3. Molecular Dynamics

Molecular dynamics (MD) is a classical computational method for calculating the time dependent behavior of a system. In order to calculate the position and velocities of all the atoms at a specified time step, algorithms are used to numerically integrate Newton's second law. The method used to calculate the positions of the atoms in these simulations is called the "leap-frog" Verlet algorithm: all the atomic positions at a time t and all the velocities v at intermediate times are obtained. The algorithm name arises from the way in which positions and velocities are calculated in an alternating sequence, "leaping" past each other in time. The initial positions are obtained from a minimized structure and the velocities are given by the desired temperature. To maximize the time step size, the bond lengths of certain atom pairs, like those involving hydrogens, can be fixed; effectively removing the highest frequency motions from the calculation. A harmonic approximation is used for the bond and the bond angle potentials and the dihedral angle (torsion) potential is a four atom term based on the dihedral angle about an axis defined by the middle pair of atoms. Because of the large number of bonds involved and in order to decrease the computational time, molecular dynamics simulations make use of cutoff distances to approximate the nonbonded interactions needed to calculate the energies. The calculation requires the compiling of a non-bonded list every so many time steps. The CHARMM program[145] models all non-bonded interactions by a sum of

effective pairwise-additive Lennard Jones (LJ) and Coulomb energies, commonly terminated at a specific distance from the atom exerting the forces. Switching functions for both the LJ and Coulomb potentials allow the potential to smoothly reach zero over a specified range and shift functions that alter the potential gradually over a long distance.[146]

In order to maintain the required temperature and pressure (depending on the chosen ensemble), coupling to a particular thermostat or bariostat is necessary. For example, the coupling of a heat bath is represented by stochastic impulsive forces (Langevin piston[147]) that act occasionally on randomly selected particles. If the particle is chosen to undergo a collision, the new velocity is obtained from a Maxwell distribution. In this case, the particles are subject to rapidly varying random forces.

MD is used to determine detailed information of the movement of molecules in solution including conformational changes. MD simulations provide a microscopic picture of molecular diffusion.[129] The extraction of rotational relaxation data from the angular correlation function is an application of MD. The angular correlation function is defined as:

$$C_2(t) = \frac{\left\langle 3(\vec{n}(0) \bullet \vec{n}(t))^2 - 1 \right\rangle}{2} \tag{3.12}$$

where $\vec{n} = \left(n_x, n_y, n_z\right)$ is a vector rotating with the molecule at time t. For excitation and emission oscillators aligned along the same molecular axis, anisotropy decay can be related to the correlation function by:

$$r(t) = \frac{2}{5} C_2(t) \tag{3.13}$$

Here $C_2(t)$ is the angular correlation function of the emission dipole. Since we are approaching the same timescale of solvent-solute collisions, the motion that we seek to describe may not follow an exponential decay; instead, it may have quasi-ballistic behavior[148], almost freely rotating with no resistance.

Perylene is an ideal molecule for these studies since it is amenable to excitation into states with different initial transition moment directions (i.e., $\beta=0$ or $\sim \pi/2$ in Eq. 3.11 above). The model of perylene as a rigid molecule was used initially in our molecular dynamics calculations, because fluorescence depolarization theory above only applies to a rigid ellipsoidal molecule. It is also known that perylene becomes more rigid in the first excited state[149], helping to justify our use of a rigid perylene molecule in the molecular dynamics simulations.

Other explanations for the possible r_o defect that we consider are vibrational coupling for tetracene reported by Sarkar[150] *et al.* and the work by Szubiakowski[151] *et al.* that examined the possible non-planarity[152] of perylene in either the ground or first excited states. In the following sections, we present simulations of perylene and tetracene in a hexadecane box using molecular dynamics, and we directly compare these results to our earlier upconversion anisotropy data.[60]

3.4. Methods

3.4.1. Simulations

We used the CHARMM[145] (Chemistry at HARvard Molecular Mechanics, version c29b2) program to determine the source of the rotation ("libration") by calculating autocorrelation functions and thermodynamic properties. This study used the high-

performance computational capabilities of the Biowulf PC/Linux cluster at the National Institutes of Health, Bethesda, Md. (http://biowulf.nih.gov). The charges and topology of perylene are taken from Jas *et al.* [129] The tetracene structure used was obtained from an energy minimization of the geometry optimized structure of tetracene using GAUSSIAN 03[153]. The atomic charges were obtained from the Mulliken population analysis of the HF/6-31G* optimized structure. Using CHARMM, geometry optimizations were performed on the pure solvent alone. We used a dodecahedral box with periodic boundary conditions. In all molecular simulations, the SHAKE method (used to fix bond lengths) was used on the bonds involving hydrogen atoms. Integration of Newton's equations of motion was carried out with the Verlet leapfrog algorithm with a time step of 0.002 ps. In all energy calculations, a 14.0 Å atom based nonbonded spherical-cutoff distance was used, with a switching function between 8.0 and 12.0 Å for van der Waals terms and a force shift function at 12.0 Å for electrostatics. For simulations with explicit solvent, the relative dielectric is set constant to unity (vacuum). The nonbonded neighbor atom lists were generated every 40 steps. The temperature was held at 300K for all the initial equilibrium simulations with a window of 5K. The solute was placed in the center of the dodecahedral box and those solvent molecules that overlapped the solute were removed. The solution boxes contained one solute molecule in 508 hexadecane molecules in a cell based on a cube of side 71.05 Å. We then performed simulations corresponding to the NVT (isothermal-isochoric) ensemble with the solute fixed to allow the solvent to rearrange around the solute. The simulations were carried out for 1 ns. The temperature of the dodecahedral box was held constant at 300K by decreasing the total kinetic energy of the atoms using velocity rescaling.

Simulations on the whole system were then performed using the NPT (isothermal-isobaric) ensemble in order to extract correlation functions and hydrodynamic properties to compare with femtosecond experimental data. The average pressure was held at 1 atm using the Langevin piston method, using a piston mass of 500.0 amu and a collision frequency of $20ps^{-1}$ used to determine the decay time of the volume fluctuations and to set the damping respectively. (This method uses Langevin dynamics to control the fluctuations of the barostat). The average temperature was held constant using the Hoover algorithm[147,154]with a thermal piston mass of 1000 kcal·ps^2 and a reference temperature of 300K. This is the equivalent of coupling our solvent box to a large heat bath at 300K. Trajectories were saved every 0.1 ps for 1 ns simulation time. We used the movement of the symmetry axes of the solutes over time to determine the correlation times. A vector along the central carbons in the plane of the molecule or a vector normal to the plane was used to obtain the angular correlation function in the simulations for the "in plane" or "out of plane" results respectively.

3.4.2. Quantum mechanics.

The quantum mechanical calculations were performed using GAUSSIAN 03. The NIH SGI Origin 3400 supercomputer, known as Nimbus, was used which runs the IRIX 6.5 operating system. The crystal structure was optimized using B3LYP/6-31G** calculated energies. Normal modal frequencies of perylene were found after optimization. The two conformations with the lowest energies were chosen. These conformations represent the butterfly and twisted conformations that have been described elsewhere.[149,155] The coordinates of maximum displacement obtained from MOLDEN

(v3.6)[156] after the addition of 4kT of energy were used for the calculations. The exact energies were calculated by the HF method using a 6-31G* basis set in Gaussian 03. The excited states are obtained by single excitations from the closed shell ground state. The calculation of excited states was done using the CIS (CI-Singles) and Dunning's correlation consistent double basis set (cc-pVDZ) in GAUSSIAN 03. A full population analysis was performed with GAUSSIAN. In this way, transition moments were obtained for both conformations.

3.5. Results

The radii of gyration of both perylene and tetracene are found to be of the same order as hexadecane, implying that perylene and tetracene should fall into the "slip" regime. Perylene will initially displace little solvent as it rotates "in-plane", leading to the expectation that this rotation is quasi-ballistic[148] in nature with very little friction. Figure 3.2 shows the experimental data and simulation of perylene in hexadecane. A third exponential term was previously used to empirically fit our prior data to account for the defect in initial anisotropy, r_o. The data were fit with $r(t) = 0.24\exp(-t/21) + 0.1\exp(-t/130) + 0.05\exp(-t/0.45)$, where times are in picoseconds. The MD simulation is able to faithfully predict the initial anisotropy decline seen in perylene experiments. The insert of Figure 3.2 focuses on the first 30 ps of the perylene in hexadecane simulation, where we can clearly see the initial behavior corresponding to the "libration" in both the experiment and simulation. Figure 3.3 shows the first 75 picoseconds of the experimental anisotropy decay data of tetracene excited at 410 nm (the 0-2 band) in hexadecane and the corresponding tetracene in hexadecane simulation. The simulations reproduce features of

tetracene anisotropy decay only qualitatively. Some of the mismatch may originate in the limited time resolution of the laser pulse generating that experimental data (at a wavelength the instrument dispersion was not optimized for). Convolution with the broader "instrument response function" at this wavelength may prevent r from reaching 0.4, and the simulation also appears horizontally offset. Nevertheless, we clearly see a sub-picosecond, predominantly in plane rotation ('libration') in the simulations.

Unlike perylene with strong allowed transitions[157], that lie only on the symmetry axes, tetracene (with weakly allowed S_1-S_o[158]) has been shown by Sarkar[150] to have anisotropy decay contaminated with picosecond changes in vibrational coupling between S_1 and higher lying states. We initially discounted the effect of such coupling when inspecting experimental anisotropy decay data like that seen in Figure 3.3, but recently we confirmed the results of Sarkar in the ultraviolet and also found that excitation at 442nm (in the 0-1 band) yielded r(t) curves with $r_o < 0.4$ that differ from those shown in 3. 3. Hence the comparison in Figure 3 cannot be expected to be quantitative as in Figure 3.2; in fact, a model combining libration and vibrational cooling would be required to fully rationalize tetracene. As that is beyond the scope of this manuscript (and dissertation), we include Figure 3.3 only to show the potential contribution of a libration to that anisotropy decay profile.

Figure 3.2. Femtosecond anisotropy decay of perylene in hexadecane (●, red). The published experimental data were fitted adequately ($\chi 2$=1.1-1.3) with r(t) = 0.24exp(-t/21) + 0.1exp(-t/130) + 0.05exp(-t/0.45) where times are in picoseconds. Perylene anisotropy in hexadecane, 4ns simulation time (100 ps shown as ■, blue). The insert shows the first 30 ps.

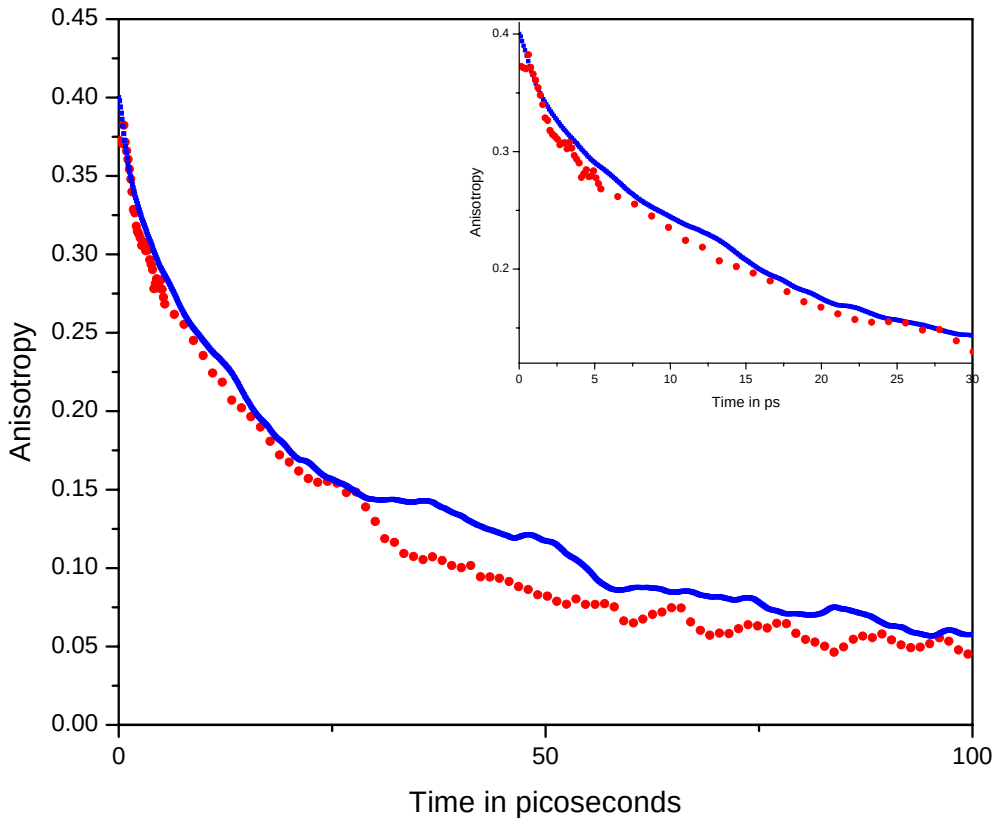

Figure 3.3. Tetracene in hexadecane anisotropy decay (●, red). The data were fitted adequately (χ2=1.1-1.3) with r_o (t) = 0.27exp(-t/10) + 0.08xp(-t/160) + 0.03exp(-t/0.6), where times are in picoseconds. Tetracene in hexadecane anisotropy simulation (■, blue). Note the experimental r(0) value does not reach the value of 0.4 but qualitatively the decay is similar. See text for details.

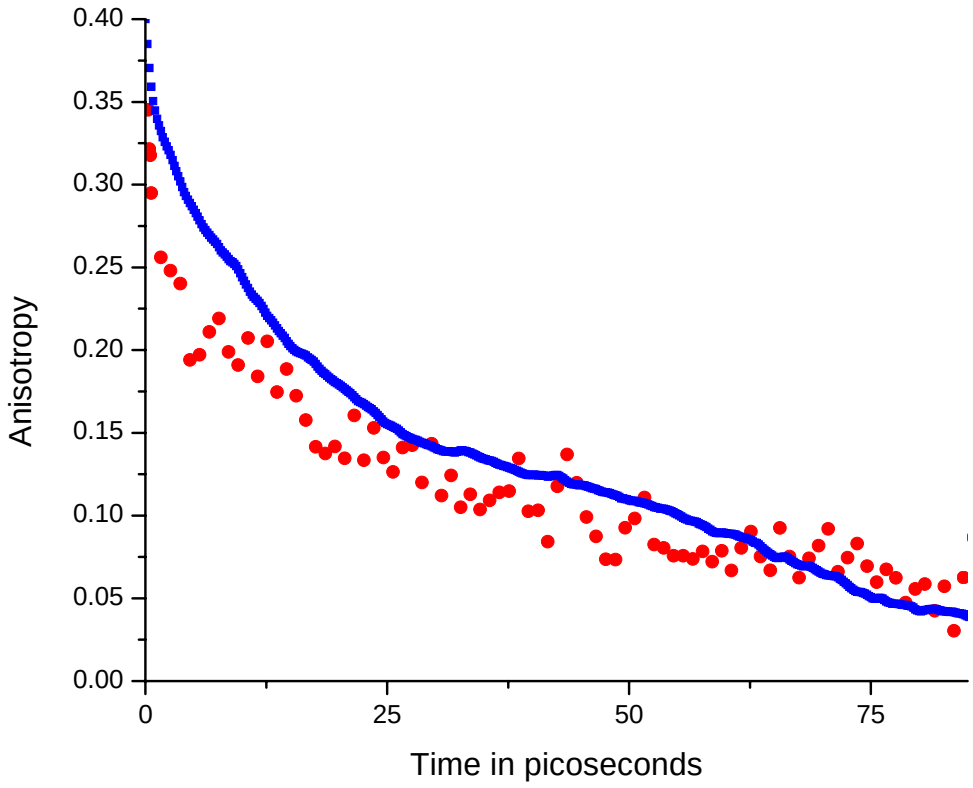

Figure 3.4 shows the twisted and butterfly conformations of perylene used for the calculations of the transition moments (shown with their maximum displacement from a flat perylene). They are shown displaced about 6° and 5° from the symmetry axis respectively. In Table 3.1, we can see that even at 4kT of energy away from equilibrium, the direction of the transition moment is essentially along the long axis in the plane of the molecule (TM_x) while the transition moment perpendicular to the plane (TM_z) is negligible for the first three excited states of both twisted and butterfly conformation. Further, the oscillator strengths for those excited states with nonzero TM_z are negligible. The angle from the symmetry axis for the twisted and butterfly conformations were about 6º and 5º, respectively. The excited states of these conformations were not found to deviate significantly from these angles. Since our calculation of transition moments inside the distorted molecule do not deviate significantly from the x-axis, we expect that even the excited state of perylene (with excess vibrational energy) will remain x-axis polarized. Our calculations find little evidence of nonrigid perylene having nonsymmetric oscillator loci.

Table 3.1. The transition moments (in AU) and oscillator strengths obtained from the quantum mechanical calculations for the first three excited states of both heavily distorted perylene configurations (twisted and butterfly).

	TM_x	TM_y	TM_z	Oscillator strength (f)
Twisted				
$S_{1,tw}$	2.800	0.000	0.0000	0.7021
$S_{2,tw}$	0.000	0.000	0.0497	0.0003
$S_{3,tw}$	0.000	0.000	0.0376	0.0002
Butterfly				
$S_{1,b}$	2.7668	0.003	0.0000	0.6916
$S_{2,b}$	0.0000	0.0000	0.0000	0.0000
$S_{3,b}$	0.0000	0.0000	0.0000	0.0000

Figure 3.4. The two conformations of perylene studied: butterfly and twisted. The butterfly conformation is on the left and the twisted conformation on the right. The conformations shown are those at maximum displacement from a flat perylene with 4kT of energy.

One final observation is that the first 4 picoseconds of perylene's in-plane and out of plane simulated depolarization (Figure 3.5) demonstrate little fast libration for the "out of plane" rotation (displacement of a vector normal to the aromatic plane) compared to the larger fast libration for the in-plane rotation. Since the anisotropy preexponential ("β") for out-of-plane motion is also 3-fold smaller, almost all of the "libration term" in r(t) seen via upconversion comes in-plane motion.

Figure 3.5. The first four picoseconds of the in-plane and out-of-plane simulated relaxation of perylene in hexadecane. The axis has been scaled to focus on earliest events. Note the relative lack of the quasi-ballistic behavior in the out of plane rotation compared to the in-plane rotation. Experiment (●, red), In-plane (■, blue), Out of plane (▲, black).

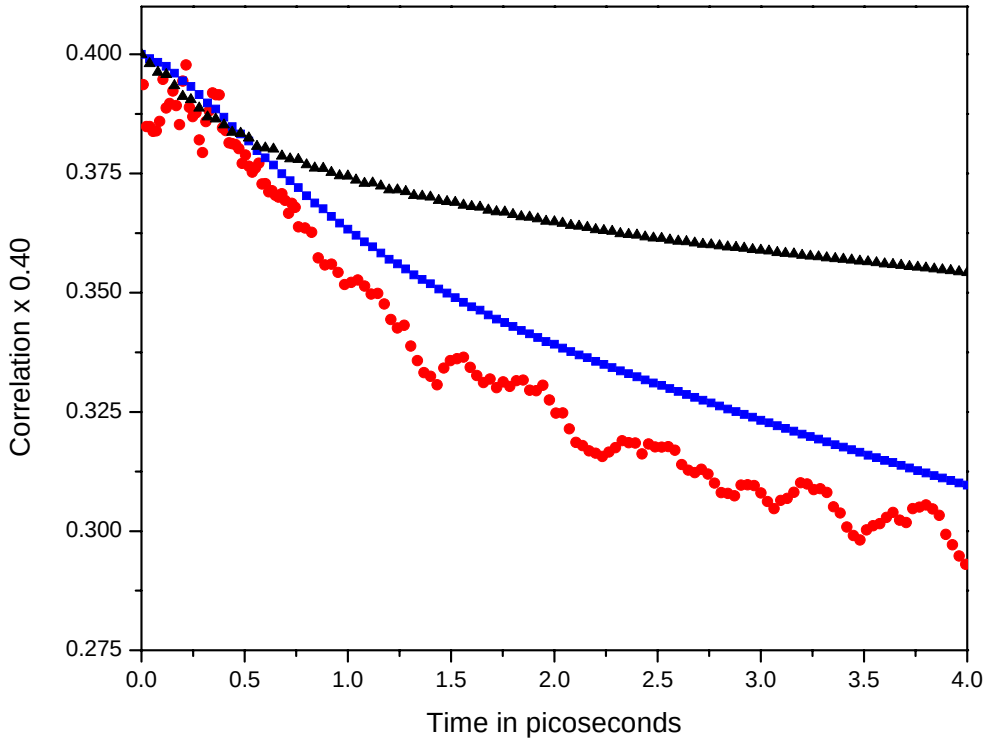

3.6. Conclusions

The molecular dynamics simulations agree well with perylene experimental results and provide insight into the existence of the fast "libration" term observed in upconversion data.

The in-plane libration of an ensemble of perylene, in hexadecane can be visualized as a 'wiggle' inside an average solvent pocket[129]. Perylene is able to rapidly 'slip' in-plane because there is no hydrogen bonding in hexadecane, and the average solvent pocket is undisturbed by small slips. The first 30 ps of the simulation match experimental data well and the longer decay terms in the experimental data are also mirrored. The correlation function obtained from the simulations for the out of plane motion of perylene contains less short term libration than seen for the in plane rotation, demonstrating that the libration seen in r(t) is predominantly an " in- plane" phenomenon. In contrast, for tetracene, the simulation only loosely follows the decay seen in experiments. The discrepancy could originate either in an apparent time offset (convolution artifact) or more likely in (previously reported)[150] vibrational coupling changes in this period.

Our quantum mechanical calculations of the excited states of perylene, however, affirmed that the observed behavior of perylene in hexadecane (and the recovery of the r_o defect) may be explained *using motion alone*. These quantum mechanical calculations show that neither the "twisted" nor the "butterfly" conformations of perylene should cause the r_o defect, because neither were accompanied by significant internal rotations of the transition moment that could account for loss of anisotropy. Prior studies that

suggested these possibilities brought up an important alternative[150], but a more computationally intensive examination disfavors this mechanism.

Recently, Pigliucci *et al.* [159] have performed fluorescence upconversion experiments on perylene derivatives whose D_{2h} symmetry was broken. Their (preliminary) report invoked vibrational cooling to account for the initial decrease in anisotropy. For perylene in a non-interacting solvent (toluene), they obtained a time constant of 2.4 ps, which is five times slower than our measured libration rate. In tetracene and other photophysical systems lacking the strong symmetric S_1 oscillator of perylene, vibrational cooling[150] may thus be an important consideration, but this effect was not apparent in the rise shape of "total" perylene decay curves ($I_{\parallel} + 2I_{\perp}$). Vibrational coupling clearly has influence on the anisotropy of some fluorophores, but it is not needed to explain our measurements of perylene motion in hexadecane. Any anisotropy decay curve calculated with libration should provide an upper envelope for experiments where both libration and cooling happen.

The fast librations seen here should be considered when analyzing, for example, orientation relaxation data obtained from tryptophans in proteins. A very fast libration was already observed in tryptophan analogs[160] that may still be operative in proteins and peptides since tryptophan, while constrained by backbone connections, can still have molecular reorientation dominated by the "pocket" around the indole ring. We have begun femtosecond anisotropy analyses in proteins[161-163] with these effects in mind.

Chapter 4: Dual-time scale photon timing methods

4.1. Introduction

As described in Chapter 2, Fluorescence Correlation Spectroscopy (FCS) has become a valuable tool to study many different softcondensed matter systems. The associated technique, Fluorescence Cross-Correlation Spectroscopy (FCCS) depends on the ability to simultaneously excite two fluorophores and then separate their contributions in a pair of detectors. An alternative way to separate the response of two fluorophores excited at the same time is by distinguishing excited state lifetimes of the fluorophores. The complexity of aligning a dual color system (no matter the excitation mechanism) and cleanly separating the emission of the overlapped fluorophores is partly relieved by using fluorescence lifetimes as markers. Since the fluorescence lifetime is generally much more sensitive to the environment than the Stokes shift, information about the fluorophore's local surroundings can also be extracted. Furthermore, identical particles labeled with a specific fluorophore can be used to probe different environments based on a multiexponential decay of fluorescence emission. For example, Benda[164] *et al.* separated the autocorrelation function of freely diffusing vesicles from mixtures containing free and substrate-absorbed vesicles. They measured the changes of the lifetime of a Bodipy labeled lipid due to quenching upon substrate absorption. Another study used the change in the lifetime of Cy5 arising from the coupling of labeled DNA to silver nanoparticles[165] to separate autocorrelation functions for free and bound species.

The most popular technique used for the detection of fluorescent lifetimes is called Time Correlated Single Photon Counting (TCSPC). The timescale measured in

this type of experiment can range from several picoseconds to nanoseconds. This technique measures emission relaxation times that, in the case of a polarized detector, can be directly related to correlation/rotational times. FCS and FCCS involve constructing a small privileged volume (by tight focusing of a laser beam) then recording of an autocorrelation function arising from fluctuations in intensity using a hardware or software correlator. The former method is implemented in commercially available electronics while the latter methods require only a file containing the photon counts over a period of time for postprocessing analysis. The timescale for FCS experiments is in the range of microsecond to seconds and appropriate for measuring translational diffusion. Most of the experiments performed using these techniques (TCSPC and FCS) involve distinct setups and equipment. Therefore, separate acquisition/measurement sessions are required to acquire data on the different timescales. Many studies have been performed in this 'separate' manner to study protein interactions. Recent advances in TCSPC hardware now allow recording photons over a time range of many seconds with picosecond resolution.[166-168] This technique makes use of an established data processing technique that, with today's computer power, can handle the large throughput required. Briefly, this is done by assigning to each photon detected two times ("time-tagging") with, 1) a macrotime, the time from the beginning of the experiment and 2) a microtime, the precise time since the previous laser pulse (few ps/bin number/channel). In this way, the information due to the microtime can be histogrammed to provide the decay profile from which lifetime(s) are extracted. The experiment time (or 'macrotime') can simultaneously be used to obtain a correlation function. For our first attempts in data analysis, we simplify the work done by Enderlein *et al.*[166,167,169], who make use of the known lifetime

components within the decays to create 'filters' for the total decay. These filters act as weights for all the channels in order to "unmix" and extract the ACF for a chosen lifetime. Recently variants of this technique, Fluorescence Lifetime Correlation Spectroscopy (FLCS) have been used to study fluorophore-labeled silver nanoparticle interactions[165], DNA compaction[170], distinguishing between dyes in a phospholipid migration in bilayers and vesicles[164] and the removal of background signals from single lifetime measurements.[167]

The time-tag recording (TTR) or First In First Out (FIFO) mode of the Becker and Hickl SPC cards and PicoQuant MicroTime series has been used to obtain a full correlation from picoseconds to seconds of simple dyes[168] and of peptides and a small cold shock protein.[171]

Unlike the above, more complex filtering approaches, we select regions of interest (ROI) with direct electronic masking (much faster than scalar multiplication with filter coefficients) to extract information about a specific lifetime. These ROIs are then multiplied by simple integral weights to calculate the separate correlation functions. These cards have also been applied to obtain Fluorescence Lifetime Imaging (FLIM) where decay curves are acquired over each pixel of an entire image.[172]

In this chapter, we describe our experimental setup and its testing on the lifetime and the diffusion coefficient of different fluorescent probes. We were able to measure the lifetime and diffusion of the Alexa 488 dye, the lifetime changes seen in the co-factor NADH fluorescence when binding the enzyme alcohol dehydrogenase (ADH) and the lifetime and diffusion changes of a DNA labeled with 6MI (a guanosine analog) as the DNA forms a quadruplex.

4.2. Materials and Methods

4.2.1. Instrument setup

4.2.1.1. Laser system

A Millennia X pumping a 'Tsunami' tunable Kerr lens modelocked Ti:Saphire laser (710-900nm) produced femtosecond pulses at a repetition rate of 80Mhz. The laser was 'pulse picked' to 4MHz using an AO deflector (Model 3980). The output was cleaned up using a spatial filter: The beam was focused into a 15μm pinhole using a f=13.8mm aspherical lens (6mm dia). After the pinhole, the beam was expanded and collimated using a f=75mm lens (25.4 mm dia.). The expanded beam was steered to an Axiovert 135M microscope (Zeiss). The IR was reflected into a 100x NA 1.3 oil immersion objective by a dichroic (dcrx640LP, Chroma Inc). The epi-fluorescence was collected and directed to the Alba II fluorescence spectrometer. A 50/50 beamsplitter was used to direct the light into two PMTs (H7422-40P, Hamamatsu). Identical pairs of filters, a 400LP and a 600SP (Thorlabs) were placed in front of the photo multiplier tubes (PMTs).

4.2.1.2. TCSPC setup

Our TCSPC setup uses the reversed 'start-stop' setup commonly used (Figure 4.1). A photodiode (PD10, Thorlabs) was used to synchronize the input signal to a SPC-630 PCI card (Becker and Hickl) providing the stop signal. The PMTs were powered by a DCC-100 PCI card connected to a Pentium 4 computer. The high voltage gain was set to

75% of the maximum. The DCC-100 card was also used to cool the PMTs through a secondary 12V connector to the Peltier controller of the PMTs. The maximum allowed current was set to 1.4A and the voltage was set to 2.6 V. The constant fraction discrimator (CFD) settings were: for the sync threshold, -100mV; the zero crossing level: as close as possible to the sync threshold (~-80mV) to avoid any spurious pulses from the original laser frequency second harmonics. The millivolt output pulses of the PMTs were amplified using 1.6GHz RF amplifiers HFAC-26 (26db, Becker & Hickl) that were connected to a router (HRT-80) in positions channel 0 and 1. A router passes sub-ns pulses to the CFD stages while it also resolves the detector number for the SPC-630 card in PC #2. All the acquisition settings for the SPC-630 can be accessed through software (SPCM v2.4). The settings for the stop CFD were usually as follows: -60mW for the CFD zero level and -80mV for the threshold. The TAC gain was set to 2, and the TAC range was 50 ns giving 9.77E-11 seconds per channel. The lower and upper levels were set to 5% and 95% of the whole TAC range. An ADC offset of 5% was also used. To improve the ADC linearity over the TAC range[168], the dither range was 1/8 of the total file. The FIFO frame length was 32-bits giving an ADC resolution of 256 channels. The delay in acquisition between the two PMTs was set to 10ns in the page control box. The Alba box and its components were controlled by PC #1 using the Vista software (ISS Inc, v7.4).

Figure 4.1. Description of the TCSPC setup (Reversed start-stop configuration). Am=Amplifier, BS=Beam splitter, DET=PMT detectors, DM=dichroic mirror, F=filter,L=lens, Obj=Objective in microscope, PD=photodiode, R=Router, SF=spatial filter

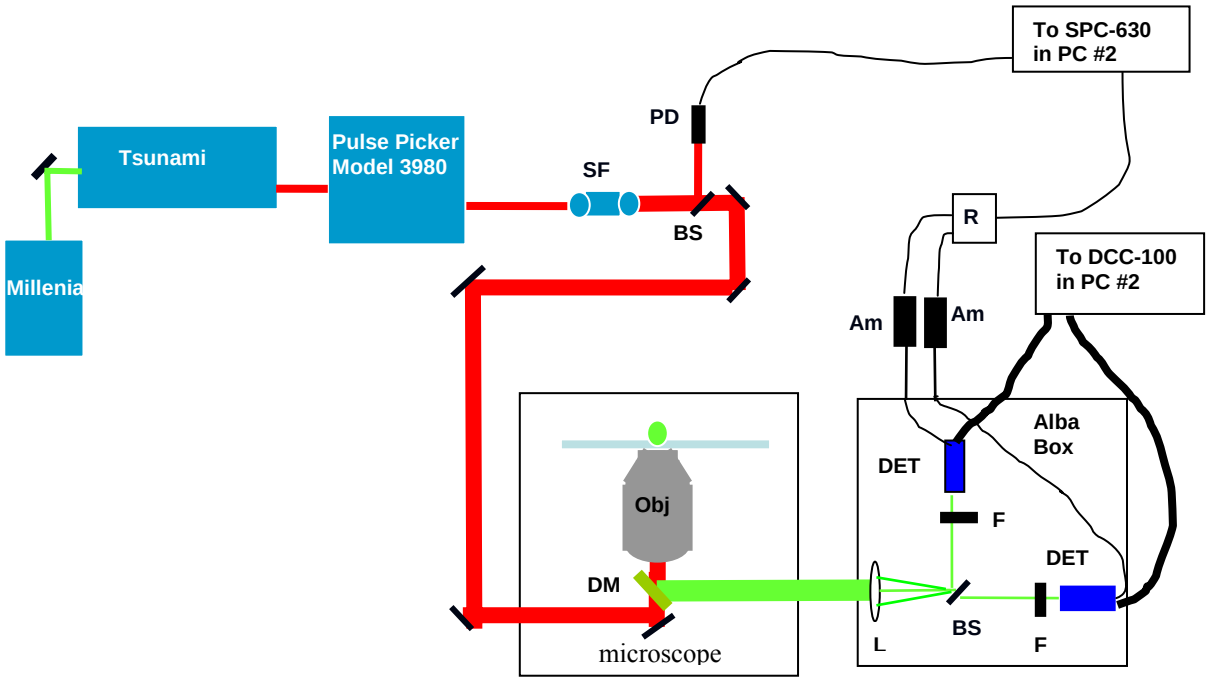

4.2.2. Data analysis

The data acquired from the SPC-630 card was saved to a computer for further analysis. The interface for the card controller allows for some fitting and rudimentary display of both the decay pattern and the auto correlation function. The autocorrelation function was done by the SPCM (v 2.4) software using a version with pseudologarithmically spaced lag times.[168] Most hardware *and* software correlators use the Schätzel[173] pseudologarithmically spaced lag times methodology. That is necessary

because a 'brute force' linear correlation over many seconds can be computationally time consuming. Since our ultimate goal was to use the decay curve as a means to select for a particular lifetime, the binary *.spc file was read using a Matlab script (see Appendix A). The script allowed access to the macrotime and microtime of each photon (files usually MBs in size). The processing of the files when using the Matlab script were done using the Biowulf cluster (http://www.biowulf.nih.gov) at the NIH. We implemented Schätzel's methodology in the Matlab scripts to calculate the correlation functions.

Initially, the files were exported as ASCII files to perform quick fitting of the decay parameters and the autocorrelation function. We only make use of the cross-correlation of both channels to avoid afterpulsing from the PMTs (at around 1-10μs timescale in the ACFs).

The number of peak counts for the instrument response function (IRF) and the sample were kept about ~25000 and ~13000 respectively. Usually, the files contained more counts than needed since longer acquisition times were required to improve S/N for the ACF than the decay curves. In these cases, the decay curves were 'trimmed' to contain the necessary peak counts. By this we mean that we avoided grouping so many counts that √N noise would fall below systematic noise. This precaution kept non-linear least square (NLLS) methods robust and valid. Alternatively, a global analysis over several subsets with $N \sim 10^4$could be employed. Instead, an in-house NLLS program, Decayfit (v 2.9.93), was used to fit the decay curves to a sum of multiple exponentials with the lifetimes and the pre-exponentials as variables:

$$I(t) = \sum_{i=1}^{N} \alpha_i e^{t/\tau_i} \qquad (4.1)$$

The IRF function is convolved with the acquired decay curve to perform a (NLLS) fit using the Levenberg-Marquadt algorithm. The recovered parameters were the lifetimes τ_i and pre-exponential factors α_i.

The autocorrelation function was fit using OriginLab software (v. 7.5) using a Levenberg-Marquadt algorithm to fit Eq. 4.2.

$$G_D(\tau) = \frac{\gamma}{\langle C \rangle V} \frac{1}{\left(1 + 8D\tau / w_o^2\right)\left(1 + 8D\tau / w_z^2\right)^{1/2}} \tag{4.2}$$

where C is the concentration, D is the translational diffusion time, w_o and z_o are the $1/e^2$ radial and axial waists of the focused laser beam.

We decided to do simple ROIs instead of a continuous filter like Enderlein has implemented. For example, we can remove from the correlation bins that can be considered only to belong to a particular lifetime. A simple +1 multiplier can be applied to those bins we wanted to keep and a "0" to those that we wanted to reject. Alternatively, ROI gate(s) in hardware could circumvent calculation. Using the Decayfit program, we simulated a decay curve with the IRF and the α/τ pairs from the lifetime(s) we wanted to exclude. We found the channel number at which the total integral intensity under the curve is one half. This channel divides the areas due to the lifetime(s) to be excluded exactly in two. The next step was to multiply by '+1' to the channels in the ROI before this particular channel and '-1' for the remaining channels. The last step was to correlate the whole time trace with those photons tagged with +1 and -1. The result was that the photons due to the lifetime to exclude with a '+1' would be 'canceled' by those photons with a '-1' giving only the ACF due to the remaining lifetime(s). This simpler

approach opens the door to fast hardware-based real time ACF presentation for lifetime-edited data.

4.2.3. Sample preparation

4.2.3.1. Samples for system characterization

TCSPC reconvolution analysis (to remove PMT jitter) requires knowledge of the PMT response to a delta-function input. To produce a good instrument response function (IRF) that could also account for the intrinsic PMT color shift (the variability of photon timing with photon energy), we used the dye DASPI (Exciton). This dye has a very short lifetime of ~35ps making it at least 10 times smaller than our measured experimental IRF width of 335ps (well within the boundaries for this type of PMT)[174]. A small amount of DASPI (Exciton Inc) was dissolved in EtOH and used without any other purification. "Nearly instantaneous" DASPI emission then occurs at the same energies as our unknown samples. Anthracene (Sigma) dissolved in 100% MetOH was used as a standard with a known lifetime of 4.0 ns.

A 2μM solution of Alexa 488 in H_2O was prepared and used to make daily series dilutions. These dilutions were used to calibrate the two photon excitation volume in FCS.

4.2.3.2. Alcohol Dehydrogenase

4.2.3.2.1. Expression and Purification

A plasmid that synthesizes the wild type Alcohol Liver Dehydrogenase protein was graciously provided by Dr. Bryce Plapp at the University of Iowa. The procedure to transfect and purify ADH from this plasmid has been described before.[175] Briefly, the plasmid was incubated with E.coli XL2-Blue competent cells (Stratagene). The cells were grown in 12.5 μg/ml tetracycline and 100μg/ml ampicillin agar plates. Single colonies were selected and used to seed culture flasks (1.5L) containing super broth medium that were shaken at 200rpm at 37 C. When the OD reached 0.8, induction of the protein was started by adding 0.3ml of 1M IPTG to a 1.5L flask. The cultures were allowed to grow overnight without shaking at 28 C by cracking open the incubator. The cells were harvested by spinning the cells at 6000rpm for 15 min and then washed with 5mM phosphate buffer, 0.25mM EDTA, pH 7.8 (NaP). The cells were resuspended in NaP buffer, lysed using a sonicator and 0.25mg/ml lysozyme. Protamine sulfate was added at 0.2% concentration and stirred for 30min at 4C. The solution was then centrifuged for 30min at 15000rpm. Twenty milliliters of the extract were put into a DEAE column and eluted with a 5mM sodium phosphate, 0.25mM EDTA, pH 7.8 buffer. The eluted fractions were checked for activity by absorption of NADH over time. The fractions with highest activity were pooled and loaded into a SP-Sepharose column equilibrated with 5mM sodium phosphate, 0.25mM EDTA pH 7. A 400ml gradient was run from 5mM-80mM sodium phosphate, 0.25mM EDTA, pH 7. The flow through was collected to check for activity and pooled. It was necessary (after concentrating) to load the pooled fraction on another DEAE column with 10mM Tris-HCL, pH 7.5 buffer. The

final concentration of the sample was 1mg/ml of pure ADH protein. This protein was compared to our stock sample of HLALDH (Boehringer-Mannheim) and was found to be as active. The LADH protein was stored at 4 C in a 10% ethanol solution with 10mM NaPO4, pH 7.0 and 0.25 mM EDTA. The buffer was exchanged to PBS for the experiments. Only about 100µl of solution are needed for each experiment.

4.2.3.2.2. Activity Assay for Alcohol Dehydrogenase

The following assay was part of the instructions for purification sent by Dr. Plapp.[176] Briefly a mixture mix composed of 19.62 g of $NaP_2O_7*10H_2O$, 0.429 g semicarbazide-HCl, 0.746 g glycine and 17.1 ml 95% ethanol was brought to a 500ml volume by adding distilled water (pH 9.0). 1.35g/ml of NAD^+ (Sigma) was added to the solution before the assay and allowed to equilibrate to room temperature. 10µL of solution containing enzyme was added to 990µL of this solution. The absorbance at 340nm was recorded for 10 minutes using a Perkin-Elmer Lambda 14 UV-VIS spectrometer. The temperature was maintained at 25 C. The specific activity is given by:

$$Units/ml = \frac{\Delta A_{340}/\min}{6.22\frac{\Delta A_{340}}{\mu mole}0.01ml} \qquad (4.3)$$

The specific activity of the horse liver enzyme was found to be 2.0 Units (U)/mg, this value compared well to the crystalline Boehringer-Mannheim enzyme activity of 2.4U/mg.

The samples used in these experiments were made by adding to a solution of ADH (1-0.1μM), the corresponding NADH concentration (factor of 2 or more) with excess isobutyramide (Sigma), 100mM.

4.2.3.3. 6MI labeled DNA

A stock solution of 3 μM 6MI (6-methylisoxanthopterin, Fidelity Systems), a guanosine based analog[177] (see Figure 4.2), was made by dissolving the appropriate amount of 6MI in a cacodylate buffer without salt. The sequence used was 5'-TA6GGTTAGGGTTTAGGGTTAGGG-3' with '6' showing the position of the 6MI. The labeled DNA was kindly provided by Dr. Lesley Davenport (synthesized by Fidelity Systems). The 6MI labeled DNA concentrations ranged from 100-200 nM dissolved in cacodylate buffer with and without 100mM KCl.

Figures 4.2. The chemical structure of 6MI with deoxyribose, a (deoxy)-guanosine based analog.

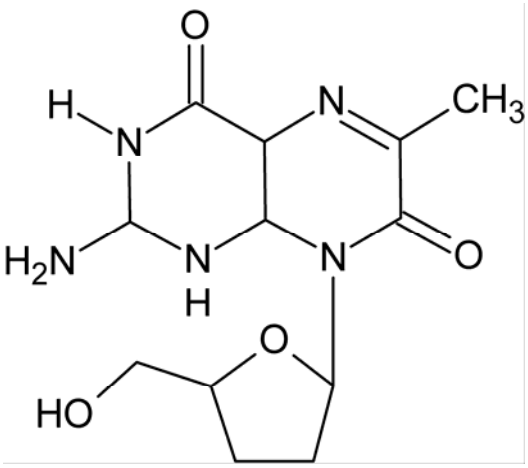

4.3. Results and Discussion

4.3.1. System Characterization

The concentrations and the known diffusion coefficient of Alexa 488 (300 μm^2/sec) were used to calibrate the excitation volume. The radial (w_o) and axial (z_o) $1/e^2$ dimensions were usually 0.25 and 1.7 μm respectively. The acquisition time varied between 30-120 secs. For Alexa 488, the amount of time required to collect 12000-15000 peak counts was ~15 secs for 1μM solution. The decay curve and the Alexa 488 ACF obtained for a solution of 100 nM are shown in Figure 4.3.

The lifetime in PBS pH 7.0 was found to be 4.00 ns (χ^2=0.92) comparing well to the 3.9 ns lifetime in the literature.[178] As explained in the methods (Data Analysis), the correlation function in Figure 4.3b was obtained from cross correlating the intensity traces of channel 1 and channel 2. The recovered diffusion coefficient was 293μm^2/sec and the concentration was 102 nM for a calibration of w_o=0.23 and z_o=1.75 μm. The data was sampled using the SPC-630's algorithm to create an autocorrelation function that is similar to the multi-tau methodology commonly used. Another advantage to using the SPC 630 card is that the smallest sampling rate becomes the total time required to record consecutive photons plus the dead time of the SPC-630 card (~150ns). We re-sampled a ~30 second data segment to 100 kHz by rebinning the data using the Matlab script, a sampling rate usually used in day to day experiments in FCS. By applying a simple windowing algorithm to the data, the S/N improved markedly. We selected a range of bin channels from 42-105 by applying a multiplier of 1 to those bins and a 0 to those photons outside that range. In effect, only using the photons closely associated with the 4 ns

decay. The sum of the square of the error (SSE) of the ACFs doubled from 0.0036 to 0.0078. The fit of the data to a 3D diffusion model improved very slightly to a χ^2 of 1.15 from 1.25 (Figure 4.4).

This improvement happened despite ~25% of the photons not being counted. In general, Alexa 488 is probably one of the brightest dyes with a substantial two photon cross-section. As a result this molecule served as an effective model solute for both lifetime and autocorrelation analysis at 710nm excitation.

Figure 4.3. Alexa 488 decay curve and ACF. A lifetime of 4.0 ns was recovered from the fit with χ^2=0.92. Fitting range was 50-231. The IRF (blue line) has been scaled to the maximum counts of the Alexa 488 decay. The bottom plot shows the standard deviation of the residuals to the fit. The top right hand corner has the autocorrelation of the fit showing no real pattern. B) The correlation function obtained from the cross correlation of both channels. The fit was done to Eq. 2. The recovered parameters were D=293 μm^2/sec and C=102 nM for w_o=0.23 and z_o=1.75 μm.

A)

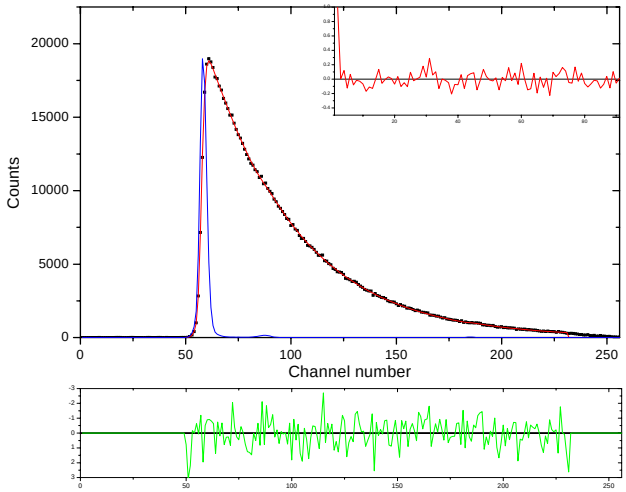

B)

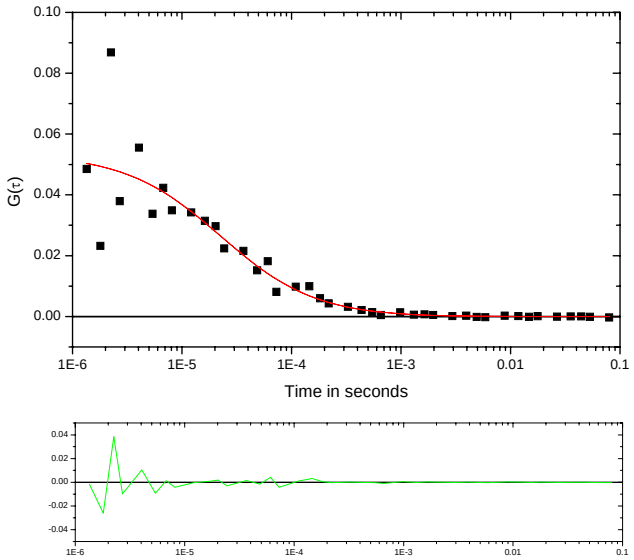

Figure 4.4. Correlation of 100nM Alexa 488 solution acquired for about 30 seconds. The correlation function was binned to 100 kHz. Both data sets were fit using D_t=300μm^2/sec and C=100nM. A) The uncorrected file returned w_o=0.40 and z_0=1.06 μm. B) After removing bins outside the range 42-105, the fit returned w_o=0.27 and z_0=1.15 μm . The χ^2 did not improve significantly (1.25 to 1.15).

A)

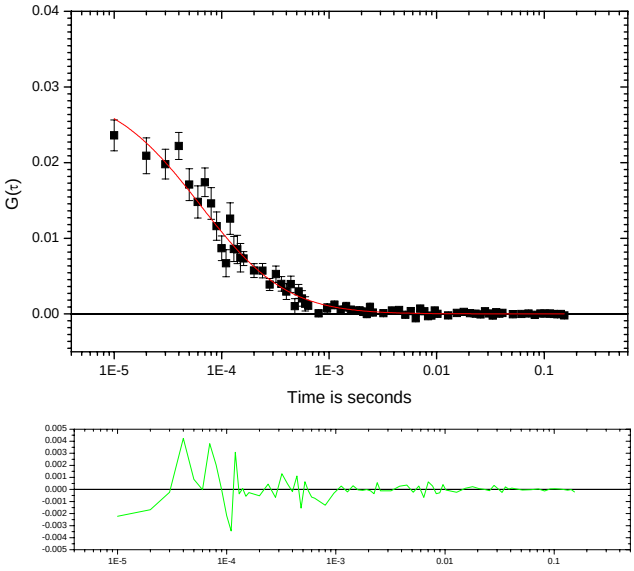

B)

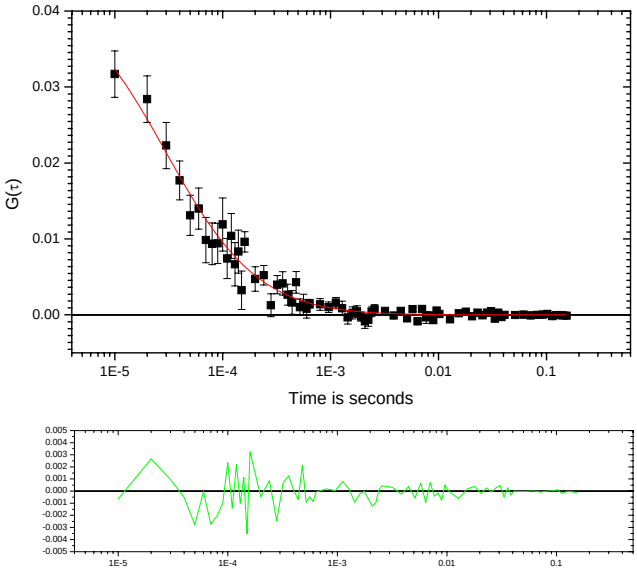

4.3.2. NADH and ADH results

NADH is a well studied and characterized fluorophore and a considerable amount of literature examines binding of NADH to ADH.[179-183] NADH has a very short lifetime when 'free' in solution. The cofactor NADH was chosen to test our systems because of its large change in lifetime when bound to various proteins, i.e. alcohol dehydrogenase (ADH). Upon binding to an eznyme (i.e. ADH), the lifetime increases by a factor of 10. We used the inhibitor isobutyramide (IBA) to form a ternary complex and hence prevent the dissociation of NADH from ADH. In solution unbound NADH has a measured lifetime of ~450ps (Figure 4.5, χ^2=1.28). The value of NADH can sometimes be split into two lifetimes of 0.358 and 0.620 ns with pre-exponentials of 1.17 (76%) and 0.377 (24%), respectively (χ^2=0.95). The intensity weighted mean of the two lifetimes was found to be $<\tau>$ = 452 ps and compared very well to literature.[181,184]

Many different ratios of [NADH] to [ADH] were tested. The ADH concentration was usually around 0.5-1μM while the NADH concentration was always submicromolar. As expected, the solutions contained different fractions of "free" NADH. The solution with about 30% free NADH in the presence of isobutyramide (IBA) is shown in Figure 4.6. The data were also smoothed twice using a three point adjacent average algorithm with Origin.

The recovered lifetimes were 0.49, 2.80 and 5.95 ns with α=0.41 (27%), 0.70 (45%) and 0.43 (28%), respectively. These lifetimes are in excellent agreement for the expected lifetimes for NADH-ADH-IBA complexes.[181,184] The time required to get enough counts to obtain an autocorrelation time was on the order of 0.5-1 hour. Figure 4.7 shows the results obtained for a sample with about 47% free NADH. In this case, the

lifetimes were 0.36, 2.34 and 5.71 with pre-exponentials 0.54(31%), 0.38(22%) and 0.83(47%) (χ^2=1.04). The data was also smoothed twice using a three point adjacent average algorithm with Origin Pro. There was a large scattering component that needed to be included in the fit. It was probably due to the positioning of the objective close to the bottom coverglass. We used the algorithm explained in the data analysis section above to remove photons linked to the longest lifetime (5.71 ns, Figure 4.7) and the shortest lifetime (0.36 ns). Since the experiments were performed at room temperature, the samples were made fresh each day and used only once. NADH has been found to have diffusion coefficients between 200-600 μm^2/sec in similar buffers.[185,186]

Figure 4.5. Decay of free NADH in solution obtained from 1μM sample in PBS. The intensity weighted lifetime was found to be 450ps (χ^2=0.95).

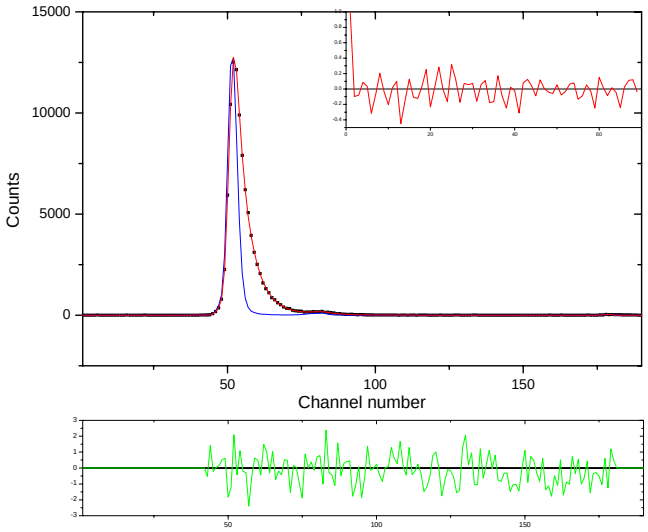

Figure 4.6. Decay and ACF of NADH-ADH-IBA complex with 30 % unbound NADH. The lifetimes recovered were 0.49, 2.80 and 5.95 ns with α=0.41, 0.70 and 0.43 respectively (χ^2 =1.04 fitting the 48-235 channel range). The IRF (blue line) has been scaled to the maximum counts of the ADH decay curve (0.097 ns/channel). The bottom plot shows the standard deviation of the residuals to the fit. The top right hand corner has the autocorrelation of the fit showing no real pattern. B) The autocorrelation function, G(τ), obtained for the best sample is shown (black). C) If we only choose those photons in the channel range 75-230, there is a slight improvement in the correlation curve. A 3 point adjacent average (2X) was applied to the data.

A)

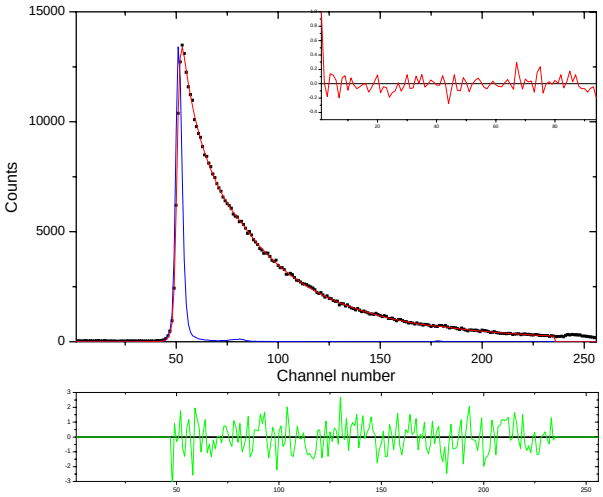

B)

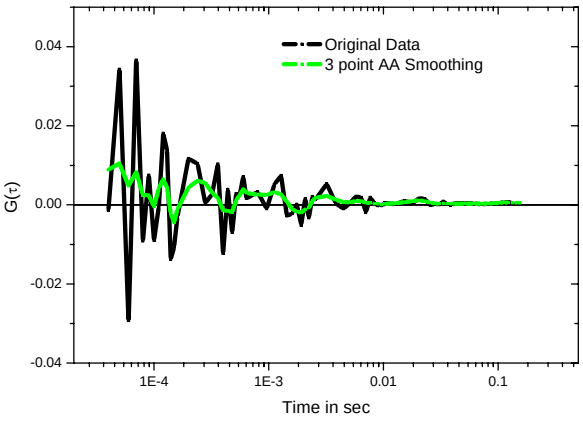

C)

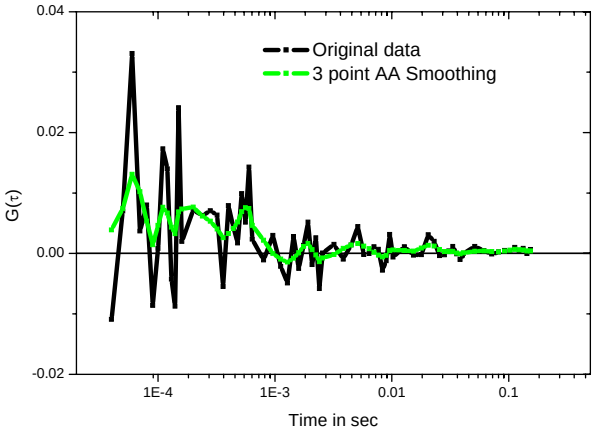

Figure 4.7. Decay and ACF of NADH-ADH-IBA complex with 47% unbound NADH. A) Decay curve of the complex. Fit was done from channel 43 to 233 (0.097 ns/channel). B) The original ACF, G(τ), decomposed by removal of shortest and longest lifetime. Removal of the shortest has a 'bump' at 1ms that could be NADH-ADH-IBA complex. The removal of the longest lifetime results in what appears NADH only diffusion. (Smoothing (2x) by a 3-point adjacent average is also shown)

A)

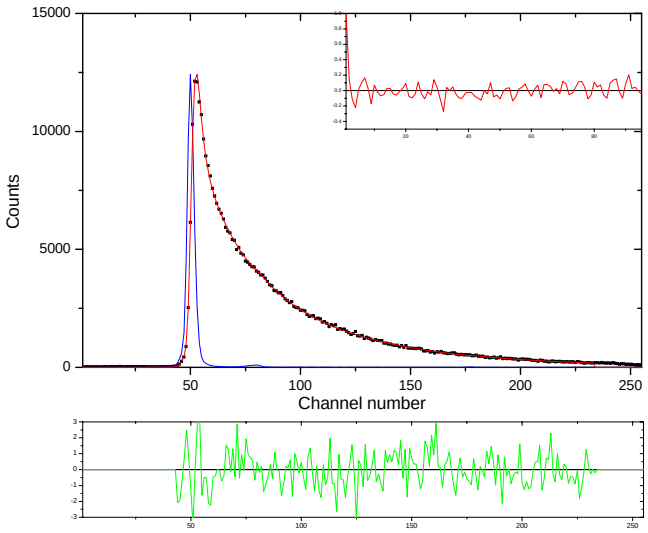

B)

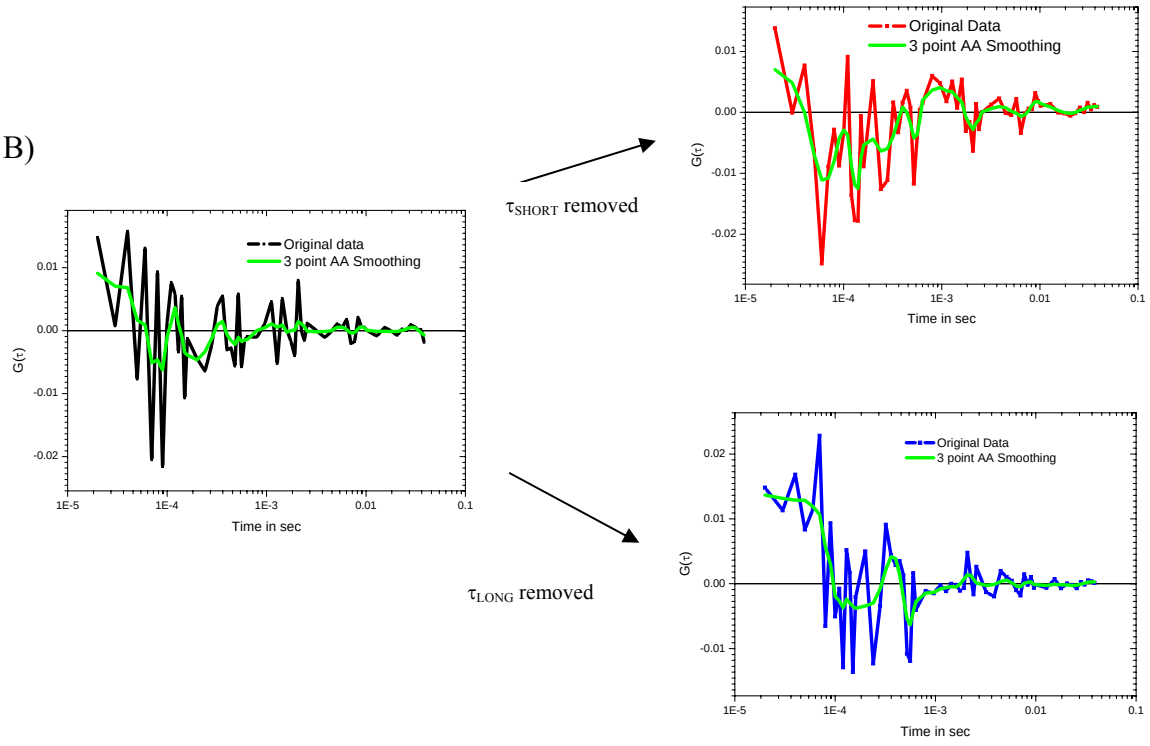

4.3.3. 6MI and G1 quadruplex results

6MI is a nucleoside analog that has been shown to change its lifetimes when surrounded by other nucleotides in a DNA single or double strand. 6MI has a complex decay in DNA due to quenching and moving of the 6MI in and out of the DNA stack. Interestingly, the decay profile is very specific to the identity of the local bases surrounding it. Our initial experiments found that lifetimes obtained for the 6MI nucleoside varied only slightly depending on the concentration. At a concentration of 1μM, there were two lifetimes: 2.4 and 6.37 ns with pre-exponential factors of 0.03 (3%) and 1.19 (97%) (χ^2=1.03). At a concentration around 250nM, the lifetimes were: 0.94 and 6.31 ns with pre-exponential factors: 0.04(3%) and 1.43 (97%) (χ^2=1.13). A lower concentration of 32nM produced three lifetimes of 0.35, 1.55 and 6.24 ns with pre-exponential factors: 0.69 (40%), 0.49 (30%) and 0.51(30%) (χ^2=1.18). Table #1 shows the results for all three concentrations. For the 250 nM concentration, we can separate the ACF into different components dependent on the lifetimes as shown in Figure 4.8.

Table 4.1. Lifetimes for three 6MI nucleoside concentrations. Typical errors are ~5%.

[μM]	α(%)	τ (ns)	α(%)	τ(ns)	α(%)	τ(ns)	χ^2	<τ> (ns)
1	3	2.4	97	6.37	-	-	1.03	6.33
0.25	3	0.94	97	6.31	-	-	1.13	6.29
0.03	40	0.35	30	1.55	30	6.24	1.18	5.06

Figure 4.9 shows the lifetime decay curve and the correlation function for the 32 nM 6MI nucleoside sample. The FCS fit returned a concentration between 40-70nM with a D_t= 660-1200 μm^2/sec (using a confidence level of 67%) with w_o= 0.23 and z_o=1.75 μm. A literature value for the diffusion coefficient of 6MI was found to be 560μm^2/sec (no uncertainties given).[187] The rather large difference between the literature value and ours is probably due both to the S/N of the curve and the fact that the "noise" is attributable to photophysics of the 6MI itself. The photophysics can arise from triplet state trapping that can produce correlations at 1-10μs. On the other hand, the 6MI labeled DNA diffusion coefficient obtained had better S/N. This last observation probably resulted from the diffusion time being outside the microsecond regime where photophysical events and the PMTs afterpulsing become a problem. G-quadruplex are guanosine rich DNA sequences that are known to form tertiary structures (cages) upon addition of salt. It is speculated that the cation interacts with the bases to form a stable structure. The data obtained for the 'G1' quadruplex is summarized in Table 2. We found that there is a change in the longer lifetime upon addition of salt accompanied by slight changes in the pre-exponential factors.

Table 4.2. Example for the lifetimes and pre-exponential factors for "G1" 6MI-DNA sample with and without salt.

	α(%)	τ (ns)	α(%)	τ(ns)	α(%)	τ(ns)	χ^2	<τ> (ns)
No salt (300nM)	46	0.41	25	2.44	29	6.35	1.15	5.02
With salt (170nM)	38	0.20	20	1.70	42	7.41	1.02	6.70

Figure 4.8. Decay and ACF of a 250nM 6MI solution. A) A 250nM 6MI concentration decay and B) decomposition of the ACF by removal of the long lifetime or the short lifetime.

A)

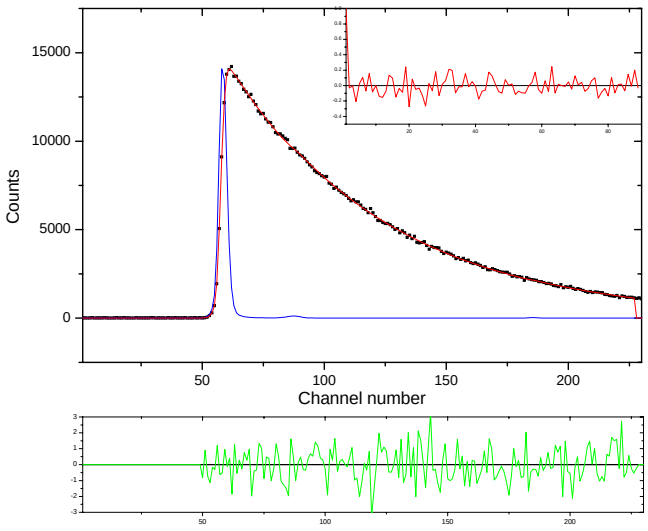

B)

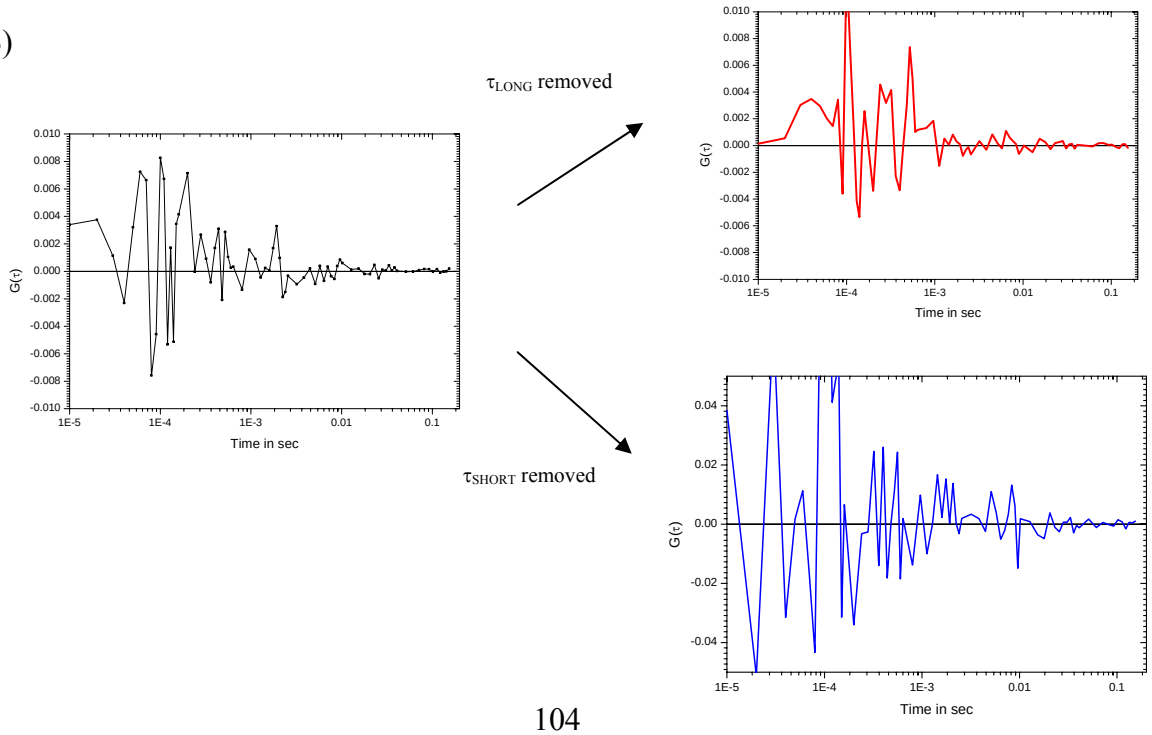

Figure 4.9. Decay and ACF of a 30nM 6MI solution. A) 6MI nucleoside lifetime and correlation (no salt). The lifetimes for the 31nM 6MI nucleoside were 0.35, 1.55 and 6.24 ns with preexponentials 40%, 30% and 30% respectively (χ^2= 1.18). B) Correlation function obtained from the ~30nM 6MI nucleoside from the Becker & Hickl card. The recovered concentration was 45nM and D_t= 660 μm^2/sec, but the fit is very poor (see text).

A)

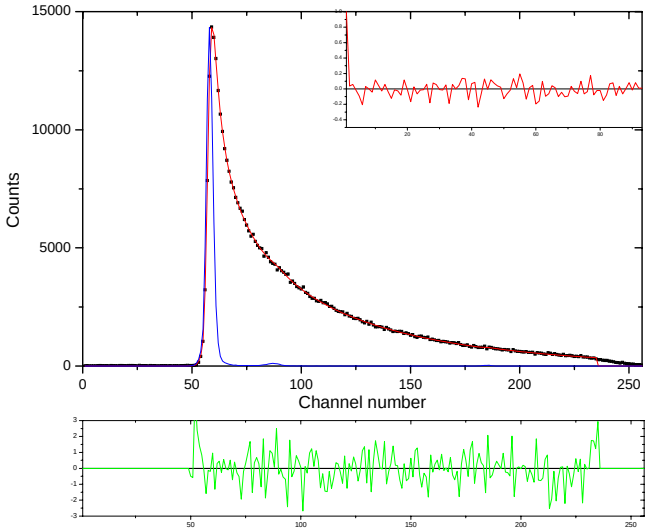

B)

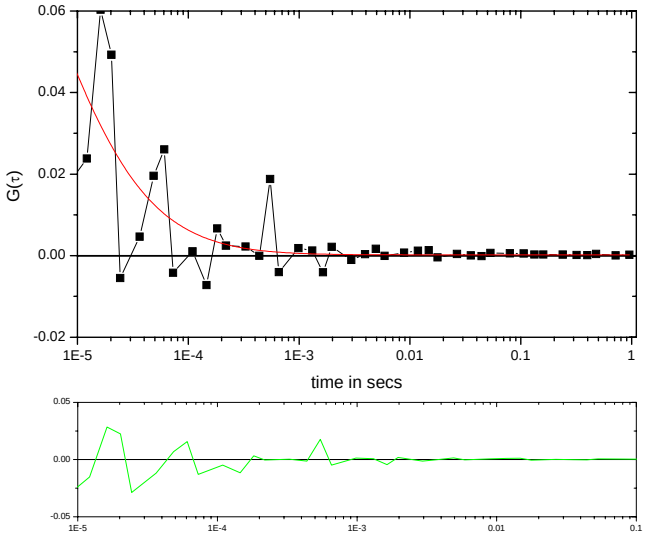

Following the same approach described in the data analysis section 4.2.1.3, we chose ROIs that would remove the signature lifetime of free 6MI nucleoside, ~6.3 ns. Figure 4.10a shows the 6MI labeled DNA data without salt. The S/N was quite low and removal of the long lifetime did not improve the ACF significantly. Figure 9b shows the results obtained for 6MI labeled DNA with salt. After applying a filter step function to exclude the long lifetime in this experiment, the ACF was now due to mostly the slower component of the original ACF. (The intensity integral completely cancels the long lifetime at channel 163).

The diffusion coefficient shifted slightly for the quadruplex from 90.7 to 77.4 μm^2 / sec (~10% error in D_t). This is an unexpected result since addition of salt typically leads to compaction of DNA. The diffusion of 90.7 μm^2/sec matches the hydrodynamic radius of about ~23.6 Å, slightly smaller than the width of the β-barrel of eGFP protein. For comparison, Bolten *et al.*[188] used dynamic light scattering to measure a duplex 16-mer sequence capable of making a quadruplex. Using this technique the quadruplex had a D_t= 114 μm^2/sec at 20 C. Whether a more rigid "cage" is formed by the addition of salt resulting in a larger hydrodynamic radius is not known. In fact, the quadruplex without salt should behave as a ssDNA, perhaps with random coil qualities. The use of another fluorophore instead of the 6MI that still allows formation of a quadruplex and the disruption of the quadruplex structure by complementary DNA segments would help to clarify these questions.

Figure 4.10. ACF of 6MI labeled 'G1' quadruplex samples. A) No salt. The S/N is probably reduced due to μs 6MI photophysics. B) With salt. There is much better S/N and removal of the longest lifetime allowed us to select the slowermoving component.

A)

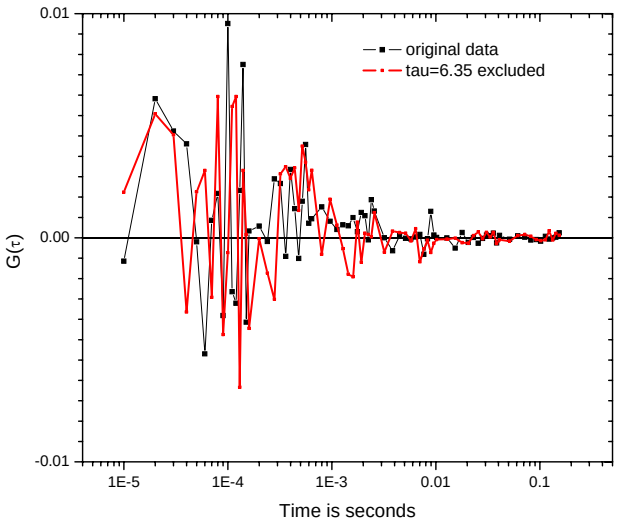

B)

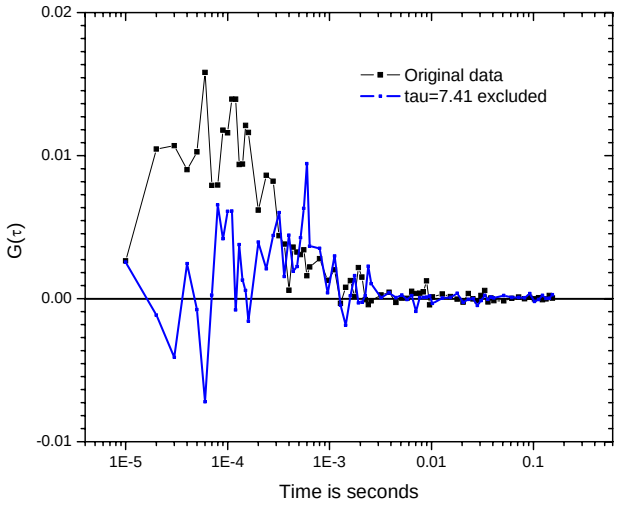

4.4. Concluding remarks

We have demonstrated our ability to measure simultaneously the lifetime and the translational rate of model fluorophores like Alexa 488 in a single experiment. More importantly, we have shown that complexity of the ACFs can be improved by extracting translational data from only those lifetimes that contribute to a selected translational form. Because our assembly had only 256 channels, some of these shorter lifetimes could not be separated very well. An added advantage from combining these techniques was the reduced amount of sample used (100 μl volumes are routinely used at less than 1 μM). Future plans involve implementing the algorithm of Enderlein *et al.* to filter the components from each lifetime. This is in the works and should help in separating some of the shorter lifetime species that could have little contribution to the translational diffusion coefficient.

Acquiring simultaneous time resolved anisotropy and the diffusion coefficient of a protein undergoing conformational changes –and their linkage- will be the goal. It might even be possible to extract diffusion tensor information (and D_t and D_r tensor couplings) from these types of measurements, since rotational correlation information will be available from the correlation times. Anisotropy measurements should be straightforward with our current setup. We still have yet to decide if having a polarizer in front of each channel is sufficient in order to measure the vertical and horizontal components simultaneously or whether the use of both PMTs to obtain the cross-correlation function in each polarizer will be necessary. As we have shown in these test cases, the photophysics of the fluorophore will be an important and deciding factor. We

expect this technique (after modeling) will be very useful in the detection of conformational changes upon protein binding.

Chapter 5: Multi-photon Imaging Techniques: Coherent Anti-Stokes Raman Spectroscopy (CARS) microscopy and Stimulated Emission Depletion (STED)

5.1. Introduction

Even though the theory of multi-photon excitation was developed in the 1930s, the technical challenges limiting this process from being used as an analytical tool have only been overcome in the last few decades. Developments in ultrafast laser technology in the late 1980s led to commercially available systems with peak intensities necessary for driving multi-photon phenomena. One of the crucial demonstrations of the capabilities of multi-photon microscopy was realized by Denk[25] *et al.* in 1990 using two-photon absorption of various fluorophores *in vivo*. Within a decade, many multi-photon techniques had become common in physics, chemistry and biology including Second Harmonic Generation (SHG)[189,190], Third Harmonic Generation (THG)[191,192], Coherent Anti-Stokes Raman Spectroscopy (CARS)[39] and Stimulated Emission Depletion (STED).[46] The first two techniques produce signals that are non-specific and very large powers are required to obtain good signal to noise ratios. We have concentrated on CARS because of the high chemical specificity and sensitivity compared to SHG and THG. We have also used STED, a technique that exploits the saturable transition kinetics of fluorophores to achieve superresolved imaging.

5.1.1. CARS microscopy

CARS microscopy is a type of coherent vibrational microscopy that is intrinsically chemically selective, due to the specificity inherent in a molecule's vibrational frequencies. In comparison to IR microscopy, CARS is not limited by inherent problems arising from low sensitivity, high laser powers and water absorption at the large wavelengths. The use of ordinary Raman microscopy improves on the water absorption problem, but the inelastic nature of the process limits the number of detectable events[193]. As a result, Raman experiments still require long acquisition times, prohibiting the use of spontaneous Raman spectroscopy for the imaging of live systems. CARS microscopy[39] can partly overcome the small cross section problem of Raman scattering microscopy; the conversion efficiency is higher since the coherent CARS signals scale as the square of the number of oscillators present while a spontaneous Raman scattering process is linear.

CARS microscopy probes a particular vibrational mode in a molecule. The emitted light (whose energy is the sum of the pump photon and one vibrational quantum) is shifted to a higher frequency (anti-Stokes) than both laser beams used to excite the molecule (Figure 5.1). (The process is dependent on concentration of oscillators present, so there are practical limits on measured concentration). At the moment, the current limit of sensitivity stands at about 100μM. Little or no photo-damage of the sample occurs because of the relatively low powers used, the low energy of each photon (red and near-IR, where few biomolecules absorb) and the low peak energy of the pulses (which are ps in duration, to keep bandwidth narrow). Most important, one can observe specific bond vibrations of cells *in vivo* without the need to label the target molecule.

Figure 5.1. The CARS process involves three steps: 1) Population of the vibrational state, 2) excitation of the vibrational state to a virtual state and 3) the emission of the Anti-Stokes photon. (Adapted from Ref. 51)

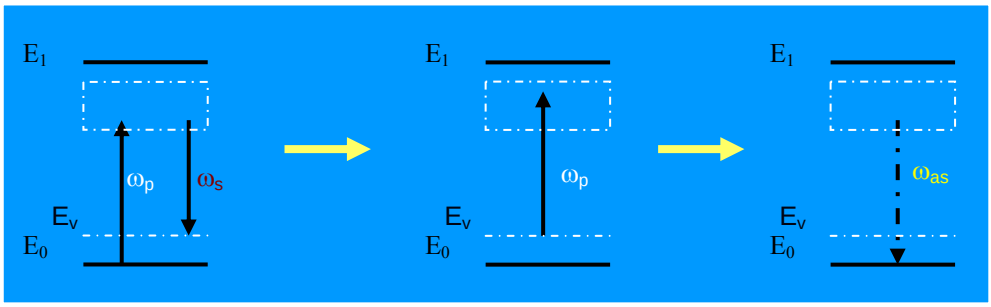

1. Need to populate the vibrational state first: Vibration at $\omega_v = \omega_p - \omega_s$

i.e. CH stretch

2. Excite the vibrational state E_v with ω_p

3. Anti-Stokes signal from the excited vibrational state of a molecule at $\omega_v = 2\omega_p - \omega_s$

CARS is a four wave mixing process where a pump field E_p, a probe field $E_{p'}$ and a Stokes field E_s interact with a sample to generate a fourth wave. To simplify, CARS can be thought of as a pump beam and a Stokes beam interacting with a sample via a wave mixing process. In this three-photon excitation process, we excite and scatter from a particular vibrational mode of the molecule under study, leading to chemical specificity. This three-photon process results in high spatial resolution that can be comparable to (if not better than) two photon excitation.[39] When the beat frequencies of these fields (ω_p-ω_s) match a Raman active mode of a molecular vibration, the oscillators are coherently driven by the excitation fields, producing blue shifted (anti-Stokes) signal at a frequency

$\omega_{AS}=\omega_p-\omega_s+\omega_{p'}$. When the pump and the probe beam are the same as in our case, the CARS signal is produced at $\omega_{AS}=2\omega_p-\omega_s$. This situation is only realized when the two laser beams are precisely overlapped in space and in time and steered into a microscope with a high numerical aperture (N.A.) objective, capable of tightly focusing the laser beams to produce a high intensity distribution. The beams are then raster scanned through the sample using a piezo stage or with scanning mirrors to produce an image. A CARS signal can be detected in two ways: 1) Forward CARS (F-CARS) uses a condenser to collect the emitted light, 2) Epi-CARS (E-CARS) collects the light directed back into the objective. For the signal to constructively interfere, the propagating waves must fulfill phase matching conditions (explained further in the following theory section). We have performed E-CARS experiments in this study. The E-CARS signal drops dramatically compared to F-CARS when the size of the object being imaged is about twice the pump beam wavelength (Figure 5.2), but epi-CARS also has a low background.[194,195] The de-phasing process diminishes the signal approximately by a factor of 10 in a few microns (when compared to F-CARS). While the background in F-CARS is considerably higher, forward detection sets no limit to the size of the scattering object.

Figure 5.2. Size dependence and background of Forward and Epi-CARS. A) Size dependence. D is the diameter of a sphere. The pump and Stokes wavelengths are at λ_p=800 nm and λ_S=917 nm. B) Background dependence. F-CARS is shown on left and E-CARS on the right. A polystyrene bead with a 535nm diameter was used. (Taken from Ref. 195).

A)

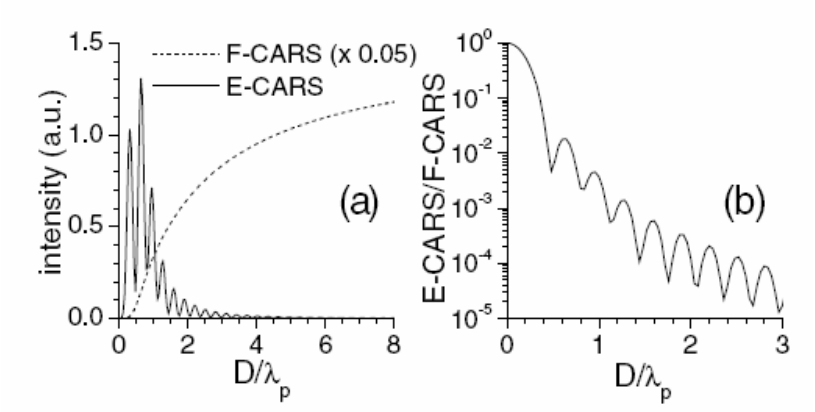

B)

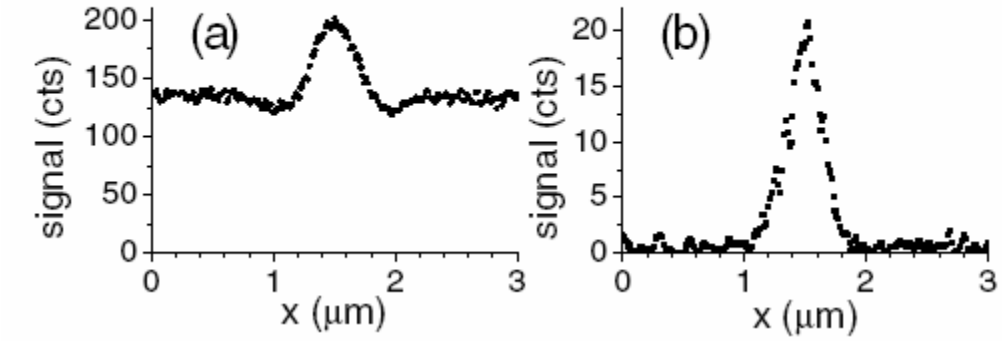

Disadvantages of CARS arise from the non-resonant background (and possible two-photon enhanced non-resonant background). New techniques to suppress the non-resonant background have been developed in the last ten years. They involve backward detection of the signal (epi-detection, E-CARS)[195,196], frequency modulating[197] the light sources to filter out any nonresonant component from the solvent (FM-CARS), polarization (P-CARS)[198] of the laser beams so that only the resonant signal can survive, and the time gating[199] of the CARS signal to gate away any other emitted photons, i.e. fluorescence, using TCSPC techniques. Our initial approach was necessarily focused on backward detection CARS (E-CARS) in order to substantially decrease the non-resonant background from the solvent, although at a cost of decreased signal.

5.1.2. Stimulated Emission Depletion

The diffraction limit established by Abbe[200] sets the bound for the resolution limit of a scanning microscope:

$$\Delta r = \frac{\lambda}{2NA} \tag{5.1}$$

where Δr is the distance between two objects that can be distinguished, λ is the wavelength of the light and NA is the numerical aperture of the objective ($NA = n\sin\alpha$, n is the refractive index of the solution and α is the aperture angle of the lens). This quantity is called the diffraction limit because two objects cannot be distinguished if they are closer than Δr.

In microscopy, this limit has been the physical barrier imposed by the optics of the system on the ability to distinguish small objects in solution. The same limit applies to confocal microscopy. This limit applies because light diffracts when squeezed through a small aperture as in a confocal microscope conjugate pinhole. For an ideal circular aperture, the diffraction pattern on the plane at the focal point is called an Airy disk (after George Airy). The image of an infinitely small luminous point source is a circular Airy diffraction image as shown in Figure 5.3. The theoretical maximum resolution for an optical system is equal to the diameter of the first dark circle. If two Airy disks are closer than half their widths, they are no longer resolvable (called the Rayleigh criterion). For diffraction at a circular aperture (Fraunhoffer), the intensity[201] is given by:

$$I(r) = \left[\frac{2J_1(r)}{r}\right]^2 \tag{5.2}$$

where I is the intensity, r is a vector and J_1 is the Bessel function of the first kind. The diffraction limit for such an aperture is now:

$$r = \frac{1.22\lambda}{2NA} \tag{5.3}$$

Figure 5.3. Plots of the Airy disk function. A) Airy disk function along x-axis and a close-up of the second and third maxima. B) Airy disk in 3D. C) Two resolvable Airy disks. D) Two unresolvable Airy disks.

A)

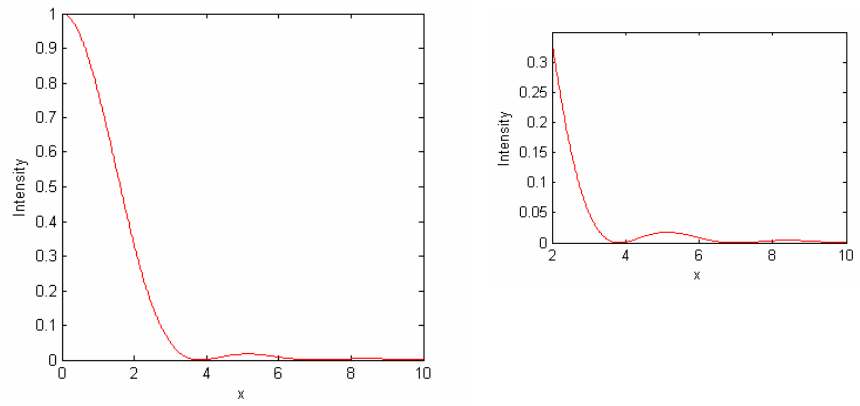

B)

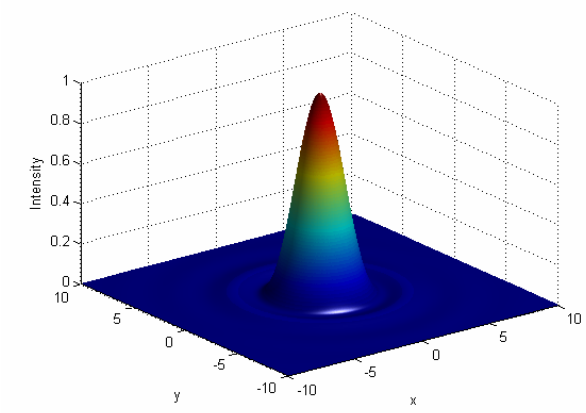

C)

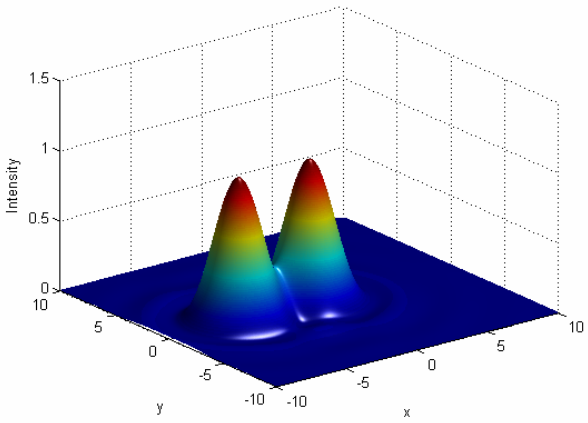

D)

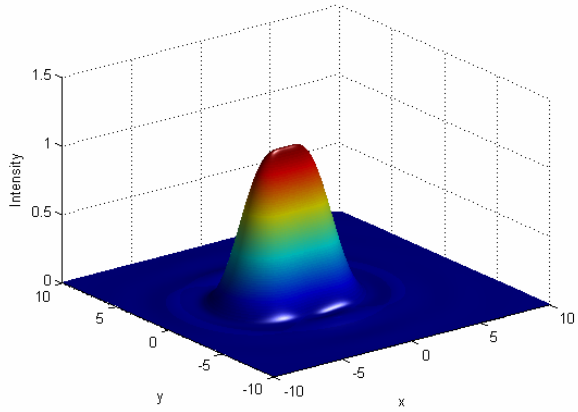

Recent methods have been developed that try to improve on the point spread function (PSF) by changing optical components. 4Pi microscopy[202] uses two opposing, coherently summed objectives to make the PSF more spherical, thereby improving resolution. Other obvious strategies for improving spatial resolution include using shorter wavelengths, but this approach runs into technical difficulties such as the need for UV objectives and mirrors that can manipulate the shorter wavelengths without great loss of signal. Also, the development of electron microscopy (EM) gets around this limit by avoiding the use of light altogether. Unfortunately, vacuum requirements for EM make this technique unsuitable for using live samples., although whole cells have been TEM scanned within microfluidic devices.[203]

In STED[204,205] the ability to improve spatial resolution depends only on the ability of light to coherently deactivate an excited fluorophore. STED microscopy works by first exciting a fluorophore using a laser and objective with a diffraction limited spot. Then, before the fluorophore emits, a second beam tuned to the redder wavelengths of the fluorophore's emission is used to quench those molecules outside of the center focus via stimulated emission. If the STED beam is shaped like a ring or donut, then fluorescence is observed only from those molecules that were not depleted in the now sub-diffraction center (See Figure 5.4). The power required from the STED laser beam (50~100mW) is comparable to power levels used in two photon excitation microscopy resulting in application to many fluorescent probes, including fluorescent proteins.[206] Recently, applications of this superresolution technique have started to become more widespread, including some applications to live systems[206]. Because fluorescent probes are used for STED, many of the techniques applied to normal confocal microscopy are now being

used for STED, i.e. image deconvolution [50] and new probes[207] designed for *in vivo* cell imaging. Recent developments include using dual color STED to study protein co-localization in neurons[48,208,209].

Figure 5.4. The STED process. A) Jablonski diagram for STED. The STED beam causes stimulated emission taking down the excited molecules back to the ground state. B) STED beam is in the emission spectrum of the selected dye. The result is quenching of the fluorescence. C) A bead labeled with a dye is excited with a laser in a typical confocal manner. A second beam (5 ps *behind*) with a wavelength at the red edge of the dye's emission in the shape of a 'donut' depletes the region by stimulated emission. The excited molecules in the donut ring are taken back to the ground state. Now the remaining dye molecules at the center fluoresce normally creating a spot smaller than a diffraction limited spot. Shown are three different donut quenching probabilities, left side in green: intensity of fluorescence of a bead created by the excitation laser, in red: the STED beam in the shape of a donut depletes the outer rim. Result of applying STED beam on the right: the resulting spot for three power levels from low to high with increasing probability of stimulated emission depletion.

A)

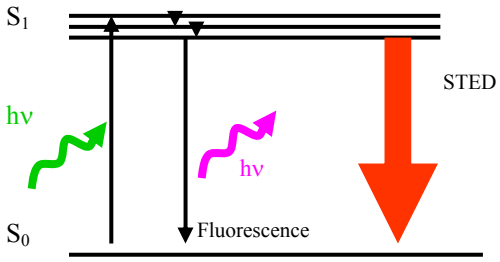

B)

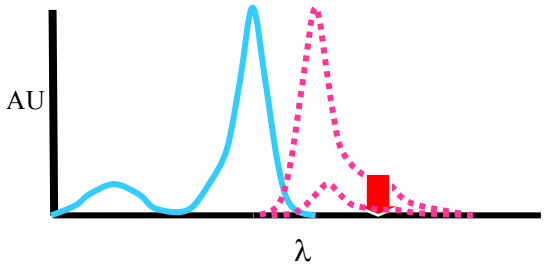

C)

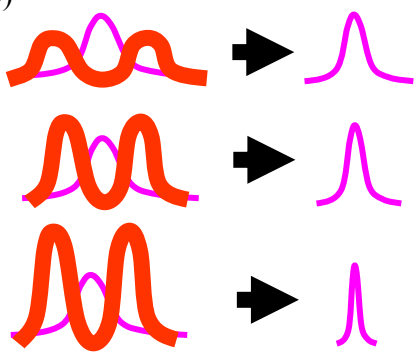

Another use of the reduced volume created by STED includes performing FCS[49] on the non-depleted region. The advantage of STED over conventional FCS is the reduced excitation volume. With fewer molecules in the excitation volume, the changes in intensity (fluctuations) are larger producing a better S/N than two-photon or single photon FCS. Using STED, Hell *et al.* have been able to distinguish between hindered and free diffusion of Atto647N labeled lipid in live cells.

5.1.3. Scope and goals of CARS and STED experiments

Using CARS microscopy we have targeted the eventual measurement of concentration of NAD^+ molecules in living cells. NAD^+ is the oxidized form of NADH and both are two of the most important molecules in mitochondria. These molecules are important intermediates in the production of ATP. NAD^+ is converted into NADH by capturing energy and one electron (per NADH) released in the Citric acid (Krebs) cycle.[210] NADH "gives up" the stored energy to the final acceptor (molecular oxygen) in the process of oxidative phosphorylation. At this point NADH becomes NAD^+, returning to the Krebs cycle to receive electrons at different points of the Citric acid cycle. Both NADH and NAD^+ are constantly being interconverted, but the total nicotinamide pool remains nearly constant. NADH is a naturally fluorescent molecule that has been quantified by our group in different bound or free states[211]. The redox balance of cells and organelles is of great biological interest; in particular, the relative concentrations of reduced and oxidized nicotinamide in mitochondria are of great value. Our motivation for using CARS microscopy is to quantify the *nonfluorescent* [NAD^+] in mitochondria and

establish enzyme kinetics of NAD^+ and NADH. These values may be useful to analyze muscle energy consumption and overall health, especially heart muscle. To quantify the non-fluorescent NAD^+, we have built a Coherent Anti-Stokes Raman Spectroscopy microscope. We use it to excite the ring breathing mode of the nicotinamide moiety of NAD^+ near 1032 cm^{-1}, resulting in anti-Stokes emission at 675nm. For possible simultaneous monitoring, one of the two different input laser pulses (near 730nm) concurrently (weakly) excites two photon fluorescence of NADH (but not NAD^+). The NADH and NAD^+ signals can be separated; thus we can monitor simultaneously the concentration of both species in the cycle. To simulate mitochondria, we prepared DPPC LUVs (large unilamellar vesicles) loaded with millimolar levels of NAD^+ and/or NADH. The NAD^+ vesicles yielded signals for CARS only (two photon NADH emission was absent).

We have also used our instrument to visualize water in vesicles and live Hela cells using as a diagnostic the O-H stretch at 3340 cm^{-1}. The resulting anti-Stokes signal appears at 510nm. In live cells, a quick switch of the surrounding media to D_2O produces a rapid (<1 min) extinguishing of the cell interior water signal. Since the O-D stretch is centered at 2800 cm^{-1}, that vibrational mode is not significantly excited at a frequency difference[212] of ~3300 cm^{-1}.

The CARS system has two laser pulsed beams with one in the NIR (~770nm) and another in the visible range. These two beams are spatially and temporally overlapped. Also, the timing between the pulses can be tightly controlled because of a delay stage in the path of the visible beam. This setup with very small changes lends itself to other multiphoton techniques. As part of the development of novel imaging techniques, we

modified our CARS setup to overcome the diffraction limit using Stimulated Emission Depletion (STED).

Our first images using STED microscopy show that we can image objects beyond the diffraction barrier, to a resolution of about ~100nm. This instrument also enabled us to test a novel photochromic dye-Our STED microscope employs a 'vortex phase plate' capable of creating a center hole in the beam profile as seen in Figure 5.5. We present the characterization of the STED microscope using fluorescent beads proving that our system is capable of breaking the diffraction limit. We also include some preliminary data on the photochromic switching of the novel dye.

5.2. Theory

5.2.1. CARS

5.2.1.1. Polarization and Intensity

We would like at this point to dwell a little on the mathematical implications of superposing different optical electric fields (with different wavelengths) on matter. We will explain the dependence of the CARS signal intensity on the electric field and the susceptibility. We also show how the anharmonic oscillator concept is used to obtain a formula for the susceptibility and its dependence on the resonant and nonresonant frequencies. Lastly, we comment on the necessary phase matching conditions of the different electric fields necessary to produce a CARS signal. We explain these using the derivations of Xie *et al.*[14]

The polarization (induced dipole per unit volume) of a medium subjected to an electric field can be expressed as a power series[37]:

$$\vec{P}(\omega) = \chi^{(1)}(\omega)\vec{E}(\omega) + \chi^{(2)}(\omega)\vec{E}^2(\omega) + \chi^{(3)}(\omega)\vec{E}^3(\omega) \quad (5.4)$$

where P is the macroscopic polarization vector, χ is the dielectric susceptibility tensor with rank n +1, n is the order of the susceptibility and E is the applied electric field at a frequency ω. $\chi^{(1)}$ is the linear susceptibility related to classical, linear optics including spontaneous Raman scattering. As the field strength increases, χ^2 and χ^3 begin to play a larger role in a molecule's response to incident light. The first non-linear term is responsible for second harmonic generation, sum and difference frequency generation and parametric oscillation.[37] The second non-linear term is responsible for third harmonic generation ($3w_1 \rightarrow w_3$) and other processes like CARS. $\chi^{(2)}$ equals zero in isotropic media and the first nonzero nonlinear term is $\chi^{(3)}$.

Assuming the same direction of propagation of the electric fields used in Eq. 5.4, we can say that[213]:

$$E_i(\omega_i) = \frac{1}{2}\left[A_i e^{i(k_i z - \omega_i t)}\right] + c.c. \quad (5.5)$$

where $\omega_i = 2\pi c/\lambda_I$, A_i is the amplitude, k_i is the momentum vector equal to $\omega_i n_i/c$, t is time, z is the distance along the direction of propagation, n_i is the index of refraction at ω_I and c.c. is the complex conjugate.

We can rewrite Eq. 5.4:

$$\vec{P}(\omega) = \frac{1}{8}\left[3\chi^{(3)}(-\omega_3, \omega_1, \omega_1, -\omega_2)\left\{A_1 A_2^{*2} e^{i(2k_1 - k_2)z - (2\omega_1 - \omega_2)t} + c.c.\right\}\right] \quad (5.6)$$

where $\chi^{(3)}(-\omega_a, \omega_b, \omega_c, \omega_d)$ represents the susceptibility for the process, $\omega_a=\omega_b+\omega_c+\omega_d$.

With the input beams at $\omega_1=\omega_p$ and $\omega_2=\omega_s$ (p for pump/probe and s for Stokes), the output field E_{as} is governed by the wave equation[213]:

$$\left[\nabla^2 + \frac{\omega_{as}^2}{c^2}\varepsilon_{as}\right]\vec{E}_{as} = \frac{-4\pi\omega_{as}}{c^2}\vec{P}^{(3)}(\omega_{as}) \tag{5.7}$$

with the solution:

$$\vec{E}_a = \frac{-i\pi\omega_{as}}{2c\varepsilon}\left|\chi_{as}^{(3)}\right\|E_p\Big|^2 E_s^{*} l \frac{\sin\left(\Delta kl/2\right)}{\left(\frac{1}{2}\Delta kl\right)} e^{-i\Delta kl/2} \tag{5.8}$$

where l is the interaction length, $\Delta k=k_a-2k_p+k_s$ is the wave vector mismatch (i.e. matching condition) between the CARS field and the incident fields, k_a is the anti-Stokes, k_p is the pump/probe and k_s is the Stokes vectors respectively and E_p and E_s are the electric fields of the probe/pump and Stokes beams. The intensity of the detected signal is then given by[213]:

$$I_a = \frac{c}{2\pi}\left|E_a\right|^2 = \frac{2\pi\omega_{as}^2}{c\varepsilon}\left|\chi_{as}^{(3)}\right|^2\left|E_p\right|^4\left|E_S\right|^2 l^2 \frac{\sin^2\left(\frac{\Delta kl}{2}\right)}{\left(\frac{\Delta kl}{2}\right)^2} \tag{5.9}$$

As can be seen in Eq. 5.9, the intensity is dependent on the square of the susceptibility and has a non-linear dependence on the incident electric fields. There is also a complex dependence on the l that we will later discuss in Section 5.2.1.3.

5.2.1.2. Anharmonic oscillator, polarization and third order susceptibilities.

Folowing the derivation by Boyd[8], we assume that the interaction of light with a vibrational mode can be modeled using a harmonic oscillator[8], then the displacement $\vec{q}(t)$ with a resonance frequency ω_υ and damping constant γ is given by:

$$\frac{d^2\vec{q}}{dt^2} + 2\gamma\frac{d\vec{q}}{dt} + \omega_\upsilon^2\vec{q} = \vec{F}(t)/m \tag{5.10}$$

where $\vec{F}(t)$ is the applied force on a vibrational mode and m is the reduced mass.

Another assumption is that the optical polarizability of the molecule depends on the internuclear separation $\vec{q}(t)$ and is given by:

$$\vec{\alpha}(t) = \alpha_o + \left(\frac{\partial\alpha}{\partial q}\right)\vec{q}(t) \tag{5.11}$$

where α_o is the polarizability at the equilibrium position.

To induce a dipole on a molecule located at coordinate z, one applies a field $\vec{E}(z,t)$ to polarize the molecule:

$$\vec{p}(z,t) = \varepsilon_o\alpha\vec{E}(z,t) \tag{5.12}$$

The energy due to the polarization is given by:

$$W = \frac{1}{2}\left\langle\vec{p}(z,t)\cdot\vec{E}(z,t)\right\rangle = \frac{1}{2}\varepsilon_o\alpha\left\langle\vec{E}^2(z,t)\right\rangle \tag{5.13}$$

From which the applied force is given by

$$\vec{F} = \frac{dW}{dq} = \frac{\varepsilon_o}{2}\left(\frac{\partial\alpha}{\partial q}\right)_o\left\langle\vec{E}^2(z,t)\right\rangle \tag{5.14}$$

The total optical field can be represented as

$$\vec{E}(z,t) = A_L e^{i(k_L z-\omega_L t)} + A_S e^{i(k_S z-\omega_S t)} + c.c. \tag{5.15}$$

where k_L is the vector due to the laser ω_L is the laser frequency, k_S is due to the Stokes frequency: $\omega_S=\omega_L-\omega_\upsilon$. Plugging in this result into the previous equation, one obtains[8]:

$$\vec{F}(z,t)=\varepsilon_o\left(\frac{\partial\alpha}{\partial q}\right)\left[A_L A_S^* e^{i(Kz-\Omega t)}+c.c.\right] \tag{5.16}$$

where $K=k_L-k_S$ and $\Omega=\omega_L-\omega_S$.

Now to solve Eq. 10, one assumes a trial solution of the form:

$$\vec{q}=q(\Omega)e^{i(Kz-\Omega t)}+c.c. \tag{5.17}$$

Plugging both equations above, one finds:

$$-\omega^2\vec{q}(\Omega)-2i\omega\gamma q+\omega_\upsilon^2\vec{q}(\Omega)=\frac{\varepsilon_o}{m}\left(\frac{\partial\alpha}{\partial q}\right)_o A_L A_S^* \tag{5.18}$$

$$\text{where } \vec{q}(\Omega)=\frac{\left(\varepsilon_o/m\right)\left(\partial\alpha/\partial q\right)_o A_L A_S^*}{\omega_\upsilon^2-\Omega^2-2i\Omega\gamma}. \tag{5.19}$$

The total polarization is given then by $\vec{P}(z,t)=N\vec{p}(z,t)=\varepsilon_o N\vec{\alpha}(z,t)\vec{E}(z,t)$ (5.20)

$$\vec{P}(z,t)=\varepsilon_o N\left[\alpha_o+\left(\frac{\partial\alpha}{\partial q}\right)_o\vec{q}(z,t)\right]\vec{E}(z,t) \tag{5.21}$$

where N is the number of molecules. We are interested in the nonlinear polarizability term[8]:

$$\vec{P}^{NL}(z,t)=\varepsilon_o N\left(\frac{\partial\alpha}{\partial q}\right)_o\left[\vec{q}(\Omega)e^{i(Kz-\Omega t)}+c.c.\right]\times\left[A_L e^{i(k_L z-\omega_L t)}+A_S e^{i(k_S z-\omega_S t)}+c.c.\right] \tag{5.22}$$

Out of this equation comes the "Stokes polarization"[8] due to oscillation at frequency ω_S:

$$\vec{P}_S^{NL}(z,t)=P(\omega_S)e^{i\omega_S t}+c.c \tag{5.23}$$

with $P(\omega_S)$ is given by:

$$P(\omega_S) = N\varepsilon_o\left(\frac{\partial\alpha}{\partial q}\right)_o q^*(\Omega)A_L e^{ik_S z}$$
$$= \frac{\left(\varepsilon_o^2/m\right)\left(\partial\alpha/\partial q\right)_o^2 |A_L|^2 A_S}{\omega_\upsilon^2 - \Omega^2 + 2i\Omega\gamma} e^{ik_S z} \tag{5.24}$$

Rewriting this solution for the polarization[8,37] to condense the contributions by the electric fields:

$$\bar{P}(w) = \frac{\left(N/m\right)\left(\partial\alpha/\partial q\right)_0^2}{\omega_\upsilon^2 - \left(\omega_p - \omega_S\right)^2 - 2i\left(\omega_p - \omega_S\right)\gamma} E_p^2 E_S^* = 3\chi^{(3)}(\omega_{as})E_p^2 E_S^* \tag{5.25}$$

where N is the number of oscillators, m is the reduced nuclear mass, γ is the damping constant, α is the Raman polarizability, q is the molecular vibration coordinate. From this equation we can obtain a formula for the third order susceptibility by comparison to Eq. 5.4[14,37]:

$$\chi^{(3)}(\omega_{as}) = \frac{\left(N/3m\right)\left(\partial\alpha/\partial Q\right)_0^2}{\omega_\upsilon^2 - \left(\omega_p - \omega_S\right)^2 - 2i\left(\omega_p - \omega\right)\gamma} \tag{5.26}$$

The nonlinear susceptibility is a property that describes the mediums's response to the applied laser fields with a peak at resonance ($\omega_p - \omega_S = \omega_\upsilon$). Since the susceptibility is proportional to the number of oscillators, the CARS signal is quadratic in the number of oscillators.

The vibrational resonant signal is not the only contribution seen in CARS. Other processes due to pure electronic nonresonant contributions can give an anti-Stokes signal. Out of the 24 different quantum mechanical paths[14] that give rise to an anti-Stokes signal, only 4 of these terms contribute to the vibrationally resonant CARS signal.

5.2.1.3. Phase matching

For the signal in Eq. 7, the phase-matching condition is $\Delta k\, l << \pi$. For very small l, both F-CARS and E-CARS are the same. As l increases in size, the two signals are no longer equivalent. For minimal changes in the index of refraction, F-CARS signal has $\Delta k=0$ and $I_{F\text{-}CARS} \propto l^2$. The E-CARS signal phase matching condition is $\Delta k=4n\pi/\lambda_{as}$. Thus, the signal oscillates as a function of l with a period equal to $\lambda_{as}/2n$. Similarly, for tightly focused beams[214] there is a quasi quadratic dependence of $I_{F\text{-}CARS}$ on l and $I_{E\text{-}CARS}$ approximates a periodicity of $\lambda_{as}/2n$. E-CARS has very low signal for large l ($\sim\lambda_p$).

5.2.2. STimulated Emission Depletion, Black Body Radiation and RESOLFT

We would like to start our discussion of STED with the definition of the spontaneous and stimulated emission (A and B) Einstein coefficients. For clarity, we will present the semiclassical derivation of these quantities[215,216] that mirrored Einstein's pioneering work.[217]

5.2.2.1. Black Body Radiation and the Einstein coefficients

Starting with a two state system with number of particles N_a in the ground state and N_b in the excited state with an energy density of radiation at the frequency of the transition with frequency ω_o given by $\rho(\omega_o)$, we can say then that the transition rate of molecules moving from the ground state to the upper state is given by:

$$\frac{dN_b}{dt} = +N_a B_{ab} \rho(\omega_o) \tag{5.27}$$

This is also the rate that a molecule is induced to return to the ground state from the excited state, and we can define the Einstein coefficient of stimulated emission as B_{ba}. The number of particles leaving the excited state to the ground state by stimulated emission is given by:

$$\frac{dN_b}{dt} = -N_b B_{ba} \rho(\omega_o) \tag{5.28}$$

At the same time, the other possible process that can take a photon from the excited state to the ground state at a given rate A, is spontaneous emission. This process is completely independent of the applied field. The number of particles leaving the excited state by spontaneous emission is given by:

$$\frac{dN_b}{dt} = -N_b A \tag{5.29}$$

Therefore the rate equation for the excited state is given by:

$$\frac{dN_b}{dt} = +N_a B_{ab} \rho(\omega_o) - N_b A - N_b B_{ba} \rho(\omega_o) \tag{5.30}$$

If we assume that we are in equilibrium, $\frac{dN_b}{dt} = 0$ and we can solve for $\rho(\omega_o)$,

$$\rho(\omega_o) = \frac{A}{\left(\frac{N_a}{N_b}\right) B_{ab} - B_{ba}} \tag{5.31}$$

If we compare this formula to the Planck's blackbody formula for the energy density of thermal radiation:

$$\rho(\omega_o) = \frac{\hbar}{\pi^2 c^3} \frac{\omega^3}{e^{\hbar\omega / k_b T} - 1} \tag{5.32}$$

Using the key Einstein conjecture that these are in fact the same, one concludes that

$$B_{ba} = B_{ab} \text{ and } A = \frac{\omega^3 \hbar B_{ab}}{\pi^2 c^3} \qquad (5.33)$$

The first part of Eq. 33 demonstrates that the rate of stimulated emission and stimulated absorption are both as probable. In our discussion, this equality implies that illuminating an excited ensemble with energy equal to the energy gap between B and A, will stack the odds in favor of stimulated emission. If the laser pulse occurs at a time point before the molecules are allowed to relax through spontaneous emission, the result is coherent emission of the excited population back to the ground state. Lasers (*l*ight *a*mplification by *s*timulated *e*mission of *r*adiation) make use of this principle. In our case, we prevent the later emission of the photons at energies throughout the band by applying our narrow line depleting beam *before* significant emission can occur, rapidly *quenching* the emission.

5.2.2.2. RESOLFT

Following the basic theory developed by Hell *et al.*[218,219], the principle behind STED imaging is based on reversible saturable optically linear (fluorescence) transition (RESOLFT) technique between two molecular states. In essence, the process involves exciting a dye molecule from the ground state to a first excited state. The transition from the excited state back to the ground state normally occurs through fluorescence. But the same transition can also be induced through stimulated emission[217] by a photon with the same energy as the gap between the excited state and the ground state. Starting with

spontaneous rates of A → B and B → A given by k_{AB}^{s} and k_{BA}^{s}, respectively and allowing for light-driven rates proportional to the depleting intensity: $\sigma_{AB}I$ and $\sigma_{BA}I$.

Then the populations of the two states n_A and n_B over time are given by:

$$\frac{dn_A}{dt} = -k_{AB}n_A + k_{BA}n_B = -\frac{dn_B}{dt} \tag{5.34}$$

with $k_{AB} = k_{AB}^{s} + \sigma_{AB}I$ and $k_{BA} = k_{BA}^{s} + \sigma_{BA}I$.

The probability that a molecule stays in state A is given by:

$$N_A = (1 - N_A)e^{(-(k_{BA}+k_{AB})\tau)} + N_{eq} \tag{5.35}$$

where the equilibrium population and the relaxation rate are given by: $N_{eq}=k_{BA}/(k_{BA}+k_{AB})$

(5.36)

Under ideal conditions, there is no broadband signal generated during the depletion process and the signal depends solely on the excitation probability multiplied by the probability of staying in state A:

$$p_A(r) = e^{(-1\sigma\tau)} \tag{5.37}$$

The RESOLFT process starts with all the molecules in the ground state (state B). Assuming a Gaussian distribution for the focal intensity, the distribution of particles excited by the first beam is given by:

$$N_A^{(1)}(r) = e^{\left(\frac{-r^2}{a^2}\right)} \tag{5.38}$$

where a is the 1/e radius in this case and is related to the FWHM by $\Delta r = 2a\sqrt{\ln 2}$. Also, the "donut" focal distribution of the depleting laser light is given by

$$I(r) = I_{\max}\left[1 - e^{\left(\frac{-r^2}{a^2}\right)}\right] \tag{5.39}$$

Combining the probability of staying in state A (excited state) with the focal intensity to get N_A after depletion:

$$N_A^{(2)}(r) = N_A^{(1)}(r)\,p_A(r) = \exp\left(\frac{-r^2}{a^2}\right)\exp\left(-\xi\left[1-\exp\left(\frac{r^2}{a^2}\right)\right]\right) \qquad (5.40)$$

where $\xi=\ln 2\ I/I_{sat}$ is the saturation factor.

The FWHM of N_A is given by:

$$-\ln 2 = \frac{-r^2}{a^2} - \xi\left[1-\exp\left(\frac{r^2}{a^2}\right)\right] \qquad (5.41)$$

After a linear approximation of the exponent and using the definition of Δr, we obtain:

$$\Delta r(\xi) = \frac{\Delta r}{\sqrt{1+\xi}} = \frac{\lambda}{2NA\sqrt{1+\xi}} \qquad (5.42)$$

Setting $\xi=0$ returns Eq. 1, but the interesting result occurs as $\xi\to\infty$. Under this condition, the spot becomes infinitesimally small.

5.3. Materials and Methods

5.3.1. General setup

5.3.1.1. CARS setup

Figure 5.5 shows the current general layout for the CARS setup. A Verdi X CW doubled Nd+:YLF laser pumps a Mira 900 tunable modelocked Ti: sapphire laser (Coherent) that is used both as a Stokes beam and to synchronously pump an internally doubled ring optical parametric oscillator (Mira-OPO) synchronized to the Mira , providing the 'pump and probe beam' (all ~1.5 ps pulses).

The beams are spatially and temporally overlapped over a large distance and telescoped to 8x their original size to backfill an objective (60x Olympus oil immersion UPlanSApo (NA=1.4) or a 100X Zeiss PlanNeoFluar (NA=1.3)) mounted on a Zeiss Axiovert 135M microscope. The detection is performed using slight modifications to the Alba II (ISS) detection system normally used for FCS. The Alba II contained two separate channels with one APD each. The incoming signal was sent through a dichroic mirror that rejected the Stokes and probe beams. The signal was further split by a 50/50 beamsplitter before entering the APDs (See Figigure 5.5).

An image is obtained by raster scanning the sample using a piezo stage (Madcity Labs) for xy control and a z piezo controller (Madcity Labs) with resolutions of 256 x 256 or 512 x 512 pixels. The dwell times varied between 0.2 to 2 ms per pixel.

Figure 5.5. The general setup in use for CARS. The probe/pump beam is a Mira laser at 785-790nm and the Stokes laser has a "visible" wavelength depending on the vibrational mode needed to excite. AC=Autocorrelator, BE=Beam Expander,BS=Beam splitter, DM=Dichroic Mirror,L=lens, F=Filter (depending on the CARS signal), Ob=objective (60x, NA=1.4) mounted on a Axiovert 135M microscope, OD=Optical Delay, P=Polarizing cube, PH=pinhole, SF=Spatial Filter, λ/2 half wave plate and λ/4 quarter wave plate.

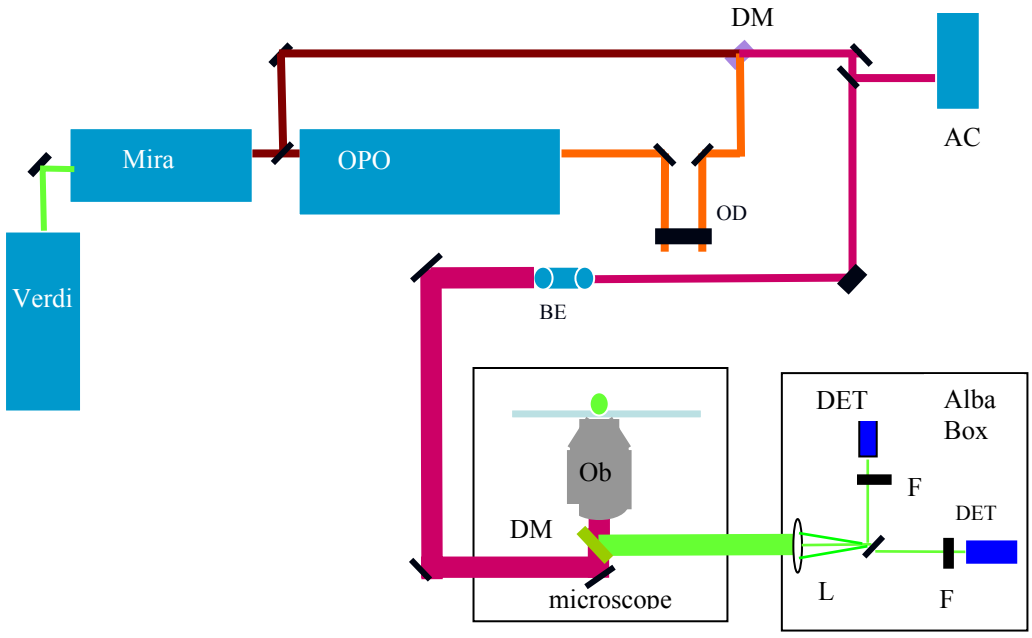

5.3.1.2. Excitation of the vibrational modes

To excite the lipid 2845 cm^{-1} vibrational mode, we use 785nm and 641.7nm beams from the Mira 900 and the Mira/OPO, respectively, with an Anti-Stokes signal emerging at 540 nm. For the NAD^+ mode[220] (1032 cm^{-1}), we use a 780nm beam (Stokes) combined with a 732nm (pump/probe) beam with a signal seen at 670nm. The fluorescent

signal of NADH *only* is detected in one of the channels by using a 500LP and a 600SP filter to block scattered light or the CARS signal. The NAD^+ signal is detected in a separate channel using a stack of filters to block background observed from other nonlinear processes. They include two 700SP and a 670 (+/-10nm) interference filter. In the case of water, we tuned the laser beams to excite the 3340 cm^{-1} band of the O-H stretch The wavelengths used for water were λ_p=620.7 and λ_S=783.2 nm with a λ_{CARS}=510nm. To detect the water signal, one channel was used in the Alba setup by removing the 50/50 BS allowing all the light to hit one APD detector. A 510 +/- 20 nm filter (Semrock) to select for the CARS signal with two 600SP filters (Thorlabs) were used to block the IR light from reaching the detector.

5.3.1.3. NADH/NAD^+ vesicles preparation

The vesicles were provided by Dr. Lesley Davenport (CUNY, NY). Briefly, the vesicles of different sizes were prepared by a fixed-pore membrane extrusion process (six times) while loaded with NAD^+ and/or NADH. The solutions were eluted through NAP-10 columns to remove any residual NAD^+/NADH in the surrounding buffer.

5.3.1.4. HeLa cells for water/D_2O studies

For the live cells studies, HeLa cells were kindly provided by Dr Ling Yi in Dr. S. Venkatesan's lab from NIAID, NIH. The HeLa cells were plated to 50% confluency and maintained in DMEM buffer with 0.2% FBS at 37C until they were used for imaging at 25C. Immersion oil (Zeiss, 518F) was used to cover the cells to give a change in the

index of refraction between the water layer covering cell and oil. For the D_2O experiments, D_2O from Sigma (99.9%) was used to quickly exchange the buffer.

5.3.2. STED setup

The STED setup is similar in layout to the CARS setup (See Figure 5.6). A spatial filter was added to each beam to obtain clean Gaussian profiles. The visible excitation beam (565nm) was focused into a pinhole (15 μm) using an aspherical lens f=13.8 mm (25.4 mm dia). The resulting beam was expanded and collimated using a f=75mm lens (25.4mmdia) providing a large diameter used to overfill the 100x objective (NA=1.45, Olympus UPLANSAPO) in a Zeiss Axiovert 135M microscope. The total visible power reaching the microscope was 300 μW. The fluorescence was detected in an epi-configuration with a 450-700BP dichroic (Chroma) and passed to the Alba II spectrometer. Because STED required confocal detection of the fluorescence, a pinhole was placed in front of the first detector (DET1). The pinhole size was varied between 12.5, 17 and 50μm depending on the fluorescence intensity. The STED beam was overlapped with the visible beam using a dichroic mirror (700SP, Chroma) before reaching the microscope. The STED beam (777nm) was focused into a pinhole (20μm) using a f=50mm lens (25.4 mm dia). The beam was collimated with a 100mm lens (25.4 mm dia). After the expansion, the beam was attenuated using a $\lambda/2$ waveplate and polarizing cube. The STED beam was steered through a vortex phase plate (VPP-1 from RPC Photonics) that created the 'donut' hole. The phase plate imprints on the wave front a helical phase of $\exp(i\phi)$ with $0 \leq \phi \leq 2\pi$ (Figure 5.7). After the beams are overlapped in space, an autocorrelator was used to ascertain the relative position of the two beams in

time. Before the objective and after the primary dichroic, a λ/4 plate was placed to obtain a completely circularly polarized beam. The visible beam arrives about 5 ps ahead of the STED beam. The STED beam power ranged from 10-90mW.

Figure 5.6. STED system setup. Setup is similar to CARS except that a phase plate produced the 'donut beam'. AC=Autocorrelator, BE=Beam Expander,BS=Beam splitter, DM=Dichroic Mirror,L=lens, F=Filter (depending on the CARS signal), Ob=objective (60x, NA=1.4) mounted on a Axiovert 135M microscope, OD=Optical Delay, P=Polarizing cube, PH=pinhole, SF=Spatial Filter, λ/2 half wave plate and λ/4 quarter wave plate.

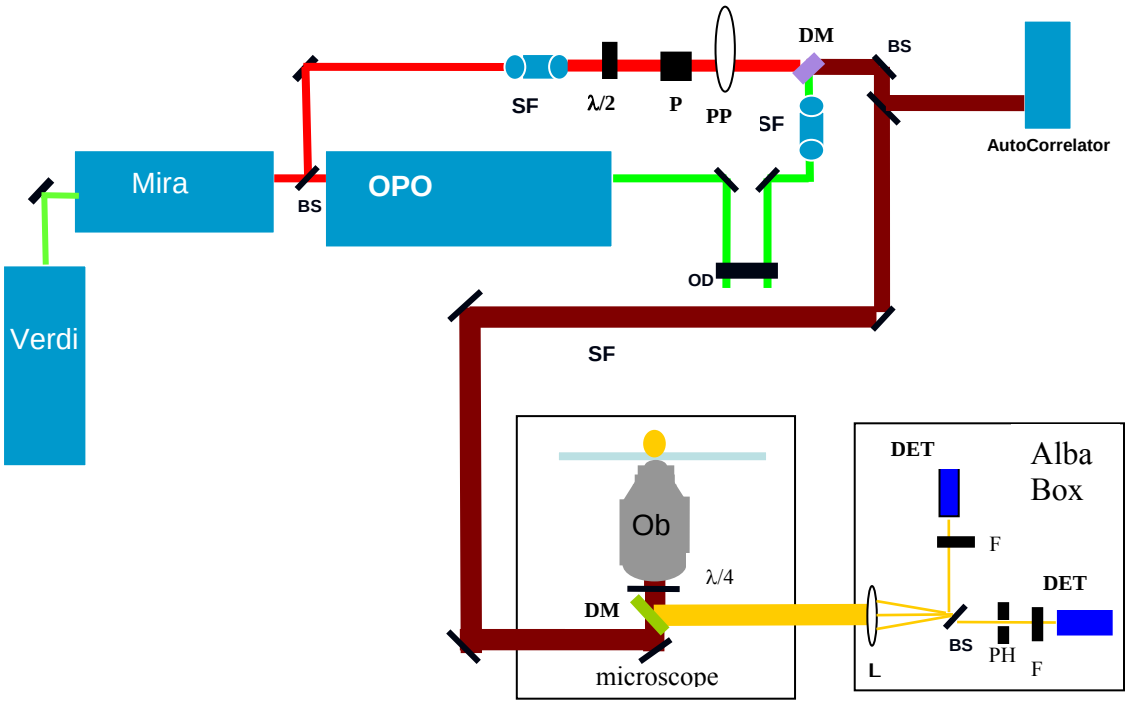

Figure 5.7. Phase plate diagram and destructive interference. A) Diagram of phase plate. The VPP-1 from RPC photonics is a continuous phase plate that provides a phase delay from 0 to 2π to the incoming beam. B) An incoming beam after passing through the phase plate (PP) has a slight phase delay applied to it. When the beam is focused, the beam destructively interferes to give a zero intensity center.

A)

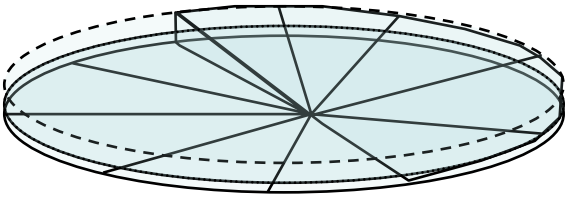

B)

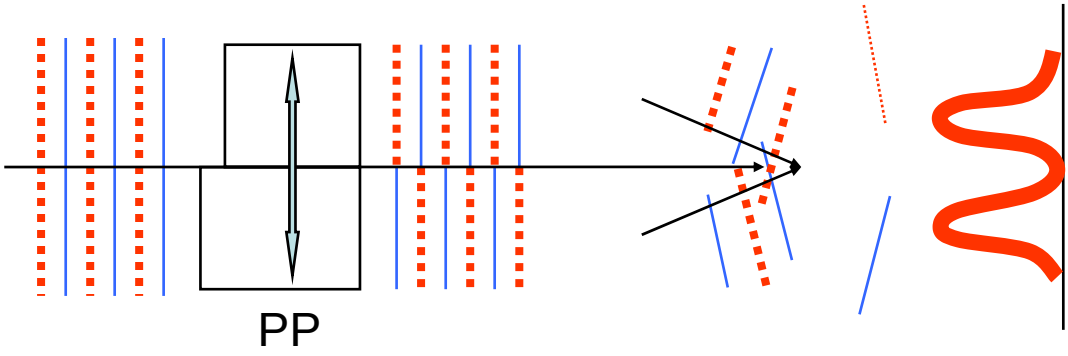

5.3.2.1. Sample preparation

Latex beads of 100nm in diameter coated with aliphatic amines (Invitrogen, P37355) were labeled with Atto 647N-NHS using the provided labeling protocol. After the reaction, the beads were centrifuged for twenty minutes at 5000rpm to separate the reaction buffer from the pelleted beads. To completely remove any unbound dye, the beads were dialyzed in water at 4C for 2 days using a 3000 MWCO Slide-a-Lyzer dialysis cassette (ThermoScientific). About 1 μL of the dialyzed beads was placed in a Labtek II chamber coverglass (Nuntech). 80μL of water were added to dilute the beads and allowed to dry. Mounting medium or glycerol was used to cover the dried beads. For alignment of the 'donut' STED beam and beam overlap, deep red beads (P7220) from Invitrogen 170nm in diameter were used. A novel dye with good STED characteristics was synthesized for us by Dr Gary Griffiths of NHLBI. The dye was synthesized by combining elements of rhodamine 6G and NIR dye. IR125 (Exciton Inc.) coupled by six proline amino acids to maintain rigidity and spacing. The IR125 dye is excited by the 777 nm laser beam producing a transient absorbing state that overlaps the emission of rhodamine 6G. In this way, the fluorescence of rhodamine 6G is quenched only when the 777nm laser beam is turned on in a process named STAQ (Superresolution using Transiently Activated Quenchers).

5.4. Results and Discussion

5.4.1. CARS Results and Discussion

5.4.1.1. Images of polystyrene beads and extruded lipid vesicles.

Our first experiments with the CARS assembly imaged polystyrene beads (~5 μm dia) by exciting the C-H vibrational mode at 2900 cm^{-1}. Figure 5.8 shows the E-CARS signal obtained from 5 μm polystyrene (PS) beads. The observed 'hollowness' arises from dephasing of the E-CARS signal as demonstrated by Volkmer *et al.*[195] Figure 5.9 shows CARS image obtained from 0.6 μm vesicles that are clearly seen via the lipid vibrational mode of 2845 cm^{-1}. The vesicles were suspended in 1% agarose to prevent them from moving. This embedding in hot agarose, unfortunately, reduces the fraction of intact vesicles in the field.

Figure 5.8. CARS image of 5 μm polystyrene beads in glycerol. 256 x256 image scanned at 0.5ms per pixel. Note the "hollowness" of the PS beads. This effect is due to dephasing of thicker sections PLUS reflection of forward CARS at interfaces.

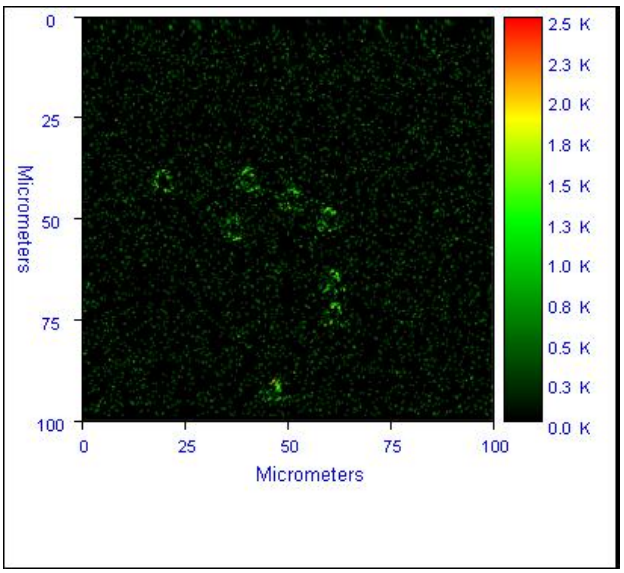

Figure 5.9. CARS image of isolated 0.6 μm lipid vesicles (red arrow). CARS signal at ω_v=2845 cm^{-1} (lipid). The image resolution was 512x512 at 1ms per pixel residence time.

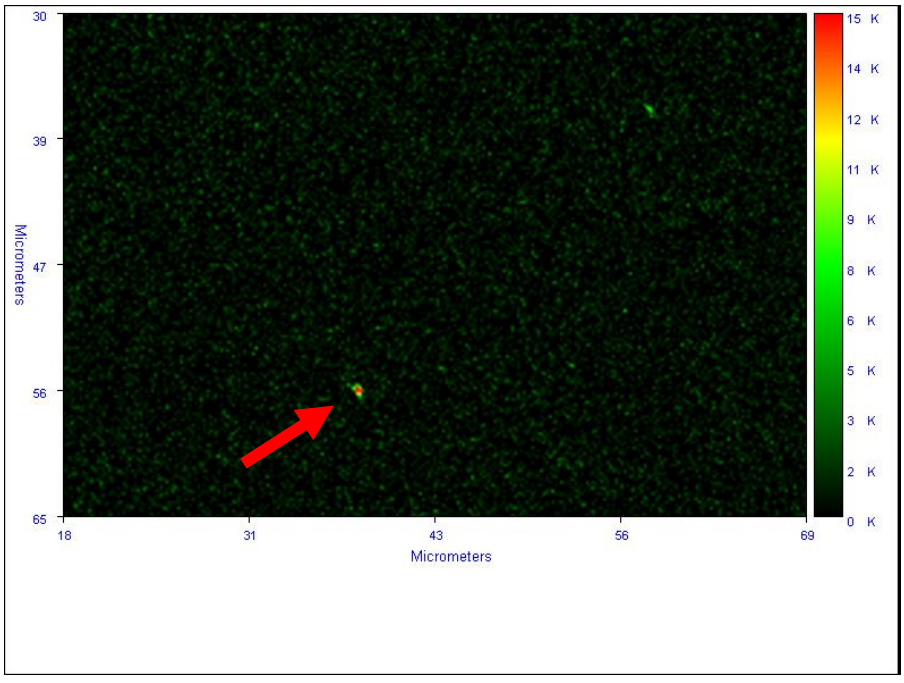

5.4.1.2. NAD^+ and NADH vesicles

Figure 5.10 shows the fluorescence of NADH (1mM) containing vesicles (5 μm dia). The fluorescence is produced by a weak two photon effect from both the 789nm probe beam and (predominantly) the 732nm Stokes beam. Two photon fluorescence from a picosecond pulse is >100-fold weaker than two photon fluorescence from 100fs pulses, but compares to CARS signal (which is also a weak signal). Figure 5.11 has the CARS signal of NAD^+ filled vesicles (1032 cm^{-1}). We are able to recover a signal to noise better than 50.

Figure 5.10. CARS image of NADH filled vesicles (5μm dia). Weak fluorescence using 732 nm and 790 nm beams. The fluorescence originated mostly from weak 732nm two-photon excitation.

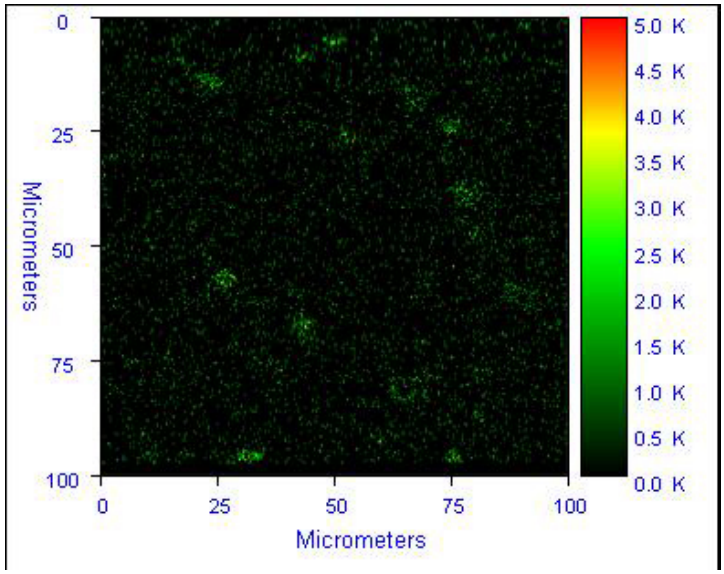

Figure 5.11. CARS image of NAD^+ filled vesicles (~5μm in diameter). Vibrational mode used was ω_v=1032 cm^{-1} with wavelengths: λ_s=790 nm, λ_p=730 nm, λ_{CARS}=679 nm.

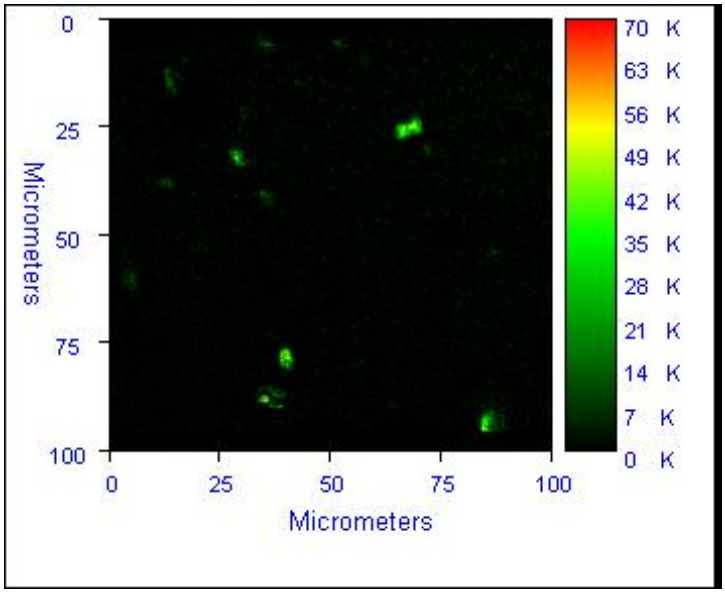

5.4.1.3. Water CARS

Our first attempts to image water were to image 'inverted' vesicles in DPPC. Figure 5.12a shows the results obtained for a group of vesicles that had started to fuse when the scans were acquired. Figure 5.12b shows the intensity cross-section shown in the red line in Figure 5.12a. Because temporal overlap is required for CARS, by delaying the visible beam by more than 5 ps, the signal was lost as seen in Figure 5.12c.

Having demonstrated that we are able to visualize water using CARS imaging, we attempted to image HeLa cells *in vitro*. Figure 5.13a has a representative image. The red rectangle was imaged at a higher resolution and is shown in Figure 5.13b. There was very low signal for these measurements but the S/N was adequate for E-CARS to provide definitive images. Potma *et al.*[212] imaged water in cells using F-CARS and the images are

comparable except for the large background signal in F-CARS. A HeLa cell undergoing apoptosis is shown in Figure 5.14. The cell had emptied its contents to the surroundings. One consistent observation was that in E-CARS the smaller vesicles produced stronger signals. Our attempts to quickly remove the surrounding serum and replace it with D_2O are shown in Figure 5.15. The signal due to water decreased significantly. Later recovery of the water CARS signal was impossible since the cells did not survive the slow buffer exchange process. The loss in signal is also comparable to observations made by Potma *et al.*[212] Figure 5.16 shows HeLa cells with serum replaced by immersion oil. The cells again do not survive for very long and can be seen to undergo apoptosis (morphology changes and disruption of cell membrane).

Using immersion oil produces a change on the index of refraction at the interface between water at surface of cells and oil leading to an improvement in contrast from the previous images of water in HeLa cells. Immersion oil is toxic and was used only because it was at hand, more benign mounting solutions will be attempted in the future.

Figure 5.12. CARS image of water filled inverted vesicles. A) The metastable inverted vesicles did not last long. As can be seen in the image, the water vesicles had started to coalesce by the time the image was acquired. B) Intensity cross section across the red line in Figure 5.12a. C) 'Detuning' the temporal overlap completely destroyed the signal.

A)

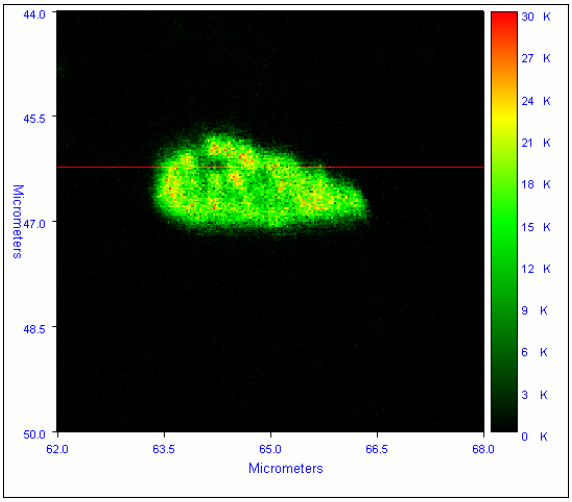

B)

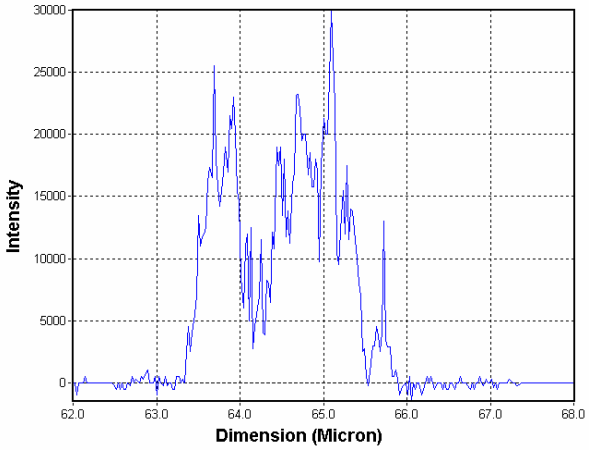

C)

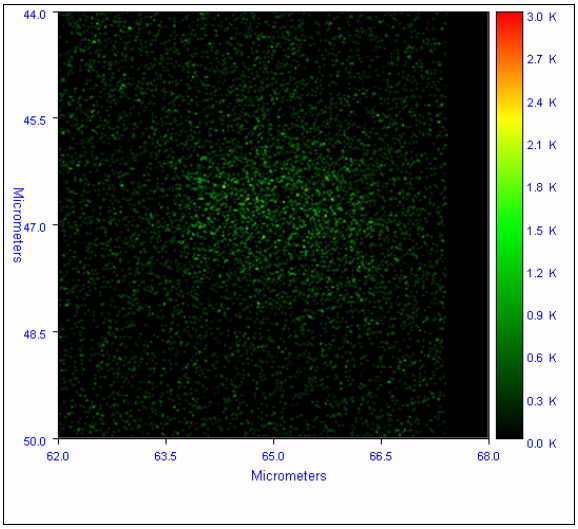

Figure 5.13. Water in HeLa cells imaged using E-CARS. A) a 100x100μm scan of HeLa cells. Note that the E-CARS signal is strong at smaller vesicles. B) The cells imaged in the red square at a higher resolution (2ms/pixel).

A)

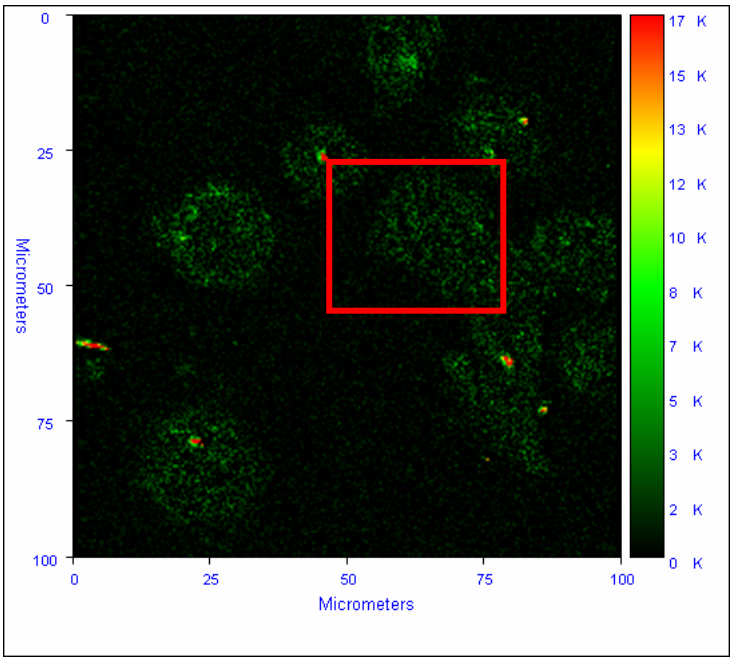

B)

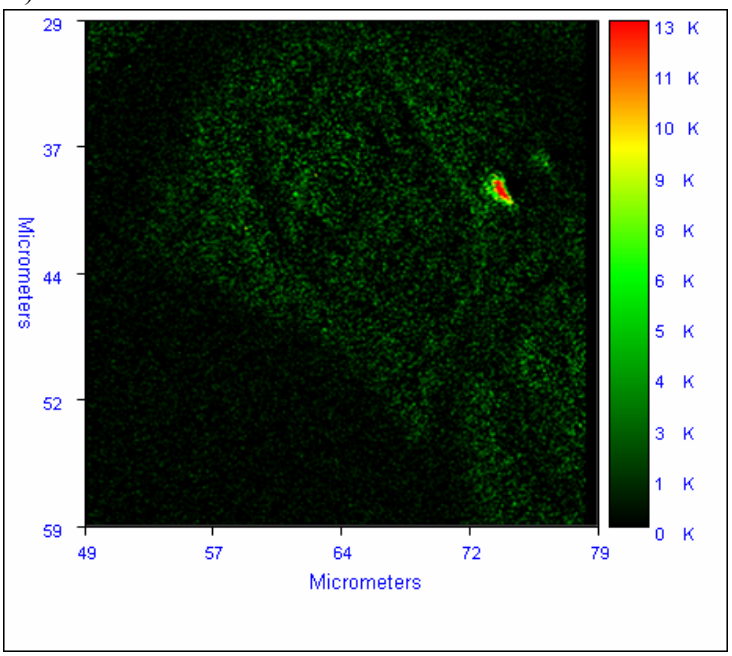

Figure 5.14. CARS image of water in HeLa cells (dying cell). A dying cell, spilling its contents (barely visible in th upper left corner). Note that the smaller structures at edges produce a stronger E-CARS signal.

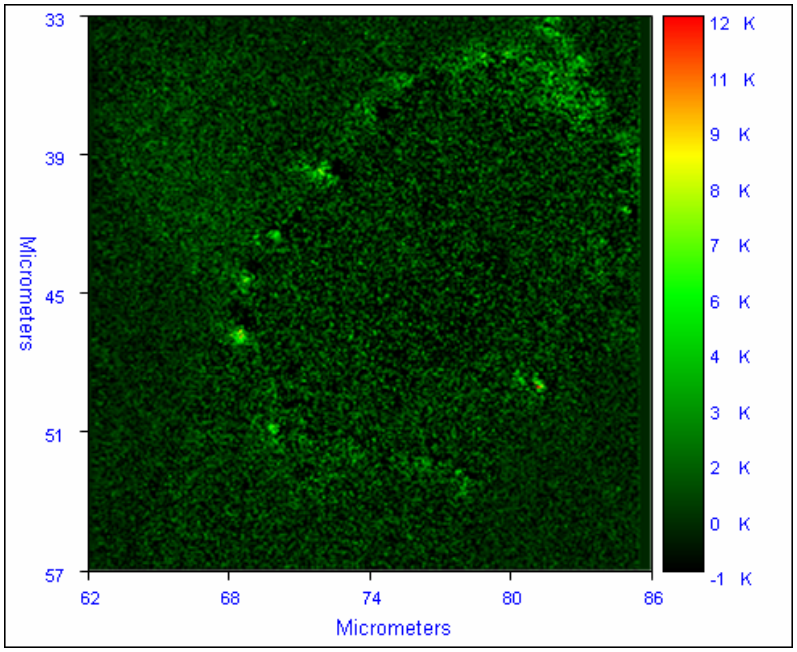

Figure 5.15. CARS image of HeLa cells. The medium was exchanged with D_2O. Exchanging the medium containing water with D_2O decreased the intensity of the signal. A) Initial image of a HeLa cell in cell medium. B) Exchange occurred rather quickly and an image was taken before cell death (evidenced by cell membrane disruption).

A)

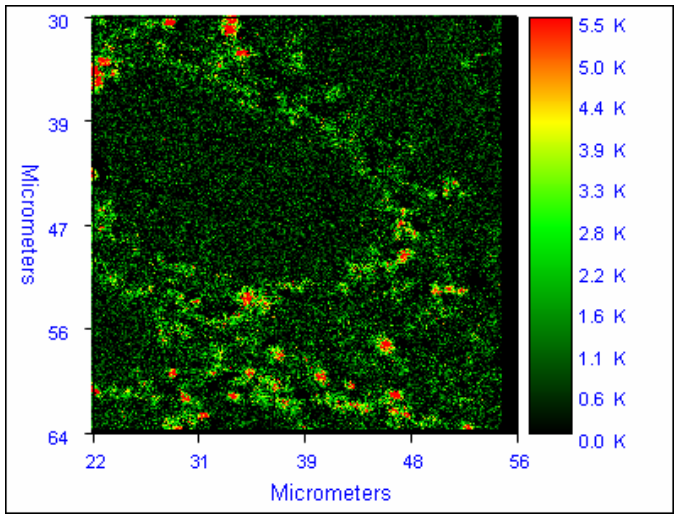

B)

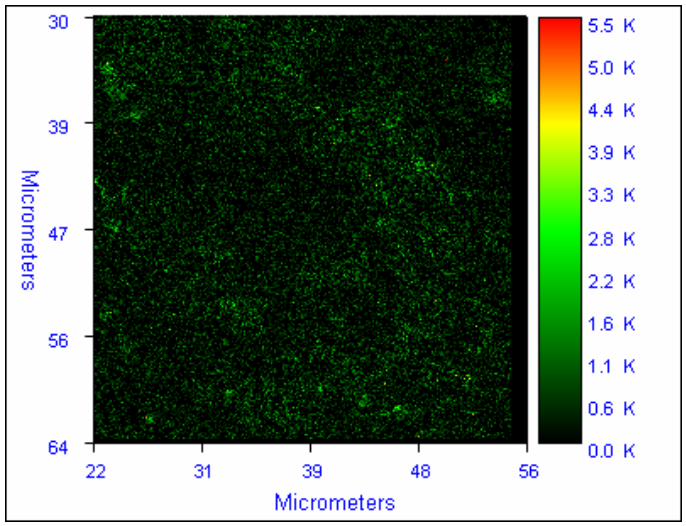

Figure 5.16. CARS image of water in HeLa cells. The medium surrounding the cells had been replaced with immersion oil. The better contrast compared to earlier images is due to E-CARS dependence on the index of refraction.

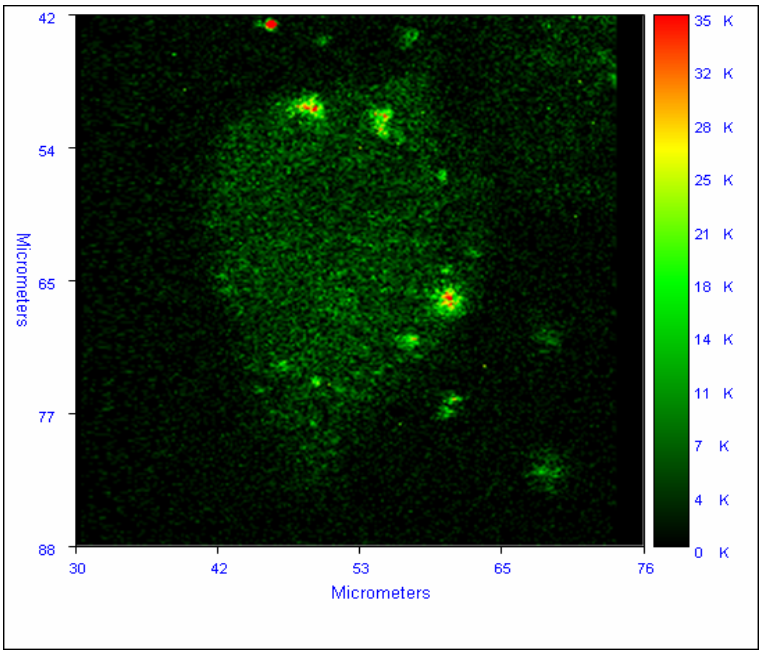

Concurrent observation of NADH and NAD^+ is possible using our current setup. The fluorescent signal from NADH has a long tail that can obscure the CARS signal (even at 670nm). However, NAD^+ E-CARS signal is surprisingly strong for a vesicle of this size (5 μm). We suspect this signal is actually a *forward* CARS signal reflected back into the objective, and we are developing alternative sample holding methods to test this hypothesis. The theoretical epi-intensity obtained for a sphere of this size should be very small.[194]

Future plans involve obtaining a calibration curve for NAD^+ by quantifying vesicles with different ratios of NAD^+ and NADH. We are also developing the ability to

simultaneously measure F-CARS by putting a PMT and condenser above the sample or move to another microscope with forward detectors. The ability to detect F-CARS will help us better understand our size-dependent results for NAD^+ filled vesicles.

5.4.2. STED Results and Discussion

The first step to obtain a STED image was to create a deactivating donut beam like the one shown in Figure 5.17a. We were able to image the shape of the donut because the 777nm beam weakly excited the deep red beads by two-photon excitation. As the power of the STED beam was increased, the probability of depleting the fluorescence increased reducing the center hole diameter. STED is able to deplete the fluorescence that falls under the donut. Figure 5.17b shows the confocal image obtained from the visible beam alone (excitation at 565nm). As soon as the STED beam was turned on (777 nm), the fluorescence in the donut disk was depleted leaving behind only the fluorescence in the center. The overlap of the donut beam with a confocal diffraction spot resulted in the STED image shown in Figure 5.17c. The improvement of the axial distance resolution went from FWHM of 470μm to 269μm. Upon refinement of our confocal geometry, a better example that went well beyond the diffraction limit was obtained (Figure 5.18). The results shown in Figure 5.18(c and d) include fits of the peak to a Gaussian profile. For the confocal image (Figure 5.18c), the fit reaches the maximum achieved by the data points. But for the STED image (Figure 5.18d), the best fit to a Gaussian does not reach the maximum amplitude. So, we are overestimating the true Full Width at Half Maximum (FWHM) of the STED image. A ~170nm 'bead' has been included on Figure 5.18c and 18d to demonstrate that the edges of the STED profile are closer to the actual size than

the confocal image. If we were to correct the FWHM corresponding to the maximum amplitude of the STED image and bead shape, we would have resolution of *about* 100nm for this bead (238nm diffraction limit).

We have been able to demonstrate that our newly synthesized dye can be depleted at 777 nm and excited at 565 nm. Small amounts of the novel dye were sprayed onto a LabtekII chambered coverglass and allowed to dry. The initial STED-like images for the novel dye are shown in Figure 5.19 in a process named STAQ (Superresolution using Transiently Activated Quenchers). By coupling other dyes with IR125, we are capable of using different excitation beams but requiring only one depleting beam. This chimera has great potential in reducing the total power required for superresolution by surrounding one rhodamine 6G with many IR1250 dyes so that less power from the depleting beam is required to quench rhodamine 6G fluorescence. (A test solution containing only rhodamine 6G produced doubling of the signal intensity because the 777 nm laser beam produced a two-photon signal from rhodamine 6G alone).

Figure 5.17. STED images of deep red fluorescent beads (170nm dia). A) Fluorescent beads that have slight two photon absorption from the 777nm beam allow observation of the STED donut. B) Confocal image of deep red beads due to visible only (565nm). C) STED image arising from the combination of the visible beam plus the STED beam (777nm).

A)

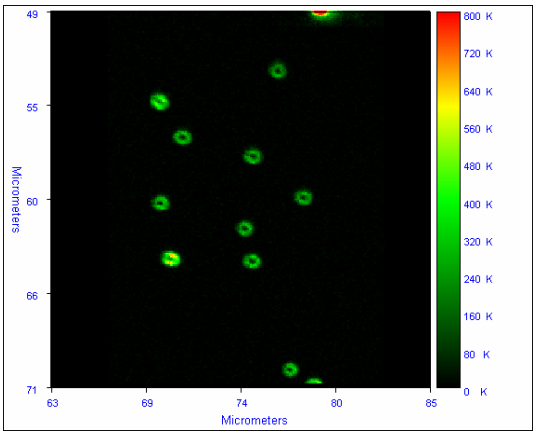

B)

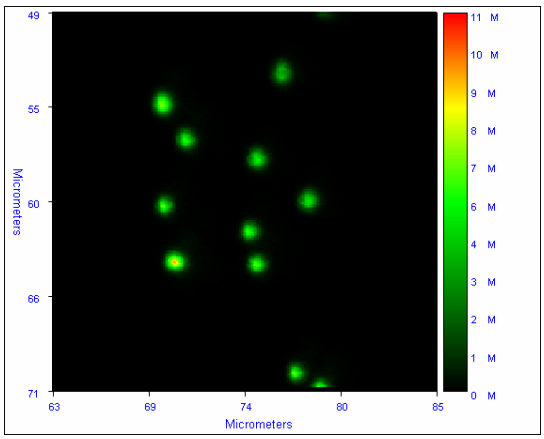

C)

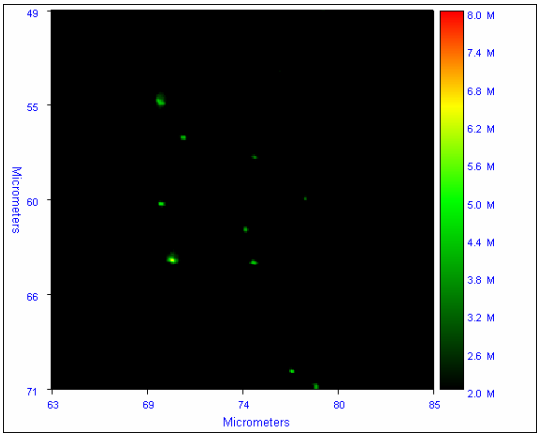

Figure 5.18. STED image of deep red beads beyond the diffraction limit. The FWHM was obtained by fitting the profile to a Gaussian peak, see C) and D). A) Confocal diffraction limited spot (FWHM= 330 μm). B) STED image with FWHM of 217μm. The diffraction limit for 565 nm light is 237 μm. C) Horizontal intensity profile of the top right bead for Figure 5.18A. A green circle is placed at approximately the FWHM. D) Horizontal intensity profile of the same top right bead for Figure 5.18B. A green circle is placed at approximately the size of the 170 nm bead.

A)

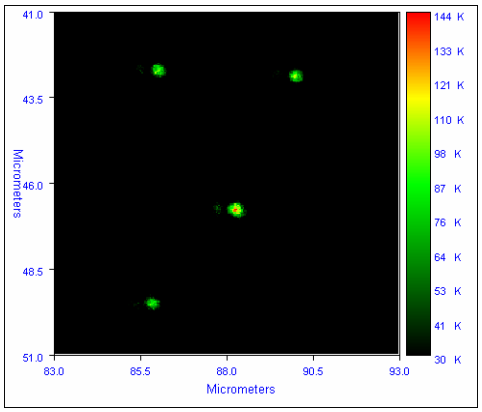

B)

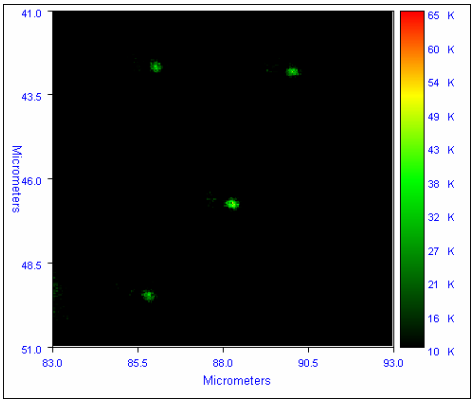

C)

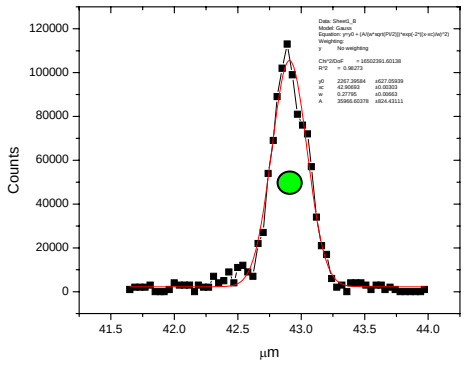

D)

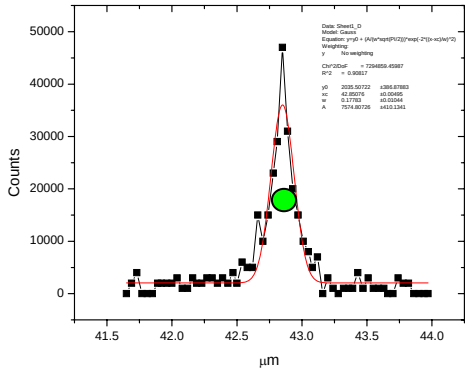

Figure 5.19. STED image of the novel dye dried onto a coverglass chamber. A) Confocal image excited at 565nm. B) STED image using a 777nm depletion beam.

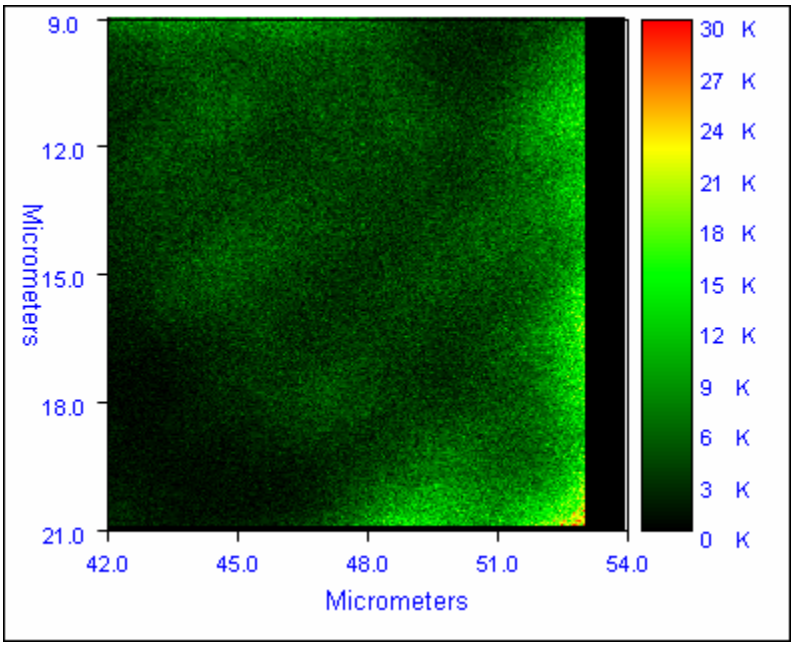

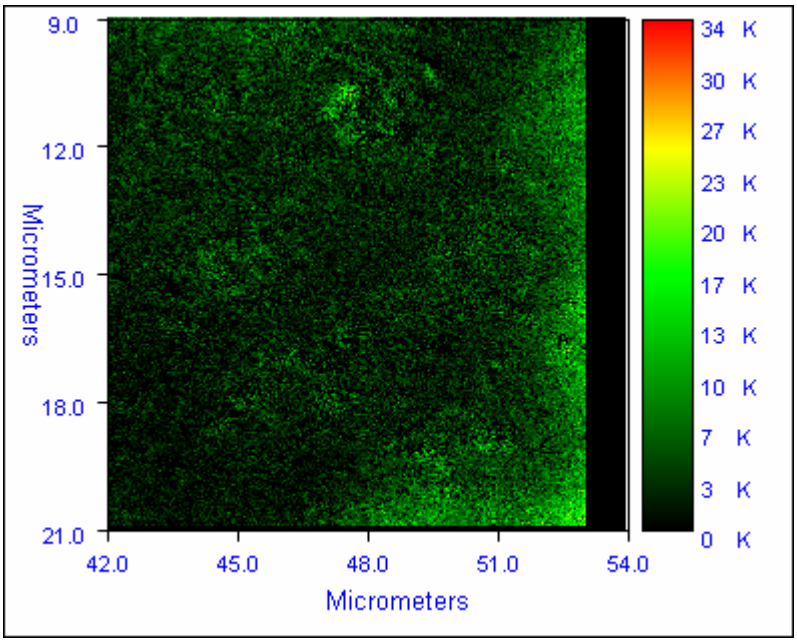

Images shown in Figures 5.17 through 5.19 show that our system using STED can overcome the diffraction limit that typically restricts microscopy experiments. We have also shown that the new dye is capable of producing depleted images. In principle, STED has no limit to the resolution that can be obtained as long as the fluorophore can be fully depleted. Work on nitrogen doped diamond nanoparticles demonstrated that the resolution can be taken down to a few nanometers with Angstrom precision.[221] Most of the work using this technique has focused on single (or few) images of living systems using fluorescent proteins[206,222] and other molecular labels[48].

If STED-like nanoscopy can be achieved at lower powers (more tolerable to living tissue) through novel dyes, live cell "time-lapse" movies can be anticipated with unprecedented value in cell biology.

Chapter 6: Conclusions

The focus of this dissertation has mostly centered on the development of optical techniques for studying molecular interactions in solution by observing the translational and rotational motion. Chapter 2 examined the translational motion of proteins in live cells. Experiments used two-photon, two-color Fluorescence Correlation Spectroscopy (TPTCFCCS) to quantify protein:protein interactions in live cells. Among the systems studied we surveyed the AR-Tif2 coactivator interactions to demonstrate the capabilities of FCS to measure drug-dependent protein binding in live cells. With the c-myc-eGFP construct in mouse embryo fibroblast cells, we demonstrated the capability of FCS to measure very low concentrations in live cell nuclei (corresponding to only a few hundred copies of c-myc protein). In Chapter 3, we modeled the rotational motion of perylene and tetracene molecules in n-hexadecane to further our understanding of the rotational motion of molecules in solution. These model systems have shown that planar fluorophores are capable of rotating in-plane in less than 500 femtoseconds with very little solvent displacement. In Chapter 4, we interleaved the measurement of the lifetime decay of a fluorophore with the translational diffusion acquisition of FCS by using advanced Time Correlated Single Photon Counting (TCSPC) techniques with two-photon excitation. We used the dye Alexa 488 to benchmark our system and also measured other biologically relevant molecules. Our goal is *linkage* between ps-ns phenomena (lifetimes/rotations) and μs-ms phenomena(translational diffusion). In Chapter 5, we explored other multi-photon techniques like Coherent Anti-Stokes Raman microscopy to image NAD^+ in vesicles and water in cells using epi-detection CARS. The CARS dual laser system was

modified by inserting a vortex phase plate in one beam to create a donut shaped beam capable of stimulated emission depletion (STED). We tested the system using deep red fluorescent beads and a prototype dye capable of superresolution at lower power (STAQ).

In more detail: The capabilities of Fluorescence Correlation Spectroscopy to measure local levels for protein interactions in live cells were demonstrated in Chapter 2. Experiments provided direct, quantitative measurements of the ligand-dependent interaction between AR and one of its physiological co-activators, Tif2, in live cells using two-photon two color FCS. Specifically, 92% of total AR protein was bound to Tif2 in the presence of an agonist. When casodex, the anti cancer drug, is added, binding drops to 51%.

We have also shown that two photon FCS is capable of measuring very low concentrations (nM) in living cells. Using FCS we have been able to measure concentrations as low as 10 nM of eGFP labeled c-myc protein in live cells and follow concentration changes after serum induction. Such data showed that an immobile fraction is present (probably chromatin bound) at the level of a few nanomolar. From these results we infer that this fraction must be an important pool in the regulation of c-myc protein. Exogenous (transfected) C-myc largely resided in a more mobile pool.

FCS has started to become an important tool in the investigation of interactions of nuclear receptors with their multiple partners in the cellular environment. We expect that this relatively new technique (that allows direct access to free and bound concentrations in any desired cellular location) will prove extremely useful especially for investigating the functional mechanisms of ligand dependent transcription factors.

To better understand the complex decays seen in fluorescence, especially the decay of naturally fluorescent amino acids, i.e. tryptophan; we have used molecular dynamics simulations to look at the rotational motion of model molecules like perylene and tetracene in n-hexadecane. In Chapter 3, our study of the librational motion of perylene in hexadecane demonstrated that there is room for molecules to rotate in plane with little displacement of the solvent. The molecular dynamics simulations agree well with perylene experimental results and provide insight into the existence of a fast "libration" term observed in up-conversion data. The correlation function obtained from MD simulations for the out-of-plane motion of perylene contains less short term libration than seen for the in-plane rotation, demonstrating that the libration seen in r(t) is predominantly an " in-plane" phenomenon.

The librational motion accounted for the 'r_o defect' seen in time resolved anisotropy of this model molecule. In contrast, for tetracene, the simulation followed the decay seen in experiments only qualitatively. The discrepancies could originate either in an apparent time offset (convolution artifact) or more likely in (previously reported)[150] vibrational coupling changes occurring during this period (i.e., planar rotation of the oscillator within the molecule). We showed with QM simulations that perylene is not subject to such S_1 oscillator relaxations.

Time Correlated Single Photon Counting (TCSPC) is a technique commonly used for the measurement of the decay lifetime(s) of a molecule, and using polarized detectors, the rotational correlation times of a molecule. FCS (measures translational diffusion and concentration) and TCSPC (measures lifetime decay and rotational correlation times) are widely used as *separate* experimental setups. Current advances in TCSPC methods allow

for the acquisition of time resolved data from picoseconds to seconds that can be used to acquire the same information obtained using either technique alone. We have demonstrated the simultaneous acquisition of the ps-ns lifetime and μs-ms translational time from a single measurement of both model and biologically relevant systems in Chapter 4. We were able to measure the population decay of Alexa 488 (τ= 4.0 ns) in water and a diffusion coefficient of ~300 μm^2/sec. Concentrations as low as 20 nM were measured. We were able to observe the lifetime decay of NADH bound to ADH, but the desired ACFs of either free NADH or the NADH bound to protein were not measurable in our current experimental assembly. We suspect NADH is such a 'weak' fluorophore (with a very small two-photon cross-section and small quantum yield) that it may deactivate, e.g. irreversibly eject an electron into solution and go dark (or be trapped in other non-fluorescing states). Further, a 6MI nucleoside analog was used in a single-stranded DNA sequences capable of forming a G-quadruplex upon addition of KCl. We were able to measure the lifetime of the DNA complex with and without salt and the diffusion coefficient of the G-quadruplex. We found, somewhat surprisingly, the long lived probe subpopulation did not link to a much more compact structure.

Further improvements in this method will strive to acquire time resolved anisotropy data. From this sort of analysis, the correlation time(s) can be extracted after some modeling. Care will need to be exercised to ensure that the correct vertical and horizontal polarizations are taken on the emission side of the microscope. Time resolved anisotropy combined with the methodology explained in Chapter 5 will allow us to directly relate a correlation time through the associated lifetime(s) with the corresponding autocorrelation function. This combination of observations may be helpful for *in vitro*

FCS where separating the correlation function of molecules that have absorbed to the cover glass surface from those still in solution has potential for developing assay techniques.

As part of the exploration of the different uses of nonlinear microscopy, we have imaged the non-fluorescent co-factor NAD^+ in vesicles and water vs. D_2O in cells using epi-CARS (E-CARS) microscopy. The almost background free signal of E-CARS could only be profitably exploited for objects sized less than the pump wavelength due to E-CARS dephasing limitations. The implementation of frequency modulation (FM-CARS) should allow forward detection with decreased background. FM-CARS would be useful in performing NAD^+ measurements in living cells after a proper calibration of the NAD^+ CARS signal *vs* concentration. CARS microscopy has matured into a widely applicable technique in biologically systems. With the recent development of Stimulated Raman Scattering[223] (SRS) microscopy that while forward, has the promise of background free imaging, the field of nonlinear microscopy is poised to show exceptional growth.
We also looked into the development of a microscope that can obtain sub-diffraction resolution by using stimulated emission depletion (STED). We used sub-diffraction red beads to test the system yielding a decrease in the FWHM of about 30%. We are currently capable of resolving 170nm beads to a FWHM resolution ~210nm, compared to 240nm FWHM for the theoretical confocal resolution and our 330nm confocal measurement. We tested a novel dye and proved that the dye is capable of laser depletion using a 777nm laser beam in a new process named STAQ (Superresolution using Transiently Activated Quenchers). This new dye should be useful in lowering the total

power (>80mW) required from the depleting beam (a main drawback for living tissue imaging in STED).

In all, we have exploited several microscopy and spectroscopy methods that take advantage of ultrafast laser technology to examine local and global mobility of macromolecules and dyes, binding between various biomolecules, and the imaging of structures beyond the diffraction limit.

Appendix A. Matlab script to compute ACF from a *.SPC file

READING BINARY FILE. EXTENSION *.SPC

```
t1=fopen('a488 100nm 36mw.spc','r');
MTC=fread(t1,1,'*ubit24','a');
VP=fread(t1,1,'*ubit1','a');
RT=fread(t1,1,'*ubit4','a');
RSV=fread(t1,1,'*ubit3','a');
adc=zeros(4000000,1);
adcw=zeros(4000000,1);
mt=zeros(4000000,1);
rts=zeros(4000000,1);
gap=zeros(4000000,1);
mtov=zeros(4000000,1);
invalid=zeros(4000000,1);
for j=1:4000000;
   adc(j)=fread(t1,1,'*ubit8','a');
   mt(j)=fread(t1,1,'*ubit17','a');
   rts(j)=fread(t1,1,'*ubit3','a');
   skip=fread(t1,1,'*ubit1','a');
   gap(j)=fread(t1,1,'*ubit1','a');
   mtov(j)=fread(t1,1,'*ubit1','a');
   invalid(j)=fread(t1,1,'*ubit1','a');
end
```

MAKING SOME BACKUPS JUST IN CASE

```
adcbak=adc;

adcw1=adc;
adcw0=adc;
adcbak=adc;
adcw1=adc;
adcw0=adc;
```

Creating histogram of the channels 1 to 256 in our case

```
x=0:1:255;
histo=hist(adcw1,x);
semilogy(x,histo,'r.')
```

Figure A1.1. Histogram created from reading datafile's microtimes.

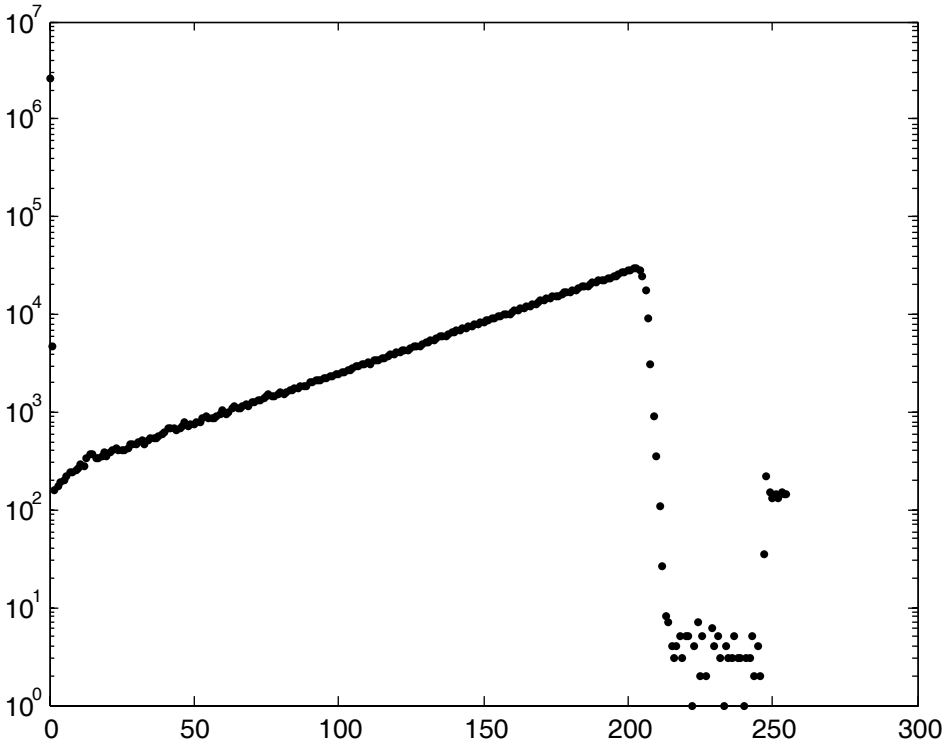

FINDING GAPS IN TIME AND DELETING BUT HONESTLY IF THERE IS ONE WHOLE FILE CAN BE WRONG

```
ndx=find(gap==1);
adcw1(ndx)=[];
adcw0(ndx)=[];
mt(ndx)=[];
rts(ndx)=[];
gap(ndx)=[];
mtov(ndx)=[];
invalid(ndx)=[];
```

PUTTING MICRO AND MACRO TIME TOGETHER

```
ptsread=length(adc);
mtovct1=0;
clear tt1;
clear tt0;
clear j;
clear mtovct1;
```

```
j=zeros(ptsread,1);
tt1=zeros(ptsread,1);
tt0=zeros(ptsread,1);
mtovct1=0;

for j=1:ptsread;
if mtov(j)==1;
mtovct1=mtovct1+1;
end
if rts(j)==1;
   tt1(j)=(255-adc(j))*(9.765625e-11)+ mt(j)*50e-9 +50e-9*131072*mtovct1;
elseif rts(j)==0;
 tt0(j)=(255-adc(j))*(9.765625e-11)+ mt(j)*50e-9 +50e-9*131072*mtovct1;
end
end
```

MORE BACKUPS

```
tt1backup=tt1;
tt0backup=tt0;
```

Separating into two routing channels
Removing those that are in channel 240 and above channels
Removing those that are in channel 50 and below

```
bph1=find(adcw1 > 239 );
tt1(bph1)=[];
adcw1(bph1)=[];

bpl1=find(adcw1 < 25);
tt1(bpl1)=[];
adcw1(bpl1)=[];

bph0=find(adcw0 >239);
tt0(bph0)=[];
adcw0(bph0)=[];

bpl0=find(adcw0 < 25);
tt0(bpl0)=[];
adcw0(bpl0)=[];
```

REMOVING THOSE BINS WITH NO PHOTON

```
ndx1=find(tt1==0);
tt1(ndx1)=[];
adcw1(ndx1)=[];
ndx0=find(tt0==0);
```

```
tt0(ndx0)=[];
adcw0(ndx0)=[];

REMOVING EXTRA length in file tt0 or tt1

filetoolong=find(tt0==tt0(end));
tt0(filetoolong)=[];
adcw0(filetoolong)=[];

filetoolong1=find(tt1==tt1(end));
tt1(filetoolong1)=[];
adcw1(filetoolong1)=[];
% plot(tt1); plot(tt0);
x=0:1:255;
histolf1=hist(adcw1,x);
semilogy(x(180:220),histolf1(180:220),'r.')
semilogy(x,histolf1,'r.')
x=0:1:255;
histolf0=hist(adcw0,x);
semilogy(x,histolf0,'r.')
```

Figure A1.2. Plot of the 'cleaned' decay.

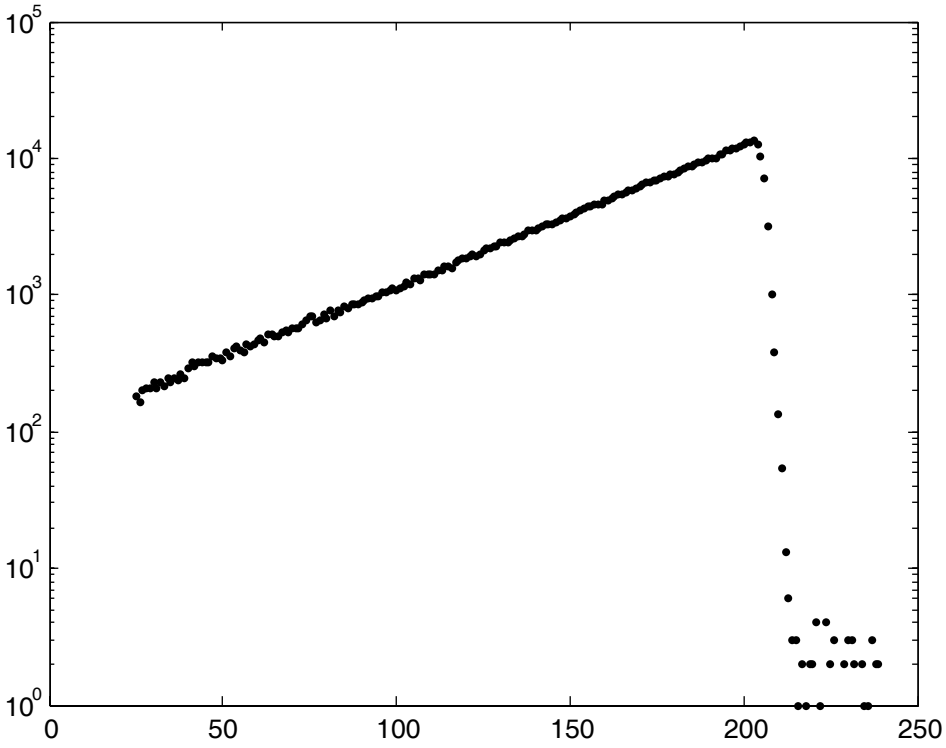

ADDING FILTER HERE

```
lb=25
ub=201
posf=1
nesf=1
ff=0;
for ff=1:length(tt1);
   if (adcw1(ff) >=lb) && (adcw1(ff) <=ub);
      tt1(ff)=posf*tt1(ff);
   elseif (adcw1(ff)>ub) ||( adcw1(ff) <lb)
      tt1(ff)=nesf*tt1(ff);
   end
end
ff=0;
for ff=1:length(tt0);
   if (adcw0(ff)>=lb) && ( adcw0(ff) <=ub);
      tt0(ff)=posf*tt0(ff);
   elseif (adcw0(ff)>ub) ||( adcw0(ff)<lb);
      tt0(ff)=nesf*tt0(ff);
   end
end
```

Autocorrelation Function Computation

Clearing variables

```
max1=max(tt1)-abs(tt1(1))
max0=max(tt0)-abs(tt0(1))
clear Gdelta1;
clear j;
clear m;
clear k;
clear i;
nsect=0;
clear tt1b;clear tt0b;
samprate=1E-5    THIS IS THE DESIRED SAMPLING RATE
ptssections=15;    POINTS PER SECTION
Numsections=6;   NUMBERS OF SECTION
basetau=4;          BASE TAU
Gdelta1=zeros(50,Numsections*ptssections);
test=[1 2 3 4 5 6 7 8 9 10 11 12 13 14 15];
transpose(test);
for nsect=1:Numsections;
  numbin1= (max1/(samprate*basetau^(nsect-1)));
  numbin0= (max0/(samprate*basetau^(nsect-1)));
  if numbin1 >=numbin0;
```

```
    Mtot=floor(numbin0/50)
  elseif numbin1<numbin0;
  Mtot= floor(numbin1/50)
end
  numbin1=int32(numbin1);
  numbin0=int32(numbin0);
  tt1b=zeros(numbin1,1);
  tt0b=zeros(numbin0,1);
  [tt1b]=hist(tt1,double(numbin1));
  [tt0b]=hist(tt0,double(numbin0));
  j=zeros(Mtot,1);
  m=zeros(Mtot,1);
  i=zeros(Mtot,1);
  k=0  ;
    nsect

for k=1:50;

    j=(nsect-1)*ptssections;
  for m=test(1):test(end);
     j=j+1;
     loweri=1+Mtot*(k-1);
     upperi=Mtot*(k)-m;
     sum10=0;
     sum01=0;
     mean1=mean(tt1b(loweri:upperi));
     mean0=mean(tt0b(loweri:upperi));
   i=zeros(Mtot-1,1);
for i=loweri:upperi;
    %mean1=mean(tt1b(1:upperi));
    sum10=(tt1b(i)-mean1)*(tt0b(i+m)-mean0)+sum10;
    sum01=(tt0b(i)-mean0)*(tt1b(i+m)-mean1)+sum01;
end

  Gdelta1(k,j)=0.5*(sum10+sum01)/(mean1*mean0*(Mtot-m));
end
end
end
```

Another backup

```
Gbackup=Gdelta1;
```

REMOVING THOSE POINTS THAT REPEAT THEMSELVES

```
jj=0;
nn=0;
```

```
time1=0;
Gmean=0;
for jj=1:Numsections;

  for nn=1:ptssections;

    if jj>1 && nn*basetau^(jj-1) < time1(ptssections*(jj-1)); %FLAGGING
DUPLICATES WITH -1
    time1(ptssections*(jj-1)+nn)=-1;
    else
    time1(ptssections*(jj-1)+nn)=nn*basetau^(jj-1);
    end

  end

end

remdup=find(time1==-1);
time1(remdup)=[];
Gdelta1(:,remdup)=[];
Gmean=mean(Gdelta1);
Gstd=std(Gdelta1);
semilogx(time1,Gmean,'b.-')
```

Figure A1.3 Plot of the calculated autocorrelation function

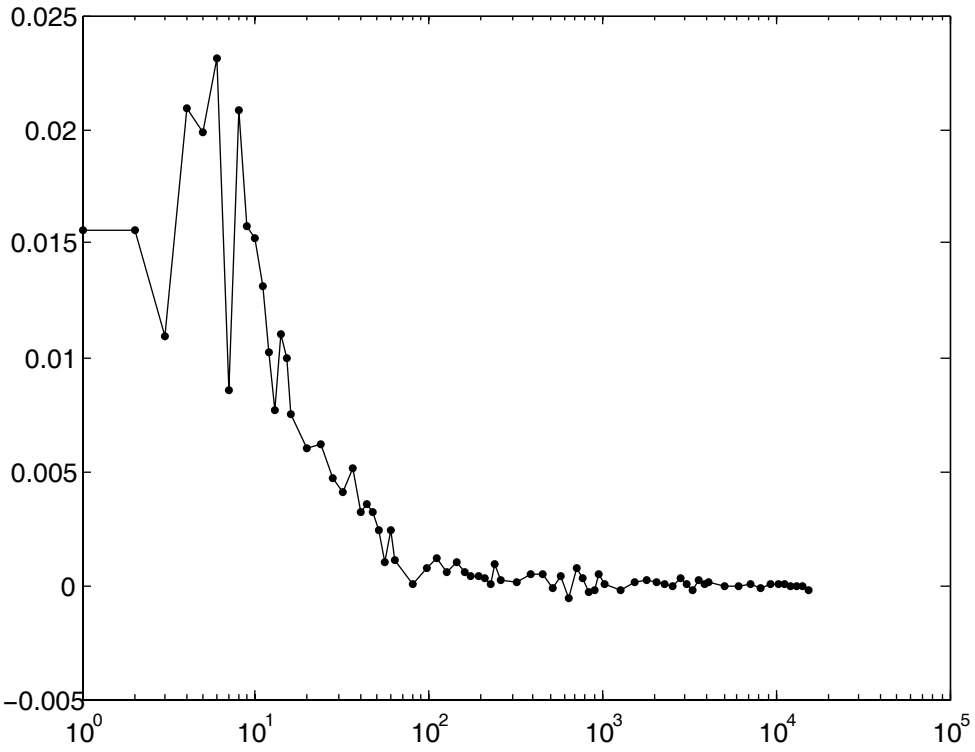

Appendix B

This manuscript was published in its entirety in 2008[62]

A Graphical User Interface for BIOEQS: A Program for Simulating and Analyzing Complex Bio-molecular Interactions.

Tilman Rosales[1] and Catherine A. Royer[2]

[1] Laboratory of Biophysical Chemistry, Optical Spectroscopy Section, NHLBI, NIH Bethesda MD 20892 and [2] Inserm, U554, Montpellier, France

ABSTRACT

BIOEQS is a global analysis and simulations program for complex biomolecular interaction data developed in the 1990's[224,225]. Its continued usefulness derives from the fact that it is based on a numerical solver for complex coupled biological equilibria, rather than on closed-form analytical equations for the binding isotherms. It is therefore quite versatile, allowing easy testing of multiple binding models and analysis of systems too complex for closed form solutions. However, a major drawback to a generalized use of this program has been the lack of a graphical user interface (GUI) for setting up the binding models and experimental conditions, as well as visualizing the results. We present here a new GUI for BIOEQS that should be useful in both research and teaching applications.

Simulation and analysis of complex biomolecular binding equilibria are key elements to both the design of binding experiments and the interpretation of interaction data. Moreover, these approaches are covered in many graduate and undergraduate courses in biochemistry and biophysics. BIOEQS is a relatively powerful, numerically based program designed to simulate and globally analyze such complex data sets.[224,225] Rather than solving a closed form, analytical expression for the binding isotherm, the BIOEQS solver uses a numerical constrained optimization algorithm, with the mass balance constraints incorporated as Lagrange multipliers, to solve the set of non-linear equations for the free energies of formation of each species, in terms of the species concentration vector. This solver is called at each point of the binding isotherm to calculate the isotherm based on the input free energy and observable asymptotic parameters. To obtain best fit free energy and other parameters, the fitting routine is based on a non-linear Marquardt-Levenberg algorithm. The program was originally conceived to treat a very broad range of binding experiments, in terms of number of elements, number of species, observable parameters and thermodynamic variables including temperature, pressure or chemical potential.

The advantage of the GUI described here resides in the ready accessibility of many of the available options of BIOEQS. These can be modified quickly with the corresponding results examined at a faster pace and with little knowledge of the intricacies of the subroutines. BIOEQS functions using ASCII format I/O files (2 input and 4 output), the structures of which have been preserved for compatibility and for advanced users. However, in the GUI, the user no longer needs to modify these files directly.

We describe here the basic structure of the graphical user interface (GUI) designed for BIOEQS by following the necessary steps from model making to confidence limit interval

analysis. Here, we have simulated data for a binding model including six species, a DNA-protein interaction with stoichiometries from one to four proteins. The other two species are the free DNA and the free protein. These simulated data were analyzed globally to demonstrate the GUI analysis output.

The BIOEQS GUI is divided into four pages or tabs; a model, an experiment, a fitting parameters and a results page. The program initializes in the model page (Figure A2.1a) where the first step is to create the **model** containing all the information necessary for composition of each species including stoichiometry and number of site isomers. (A quantum yield factor allows for assignment of unequal weighting of the species in the observable). A model making tool (Figure A2.1b) allows for creating species by dragging and dropping elements into species boxes that can also be dragged and placed within a specific free energy range. The model can also be built manually. The BIOEQS program has a limit of three different elements and the GUI has a limit of fifteen unique species (100 for the kernel). Drop down menus allow the user to specify the concentration range and the number of experiments (maximum 16). The default solver of the GUI is the numerical one mentioned above, but a closed-form analytical solver for monomeric protein folding can also be specified. If a simulation is performed, a seed for the noise and percent noise become available options.

The next two pages involve specifying the experimental and fitting parameters. The available options depend on the type of experiment. For each experiment, the user must specify what type of observable is to be mapped (i.e. total or fractional contribution to the total signal for a particular element, or the population of a specific species) and the actual experiment type

Figure A2.1. a) The **Model** page is shown with six species (including the identity matrix) with the Model Making Tool in (b) showing the four species containing DNA and protein elements with color coded icons.

A)

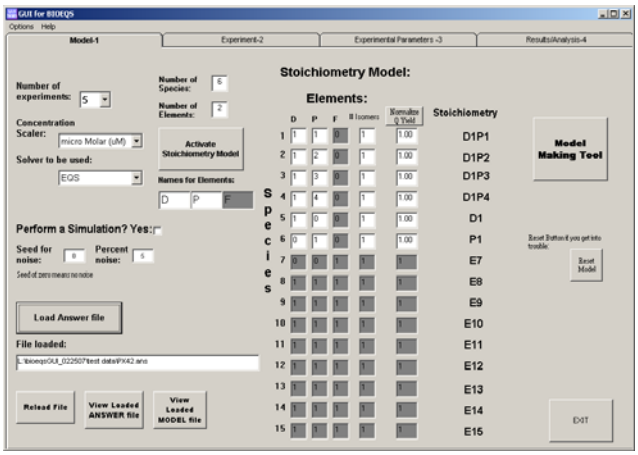

B)

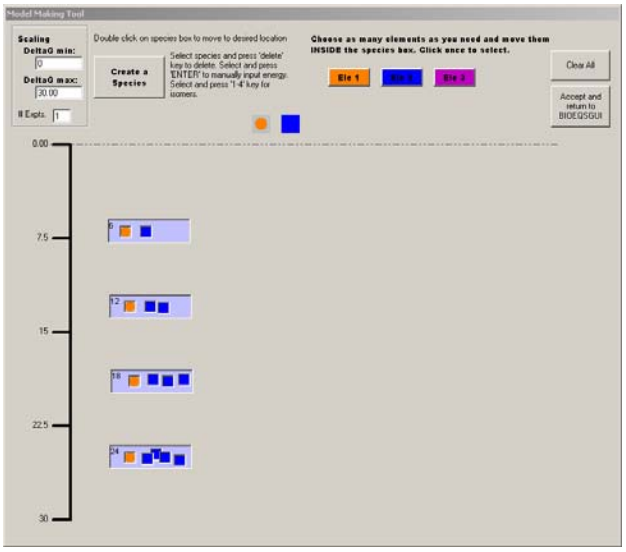

performed, i.e. titration, folding, pressure or temperature. Also, depending on the type of the experiment, the concentration for the other elements, the concentration of chemical additive

(denaturant, salt, osmolyte), the pressure or the temperature of the experiment may be required. In our example, for all the experiments, we chose a fractional population (with respect to total DNA) for each of the species containing DNA (species 1-5). The experiment type was a titration of the first element (DNA) at 0.1 μM with protein at a temperature of 291 K and at a pressure of 1 bar. If a simulation is performed, the simulated data files are also created on this page. We created five files starting at 0.1 and ending at 1000 μM with a step of log 0.1 units, each file corresponding to the fractional population of each of the DNA containing species.

The fitting parameters (free energies of formation (from the free elements) for each of the species, asymptotic observable values, and thermodynamic parameters such as m-values, volume changes or enthalpy changes) are found in the Master Table on the Experimental Parameters page (page 3). Because BIOEQS is a global analysis program, the GUI includes algorithms to deduce the appropriate parameter numbering scheme, and thus linking of the different parameters energies across experiments is also done on this table. For our example, the energies were linked across all five experiments and allowed to vary. The initial guesses for the species were 6, 12, 18 and 24 kcal/mol. The asymptotic values of fractional populations were normalized between 0 and 1, but for real experiments they can in fact be any number resulting from an experimental observable.

The BIOEQS FORTRAN 77 code has been re-compiled as a dynamic link library (DLL) that is called directly with all the parameters (There is no longer a need to run the program in a MS-DOS window). The use of a DLL allows for multiple instances and sequential calls to the DLL, as when performing a covariance analysis (see below). The output, including any errors produced by the DLL, are displayed as the calculation progresses in textboxes located next to the Master Table in the Experiment parameters page.

Figure A2.2. a) The **Results** page with the graphed results with residuals in (b) and the covariance analysis (c) of the first element of experiment #1.

A)

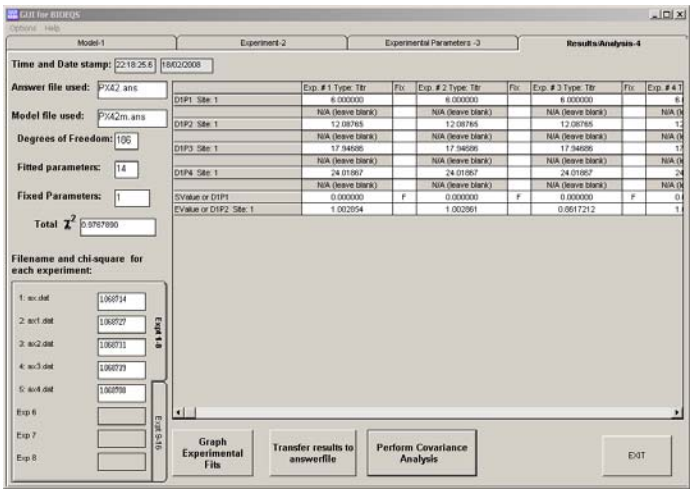

B)

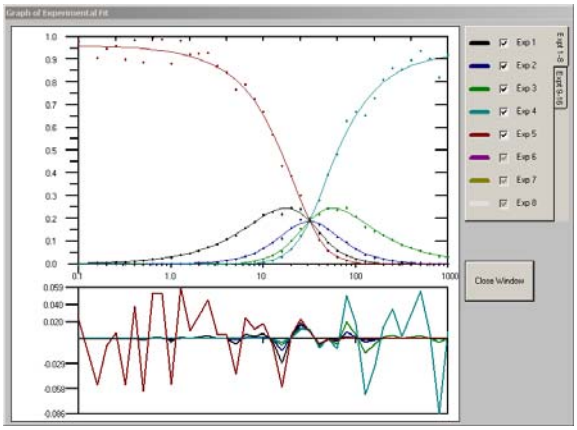

C)

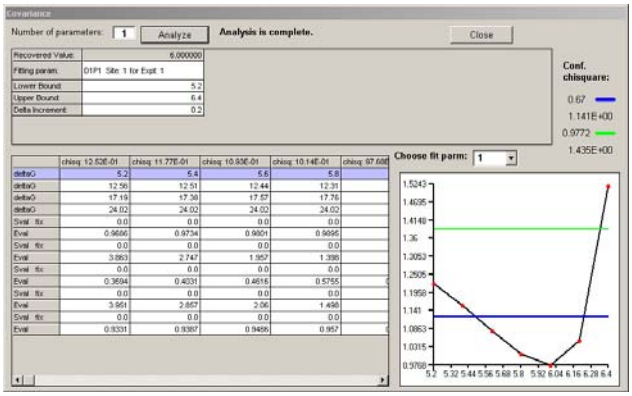

The **Results** page displays in table format all the returned parameter values for each experiment as well as the local and global χ^2 values (Figure A2.2a). Another useful aspect of the BIOEQS GUI is the rapid graphic display of the fit results (Figure A2.2b), including residuals for all the experiments. The recovered parameter values are stored in an ASCII file with a *.res extension

and the initial data, fit and residuals for each experiment are placed in a file with the *.tmp extension.

Rigorous confidence limit testing and covariance analysis can be also performed for up to 20 unique parameters over a specified interval in specified steps. The output table includes the **cov**ariance of all the parameters for each experiment due to the change of the specified parameter. The calculated χ^2 for that step is used as a header on each column. Also, a graph of χ^2 vs parameter (**con**fidence limit) is plotted for each variable including a line at the 67% and 97% interval (Figure A2.2c). In our example, we chose the first free energy of the first experiment to be rigorously tested between 5.2 to 6.4 kcal/mol with steps of 0.2 kcal/mol. For rapid recognition, the selected variable is shown in purple in the Covariance Table. The results are placed in files with a *.cov and a *.con extension.

Given the broad capabilities of the BIOEQS fitting program, we hope that the development of the GUI will allow the program to be widely used. In particular, it could be a very useful tool in upper level undergraduate or graduate courses that cover biomolecular interactions. The program with the installation package and a brief description of the I/O files can be found at the following link: http://abcis.cbs.cnrs.fr/BIOEQS/.

Appendix C. Release of Fluorescein labeled ssDNA from AuNP-DNA complex by laser local heating.

Introduction

We were aware of the enormous effective extinction of gold nanoparticles[226] and we had previously used it to cause FRET quenching over great distances.[227] We reasoned that the large cross section would cause nanoparticles to transiently heat upon laser illumination, and then cool by conduction into surrounding liquid water. If the thermal rise topped 100C, we hoped a vapor barrier might form that would slow conduction and allow the NP to stay hot even longer.[228,229] DNA melting and dissociation of strands is *estimated* to require at least tens of μs, and water heat conduction should cool a 60 nm particle in tens of ns.[230] Nevertheless, we felt the combination of the largest particles we could stabilize and a high concentration >20μM of unlabeled complementary strand might make this "hot flash" phenomenon useful for rapid PCR reactions or other DNA-melting diagnostics

Materials and Methods

A ssDNA having 20 bases long was synthesized with trebler sulfhydryl groups from Trilink, Inc on the 5' end. A complementary sequence to this oligonucleotide with a 3'FAM was also obtained from Trilink Inc. The ssDNAs were mixed at equimolar concentrations and annealed at 95 ºC for 5 minutes in 1M DTT and 2M NaCl buffer. The solution was stored until use at -80 ºC. For the reaction with Au (50nm dia. from Ted Pella Inc), a similar procedure to that of Schatz *et al.*[231] was used. The DNA solution was

passed through a NAP-10 column (Invitrogen) to remove any DTT. The Au-DNA solution was mixed for two days during which the NaCl was adjusted to 25 or 50mM. The unreacted solution was separated from the Au-DNA by centrifugation. The solution was washed three times with 50mM NaCl and centrifuged at 5000 rpm for 30 minutes. The fluorescein absorption was measured using a HP-8452 diode array UV/VIS spectrometer.

The fluorimeter used in all the experiments was an Yvon Horiba Fluoromax 211 with slits set to 5nm in both the emission and excitation windows. The excitation was set to 470 nm and the emission was taken from 485 to 700nm. The excitation polarizer was set to 90 degrees (horizontal) and the emission polarizer was removed from the path. A 500SP filter was placed on the excitation side. Both the Signal and the Reference were acquired. The S/R resulting signal was used for all the experiments. The background arising from the buffer only was substracted from all the spectra.

The fluorescence of a sample containing 20μL of Au-DNA, 100 μL of 25 or 50mM NaCl buffer and 3μL of complementary DNA (20μM) was used as a control. The positive control was made with 20μL of Au-DNA and 3μL of complementary DNA. This sample was heated for 5 minutes at 95 C. 103 μL of buffer was added after the sample was allowed to cool (~2mins). All of the 'laser' samples were prepared as the control samples and placed in capillary tubes. The capillary tubes were placed in the path of a TFR laser (Spectra Physics) capable of producing 5 ns pulses with 100μJ of power at 524 nm.

Transmission Electron Microscopy images were taken using the electron microscope at the Electron microscopy Core facility of NHLBI. The samples were dried on a copper

grid (200 mesh) that had carbon films deposited on them as support using a Denton Benchtop Turbo vacuum evaporator. The samples were allowed to dry on the copper grids and stained with a with 1-2% uranium acetate to work as a positive contrast agent. A JEOL 1200EX transmission electron microscope with an AMT 6 megapixel digital camera was used to image the 50nm Au-DNA nanoparticles.

Results and discussion

Figure A3.1 has the release of fluorescence by positive and negative controls for a typical run. Addition of NaCl to make 1M [Na+Cl-] produced very little release of the fluorescein labeled DNA. The 1M NaCl sample was left overnight and the fluorescence taken as described earlier. The control with 25mM NaCl with no complementary DNA had no release of fluorescein labeled DNA.

Figure A3.2 shows the release due to the addition of DNAase enzyme to a control solution. The release of the fluorescein labeled DNA is as good as that for a positive (bulk heated) control. Note that the solution became clear indicating loss of colloidal suspension. (There was a black precipitate clinging to the microcentrifuge tube). Other controls that involve adding just the buffer with no DNAase produced no release. These negative controls included adding 1μL of EDTA at 0.5M. There was no release seen using these controls.

Figure A3.1. Release of the fluorescein labeled DNA by heating for 5 minutes at 95 ºC the Au-DNA complex. The control was not heated and addition of 1M NaCl has minimal release of fluorescein.

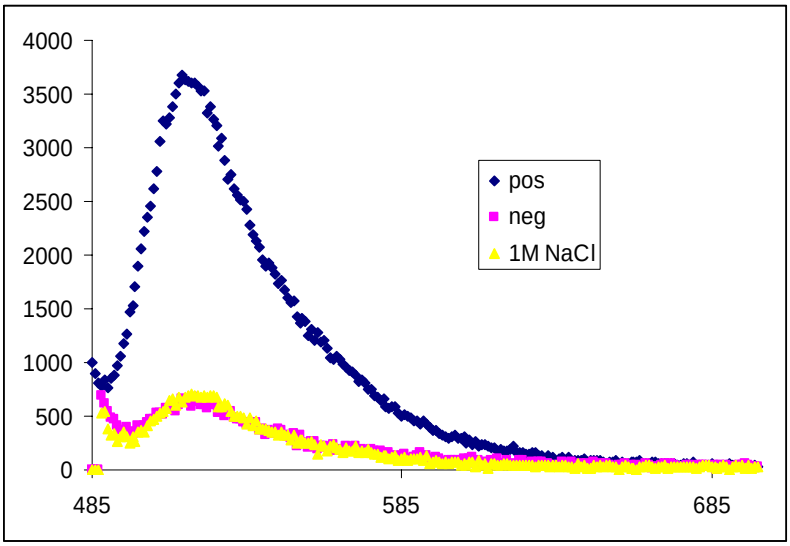

Figure A3.2. Release of the fluorescein labeled DNA by DNAase. A negative and positive control are shown.

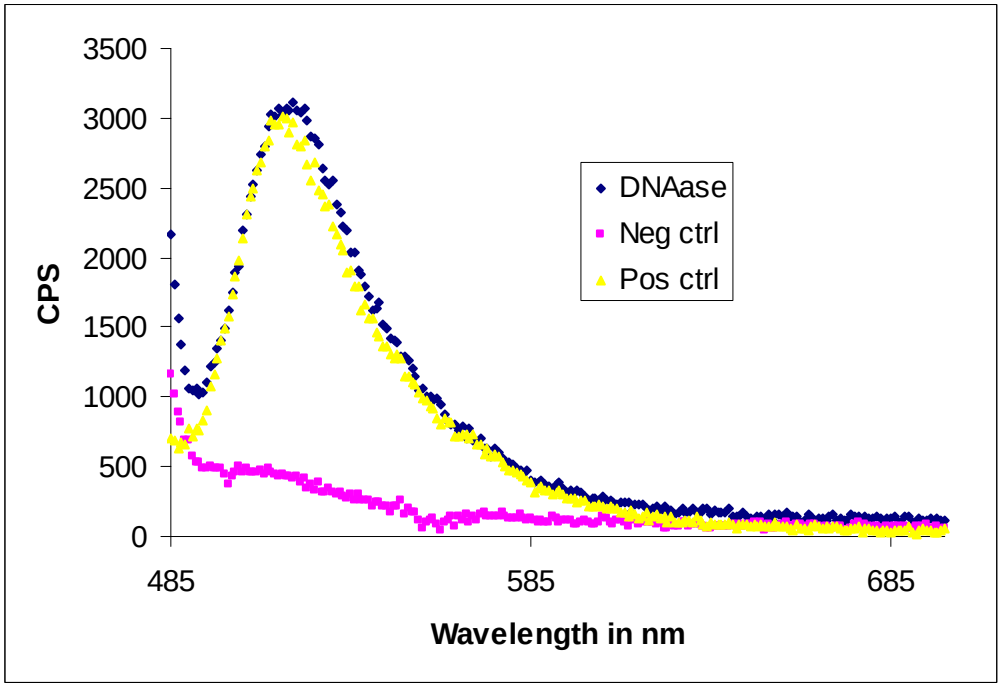

The laser experiments are shown in Figure A3.3. The laser pulse rates and the total exposure time to a laser were varied. The minimum rate was 300Hz and the maximum was 1200Hz. The maximum release achieved using 1200Hz was 16% taken from the maximum fluorescence released by the positive control. To prove that the DNA is bound to the gold particles, we have imaged the Au-DNA using TEM. Figure A3.4 shows the EM images of a Au-DNA solution.

Figure A3.3. Laser experiment showing release of the fluorescein labeled ssDNA depending on total amount of time and repetition rate.

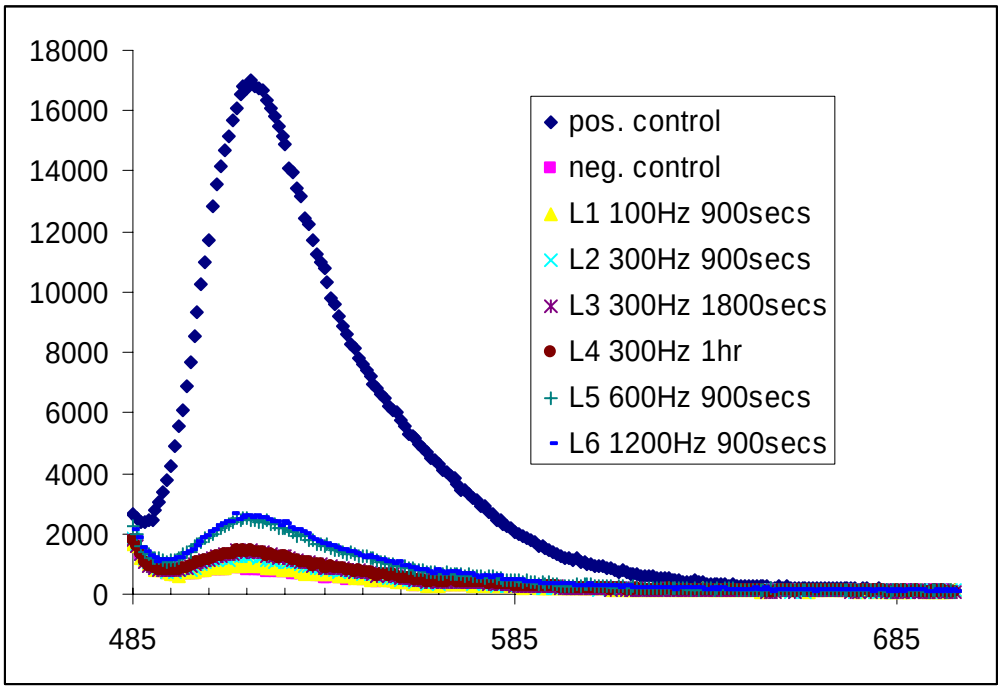

Figure A3.4. TEM image of Au-DNA. Close-up showing the DNA (some positive staining). Note that the DNA has collapsed in the EM images.

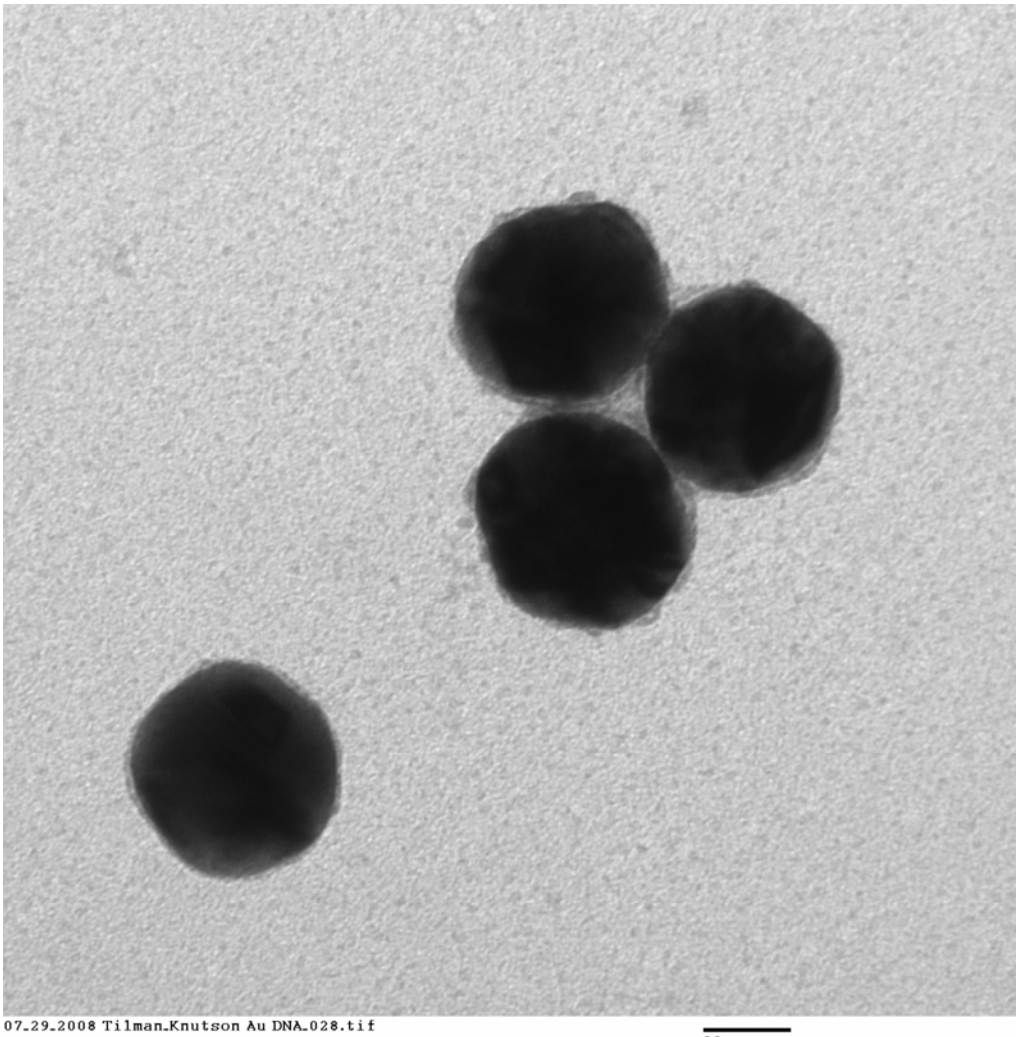

We have shown that there is a power and time dependent release of fluorescein labeled ssDNA from the Au-DNA complex due to laser excitation. Surprisingly, we have achieved photothermal melting and dissociation of labeled DNA strands from their anchored complement on nanoparticles. It is possible that the creation of the vapor bubble

might be changing the morphology of the nanoparticles. But we don't believe we are melting the nanoparticles since the intensity we used of 280 kW/cm^2 is below the intensity[229] required to melt nanoparticles of such size $700kW/cm^2$. Checks to interrogate the possibility of nanoparticle morphology changes or Au-thiol bond breakage[232] are necessary.

Bibliography and Notes

1 Gest, H., Notes Rec. R. Soc. Lond. **58** (2), 187 (2004).

2 Hooke, R., *Micrographia*, Dover Phoenix Editions ed. (Dover Publications, Dover, 2003).

3 Smit, P. and Heniger, J., Antonie van Leeuwenhoek **41** (3), 219 (1975).

4 Lakowicz, J. R., in *Principles of Fluorescence Spectroscopy* (Kluwer Academic/Plenum Publishers, New York, 1999).

5 Sambrook, J. and Russell, D. W., *Molecular Cloning: A laboratory Manual*. (Cold Spring Harbor Laboratory Press, Cold Spring Harbor, NY, 2001).

6 Chalfie, M., Tu, Y., Euskirchen, G., Ward, W., and Prasher, D., Science **263** (5148), 802 (1994).

7 Shaner, N. C., Campbell, R. E., Steinbach, P. A., Giepmans, B. N., Palmer, A. E., and Tsien, R. Y., Nat Biotechnol **22** (12), 1567 (2004).

8 Boyd, R. W., *Nonlinear Optics*. (Academic Press, Burlington,MA, 2008).

9 Alberts, B., Johnson, A., Lewis, J., Raff, M., Roberts, K., and Walter, P., *Molecular Biology of the Cell*, 4th ed. (Garland Science, New York,NY, 2002).

10 Gratton, E. and vandeVen, M. J., in *Handbook of Biological Confocal Microscopy*, edited by J. B. Pawley (Plenum Press, New York, 1989).

11 McQuarrie, D. A., *Statistical Mechanics*. (University Science Books, Sausalito, 2000).

12 Smekal, A., Die Naturwissenschaften **43**, 873 (1923).

13 Raman, C. V. and Krishnan, K. S., Nature (London) **12**, 501 (1928).

14 Potma, E. O. and Xie, X. S., in *Handbook of Biomedical Nonlinear Optical Microscopy*, edited by B. R. Masters and P. T. C. So (Oxford University Press, New York, 2008).

15 Goppert-Meyer, M., Ann. Phys. **9**, 273 (1931).

16 Masters, B. R. and So, P. T. C., Micr. Res. and Tech. **63**, 3 (2004).

17 Maiman, T. H., Nature **187**, 493 (1960).

18 Kaiser, W. and C.G.B, G., Phys. Rev. Lett. **7**, 229 (1961).

19 Sheppard, C. J. R. and Kompfner, R., Appl. Optics **17**, 2879 (1978).

20 Sheppard, C. J. R., Kompfner, R., Gannaway, J. N., and Walsh, D., presented at the IEEE/OSA Conf. Laser Eng. Appl., Washington, DC, 1977 (unpublished).

21 Gannaway, J. N. and Sheppard, C. J. R., Opt. Quant. Electron. **10**, 435 (1978).

22 Spence, D. E., Kean, P. N., and Sibbert, W., Opt. Lett. **16**, 42 (1991).

23 Pawley, J. B., *Handbook of Biological Confocal Microscopy*. (1995).

24 Xu, C. and Webb, W. W., in *Topics in Fluorescence Spectroscopy*, edited by J. R. Lakowicz (1997), pp. 471.

25 Denk, W., Strickler, J. H., and Webb, W. W., Science **248** (4951), 73 (1990).

26 Zipfel, W. R., M., W. R., and W., W. W., Nat. Biotechnol **21** (11), 1368 (2003).

27 Bacia, K., Scherfeld, D., Kahya, N., and Schwille, P., Biophys. J. **87** (2), 1034 (2004).

28 Wang, Z. F., Shah, J. V., Chen , Z. P., Sun, C. H., and Berns, M. W., J. Biomed. Opt. **9** (2), 395 (2004).

29 Bacia, K., Majoul Irina, V., and Schwille, P., Biophys. J. **83** (2), 1184 (2002).

30 Chen, Y., Muller, J. D., Tetin, S. Y., Tyner, J. D., and Gratton, E., Biophys. J. **79** (2), 1074 (2000).

31 Sherman, E., Itkin, A., Kuttner, Y. Y., Rhoades, E., Amir, D., Haas, E., and Haran, G., Biophys. J. **94** (12), 4819 (2008).

32 Hazlett, T. L., Ruan, Q., and Tetin, S. Y., in *Methods. Mol. Biol.* (2005), Vol. 305, pp. 415.

33 Torres, T. and Levitus, M., J Phys Chem B **111** (25), 7392 (2007).

34 Wiseman, P. W., Squier, J. A., Ellisman, M. H., and Wilson, K. R., J. Microsc.-Oxf **200**, 14 (2000).

35 Digman, M. A., Wiseman, P. W., Choi, C., Horwitz, A. R., and Gratton, E., Proc. Natl. Acad. Sci. U. S. A. **106** (7), 2170 (2009).

36 Huang, D. Z.-L., (http://belfield.cos.ucf.edu/one%20vs%20two-photon%20excitation.html).

37 Tolles, W., Nibler, J., Mcdonald, J., and Harvey, A. B., Appl. Spectrosc. **31** (4), 253 (1977).

38 Maker, P. D. and Terhune, R. W., Phys. Rev. **137** (3A), A801 (1965).

39 Zumbusch, A., R., H. G., and S., X. X., Phys. Rev. Lett. **82** (20), 4142 (1999).

40 Evans, C. L., Y., X. X., S., K., S., X. X., C., W. S. T., and S., Y. G., Opt. Express **15** (19), 12076 (2007).

41 Cheng, J. X., Pautot, S., Weitz, D. A., and Xie, X. S., Proc. Natl. Acad. Sci. U. S. A. **100** (17), 9826 (2003).

42 Hellerer, T., Schiller, A., Jung, G., and Zumbusch, A., ChemPhysChem **7**, 630 (2002).

43 Cheng, J. X., Potma, E. O., and Xie, X. S., J. Phys.Chem. A **106**, 8561 (2002).

44 Ly, S., G., M., S., F., J., C., and T., H., Opt. Express **15** (25), 16839 (2007).

45 Wright, A. J., P., P. S., M., G. J., W., F. C., L., E. C., and S., X. X., Opt. Exp. **15** (26), 18209 (2007).

46 Hell, S. W. and Wichmann, J., Opt. Lett. **19** (11), 780 (1994).

47 Moh, K. J., Yuan, X. C., Bu, J., Burge, R. E., and Gao, B. Z., Appl. Optics **46** (30), 7544 (2007).

48 Meyer, L., Wildanger, D., Medda, R., Punge, A., Rizzoli, S. O., Donnert, G., and Hell, S. W., Small **4** (8), 1095 (2008).

49 Eggeling, C., Ringemann, C., Medda, R., Schwarzmann, G., Sandhoff, K., Polyakova, S., Belov, V. N., Hein, B., von Middendorff, C., Schonle, A., and Hell, S. W., Nature **457** (7233), 1159 (2009).

50 Willig, K. I., Keller, J., Bossi, M., and Hell, S. W., New J. Phys. **8** (2006).

51 Rodriguez, L. G., Lockett , S. J., and Holtom, G. R., Cytom. Part A **69A** (8), 779 (2006).

52 Nelson, P., *Biological Physics*. (W. H. Freeman, 2003).

53 Kim, S., *Microhydrodynamics: principles and selected applications*. (1991).

54 Einstein, A., in *Investigations on the theory of the Brownian Movement*, edited by R. Furth (Dover Publications, New York, 1956).

55 Einstein, A., Annalen der Physik **17**, 549 (1905).

56 Perrin, F., J. Phys. Rad., 497 (1934).

57 Tanford, C., *Physical Chemistry of Macromolecules*. (Wiley and Sons Inc, New York, 1963).

58 Elson, E. L. and Magde, D., Biopolymers **13** (1), 361 (1974).

59 Rosales, T., Georget, V., Malide, D., Smirnov, A., Xu, J. H., Combs, C., Knutson, J. R., Nicolas, J. C., and Royer, C. A., Eur. Biophys. J. Biophys. Lett. **36** (2), 153 (2007).

60 Xu, J., Shen, X., and Knutson, J. R., J. Phys. Chem. A **107** (41), 8383 (2003).

61 Rosales, T., Xu, J. H., Wu, X. W., Hodoseck , M., Callis, P., Brooks, B. R., and Knutson, J. R., J. Phys. Chem. A **112** (25), 5593 (2008).

62 Rosales, T. and Royer, C. A., Anal. Biochem. **381** (2), 270 (2008).

63 Magde, D., Webb, W., and Elson, E., Phys. Rev. Lett. **29** (11), 705 (1972).

64 Berne, B. and Pecora, R., *Dynamic Light Scattering: with applications to Chemistry, Biology and Physics*. (Wiley-Interscience, New York, 1976).

65 Haustein, E. and Schwille, P., Curr. Opin. Struct. Biol. **14** (5), 531 (2004).

66 Bacia, K., Kim, S. A., and Schwille, P., Nat. Methods **3** (2), 83 (2006).

67 Atkins, P. W. and Friedman, R. S., *Molecular Quantum Mechanics*. (Oxford University Press, New York, 1997).

68 Masters, B. R. and So, P. T. C., in *Handbook of Biomedical Nonlinear Optical Microscopy*, edited by B. R. Masters and P. T. C. So (Oxford University Press, New York, 2008).

69 Pabit, S. and Berland, K., in *Handbook of Biomedical Nonlinear Optical Microscopy*, edited by B. R. Masters and P. T. C. So (Oxford University Press, New York, 2008).

70 Nagy, A., Wu, J. R., and Berland, K. M., Biophys. J. **89** (3), 2077 (2005).

71 Elson, E. and Magde, D., Biopolymers **13** (1), 1 (1974).

72 Magde, D., Webb, W. W., and Elson, E., Phys. Rev. Lett. **29** (11), 705 (1972).

73 Kettling, U., Koltermann, A., Schwille, P., and Eigen, M., Proc. Natl. Acad. Sci U. S. A. **95** (4), 1416 (1998).

74 Heinze, K. G., Koltermann, A., and Schwille, P., Proc. Natl. Acad. Sci. U. S. A. **97** (19), 10377 (2000).

75 Kim, S. A., Heinze, K. G., Waxham, M. N., and Schwille, P., Proc. Natl .Acad. Sci. U.S. A. **101** (1), 105 (2004).

76 Hillesheim, L. N. and Muller, J. D., Biophys. J. **85** (3), 1948 (2003).

77 Chen, Y., Wei, L. N., and Muller, J. D., Biophys. J. **88** (6), 4366 (2005).

78 Berland, K. and Shen, G. Q., Appl. Optics **42** (27), 5566 (2003).

79 Karvonen, U., Janne, O. A., and Palvimo, J. J., FEBS Lett. **523** (1-3), 43 (2002).

80 Nettles, K. W. and Greene, G. L., Annu. Rev. Physiol. **67**, 309 (2005).

81 Chang, C. S., Chen, Y. T., Yeh, S. D., Xu, Q. Q., Wang, R. S., Guillou, F., Lardy, H., and Yeh, S. Y., Proc. Natl. Acad. Sci. U. S. A. **101** (18), 6876 (2004).

82 De Gendt, K., Swinnen, J. V., Saunders, P. T. K., Schoonjans, L., Dewerchin, M., Devos, A., Tan, K., Atanassova, N., Claessens, F., Lecureuil, C., Heyn, s. W., Carmeliet, P., Guillou, F., Sharpe, R. M., and Verhoeven, G., Proc. Natl. Acad. Sci. U. S. A. **101** (5), 1327 (2004).

83 Culig, Z., Comuzzi, B., Steiner, H., Bartsch, G., and Hobisch, A., J. Steroid. Biochem. Mol. Biol. **92** (4), 265 (2004).

84 Burnstein, K. L., J. Cell. Biochem. **95** (4), 657 (2005).

85 Edwards, J. and Bartlett, J. M. S., B.J.U. Int. **95** (9), 1320 (2005).

86 Edwards, J. and Bartlett, J. M. S., B.J.U. Int. **95** (9), 1327 (2005).

87 d'Ancona, F. C. H. and Debruyne, F. M. J., Hum. Reprod. Update **11** (3), 309 (2005).

88 Lonard, D. M. and O'Malley, B. W., Trends Biochem. Sci. **30** (3), 126 (2005).

89 Xu, J. M. L. Q. T., Mo.l Endocrinol. **17** (9), 1681 (2003).

90 Smith, C. L. and O'Malley, B. W., Endocr. Rev. **25** (1), 45 (2004).

91 Wu, R. C., L., S. C., and O'Malley, B. W., Endocr. Rev. **26** (3), 393 (2005).

92 Ye, X. C., Han, S. J., Tsai, S. Y., DeMayo, F. J., Xu, J. M., Tsa, i. M. J., and O'Malley, B. W., Proc. Natl. Acad. Sci. U. S. A. **102** (27), 9487 (2005).

93 Greschik Holger Moras, D., Curr Top Med Chem **3** (14), 1573 (2003).

94 Nagy, L. and Schwabe, J. W. R., Trends. Biochem. Sci. **29** (6), 317 (2004).

95 Baudendistel, N., Muller, G., Waldeck, W., Angel, P., and Langowski, J., ChemPhysChem **6** (5), 984 (2005).

96 Kim, S. A., Heinze, K. G., Bacia, K., Waxham, M. N., and Schwille, P., Biophys. J. **88** (6), 4319 (2005).

97 Larson, D. R. , Gosse, J. A., Holowka, D. A., Baird , B. A., and Webb, W. W., J. Cell. Biol. **171** (3), 527 (2005).

98 Saito, K., Wada, I., Tamura, M., and Kinjo, M., Biochem. Biophys. Res. Commun. **324** (2), 849 (2004).

99 Thews, E., Gerken, M., Eckert, R., Zapfel, J., Tietz, C., and Wrachtrup, J., Biophys. J. **89** (3), 2069 (2005).

100 Chen, Y., Muller , J. D., So, P. T. C., and Gratton, E., Biophys. J. **77** (1), 553 (1999).

101 Chen, Y., Wei, L. N., and Muller, J. D., Proc. Natl. Acad. Sc.i U. S. A. **100** (26), 15492 (2003).

102 Black, B. E. and Paschal, B. M., Trends Endocrinol. Metab. **15** (9), 411 (2004).

103 Whitaker, H. C., Hanrahan, S., Totty, N., Gamble, S. C., Waxman, J., Cato, A. C. B., Hurst, H. C., and Bevan, C. L., Clin. Cancer Res. **10** (21), 7392 (2004).

104 Georget, V., Lobaccaro, J. M., Terouanne, B., Mangeat, P., Nicolas, J. C., and Sultan, C., Mol. Cell. Endocrinol. **129** (1), 17 (1997).

105 Tyagi, R. K., Lavrovsky, Y., Ahn, S. C., Song, C. S., Chatterjee, B., and Roy, A. K., Mol. Endocrinol. **14** (8), 1162 (2000).

106 Shaner, N. C., Campbell, R. E., Steinbach, P. A., Giepmans, B. N., Palmer, A. E., and Tsien, R. Y., Nat .Biotechnol. **22** (12), 1567 (2004).

107 Shaner, N. C., Steinbach, P. A., and Tsien, R. Y., Nat. Methods **2** (12), 905 (2005).

108 Powell, S. M., Christiaens , V., Voulgarak, i. D., Waxman, J., Claessens, F., and Bevan, C. L., Endocr-Relat. Cancer **11** (1), 117 (2004).

109 Blackwell Tk Kretzner, L. B. E. E. R. W. H., Science **250** (4984), 1149 (1990).

110 Blackwood Em Eisenman, R. N., Science **251** (4998), 1211 (1991).

111 Nilsson, J. A. and Cleveland, J. L., Oncogene **22** (56), 9007 (2003).

112 Cole, M. D. and Nikiforov, M. A., Curr. Top. Microbiol. Immunol. **302**, 33 (2006).

113 Amati, B., Littlewood , T., Evan, G., and Land, H., Embo J. **12** (13), 5083 (1993).

114 Inghirami, G., Grignani, F., Sternas, L., Lombardi, L., Knowles, D., and Dallafavera, R., Science **250** (4981), 682 (1990).

115 Arabi, A., Rustum, C., Hallberg, E., and Wright , A. P. H., J. Cell. Sci. **116** (9), 1707 (2003).

116 Marcu, K. B., Bossone, S. A., and Patel, A. J., Annu. Rev. Biochem. **61**, 809 (1992).

117 Harris, M. H. and Thompson, C. B., Cell. Death Differ. **7** (12), 1182 (2000).

118 Scorrano, L. and Korsmeyer, S. J., Biochem .Biophys. Res. Commun. **304** (3), 437 (2003).

119 Hann Sr Eisenman, R. N., Mol Cell Biol **4** (11), 2486 (1984).

120 Persson, H., Gray, H. E., and Godeau, F., Mol. Cell. Biol. **5** (11), 2903 (1985).

121 Mateyak, M. K., Obaya, A. J., Adachi, S., and Sedivy, J. M., Cell Growth Differ. **8** (10), 1039 (1997).

122 Tworkowski, K. A., Salghetti , S. E., and Tansey, W. P., Oncogene **21** (55), 8515 (2002).

123 Seksek, O., Biwersi, J., and Verkman, A. S., J. Cell. Biol. **138** (1), 131 (1997).

124 Mehmet, H., Littlewood, T. D., SinnettSmith, J., Moore, J. P., Evan, G. I., and Rozengurt, E., Cell Growth Differ. **8** (2), 187 (1997).

125 Mantulin, W. W. and Weber, G., J. Chem. Phys. **66** (9), 4092 (1977).

126 Barkley, M., Kowalczyk, A., and Brand, L., J. Chem. Phys. **75**, 3581 (1981).

127 Brand, L., Knutson, J. R., Davenport, L., Beechem, J. M., Dale, R. E., Walbridge, D. G., and Kowalczyk, A., in *Spectroscopy and the Dynamics of Molecular Biological Systems*, edited by R. E. Dale (Acad. Press, London, 1985), pp. 259.

128 Zinsli, P. E., Chem. Phys. **20**, 299 (1977).

129 Jas, G., Larson, E. J., Johnson, C. K., and Kuczera, K., J. Phys. Chem. A **104**, 9841 (2000).

130 Christensen, R. L., Drake, R. C., and Phillips, D., J. Phys. Chem. **90**, 5960 (1986).

131 Brocklehurst, B. and Young, R. N., J. Chem. Phys. **99**, 40 (1995).

132 Pauls, S. W., Hedstrom, J. F., and Johnson, C. K., J. Chem. Phys. **237**, 205 (1998).

133 Goldie, S. N. and Blanchard, G. J., Journal of Physical Chemistry A **103**, 999 (1999).

134 Jiang, Y. and Blanchard, G. J., J. Phys. Chem. **98**, 6436 (1994).

135 Wirth, M. J. and Chou, S.-H., J. Phys. Chem. **95**, 1786 (1991).

136 Einstein, A., *In investigations on the theory of the Brownian movement*. (Dover Publications, New York, 1956).

137 McQuarrie, D. A., *Statistical Mechanics*. (University Science Books, New York, 1973).

138 Hu, C.-M. and Zwanzig, R., J. Chem. Phys. **60**, 4354 (1974).

139 Tanford, C., *Physical Chemistry of Macromolecules*. (John Wiley and Sons, Inc, New York, 1961).

140 Stokes, G., Trans. Cambridge Phil. Soc. **8**, 287 (1847).

141 Perrin, F., J. Phys. Rad. **7**, 1 (1936).

142 Small, E. W. and Isenberg, I., Biopolymers **16**, 1907 (1977).

143 Chuang, T. J. and Eisenthal, K. B., J. Chem. Phys. **57**, 5094 (19972).

144 Ehrenberg, M. and Rigler, R., Chem. Phys. Lett. **14** (5), 539 (1972).

145 Brooks, B. R., Bruccoleri, R. E., Olafson, B. D., States, D. J., Swaminathan, S., and Karplus, M., J. Comput. Chem. **4**, 187 (1983).

146 Steinbach, P. J. and Brooks, B. R., J.Computational Chemistry **15** (7), 667 (1994).

147 Feller, S. E., Zhang, Y., Pastor, R. W., and Brooks, B. R., J. Chem. Phys. **103** (11), 4613 (1995).

148 Jimenez, R., Fleming, G. R., Kumar, P. V., and Marncelli, M., Nature **369**, 471 (1994).

149 Fillaux, F., Chem. Phys. Lett. **114** (4), 384 (1985).

150 Sarkar, N., Takeuchi, S., and Tahara, T., J. Phys. Chem. A **103**, 4808 (1999).

151 Szubiakowski, J., Balter, A., Nowak, W., Kowalczyk, A., Wisniewski, K., and Wierzbowska, M., Chem. Phys. **208**, 283 (1996).

152 Shilstone, G. N., Zannoni, C., and Verachini, C. A., Lig. Cryst. **6**, 303 (1989).

153 Frisch, M. J., Trucks, G. W., Schlegel, H. B., Scuseria, G. E., Robb, M. A., Cheeseman, J. R., Montgomery, J. A., Jr., T. V., Kudin, K. N., Burant, J. C., Millam, J. M., Iyengar, S. S., Tomasi, J., Barone, V., Mennucci, B., Cossi, M., Scalmani, G., Rega, N., Petersson, G. A., Nakatsuji, H., Hada, M., Ehara, M., Toyota, K., Fukuda, R., Hasegawa, J., Ishida, M., Nakajima, T., Honda, Y., Kitao, O., Nakai, H., Klene, M., Li, X., Knox, J. E., Hratchian, H. P., Cross, J. B., Adamo, C., Jaramillo, J., Gomperts, R., Stratmann, R. E., O. Yazyev, Austin, A. J., Cammi, R., Pomelli, C., Ochterski, J. W., Ayala, P. Y., Morokuma, K., Voth, G. A., Salvador, P., Dannenberg, J. J., Zakrzewski, V. G., Dapprich, S., Daniels, A. D., Strain, M. C., Farkas, O., Malick, D. K., Rabuck, A. D., Raghavachari, K., Foresman, J. B., Ortiz, J. V., Cui, Q., Baboul, A. G., Clifford, S., Cioslowski, J.,

Stefanov, B. B., Liu, G., Liashenko, A., Piskorz, P., Komaromi, I., Martin, R. L., Fox, D. J., Keith, T., Al-Laham, M. A., Peng, C. Y., Nanayakkara, A., Challacombe, M., Gill, P. M. W., Johnson, B., Chen, W., Wong, M. W., Gonzalez, C., and Pople, J. A., Gaussian (Gaussian Inc, Pittsburgh, PA, 2003).

154 Hoover, W. G., Phys. Review A **31** (3), 1695 (1985).

155 Fourmann, B., Jouvet, C., Tramer, A., Le Bars, J. M., and Millie, P., Chem. Phys. **92**, 25 (1985).

156 Schaftenaar, G. and Noordik, J. H., J.Comp.-Aided Mol. Design **14**, 123 (2000).

157 Zimmermann, H. and Joop, N., Elektrochem. Ber. Bunnsenges. Physik Chem. **65**, 138 (1961).

158 Zimmermann, H. and Joop, N., Elektrochem. Ber. Bunnsenges. Physik Chem. **64**, 1215 (1960).

159 Pigliucci, A. and Vauthey, E., Chimia **57**, 200 (2003).

160 Shen, X. and Knutson, J. R., Chem. Phys. Lett. **339**, 191 (2001).

161 Xu, J., Toptygin, D., Graver, K., Albertini, R., Savtchenko, R., Meadow, N., Roseman, S., Callis, P., Brand, L., and Knutson, J., Journal of the American Chemical Society **128** (4), 1214 (2006).

162 Xu, J. and Knutson, J. R., Biophys. J. **84**, B647 and manuscript (2003).

163 Xu, J., Chen, J.-J., King, J., Toptygin, D., Callis, P., Brand, L., and Knutson, J., in *52nd Annual Meeting of the Biophysical Society* (Long Beach, CA, 2008), Vol. Supp. 94, 1607-Pos.

164 Benda, A., Fagul'ova, V., Deyneka, A., Enderlein, J., and Hof, M., Langmuir **22** (23), 9580 (2006).

165 Ray, K., Zhang, J., and Lakowicz, J. R., Anal. Chem. **80** (19), 7313 (2008).

166 Gregor, I. and J., E., Photochem. Photobiol. Sci. **6** (1), 13 (2007).

167 Kapusta, P., Wahl , M., Benda, A., Hof, M., and J., E., J. Fluoresc. **17** (1), 43 (2007).

168 Felekyan, S., Kuhnemuth, R., Kudryavtsev, V., Sandhagen, C., Becker, W., and Seidel, C. A. M., Rev. Sci. Instrum. **76** (8) (2005).

169 Bohmer, M., Wahl, M., Rahn, H. J., Erdmann, R., and Enderlein, J., Chem. Phys. Lett. **353** (5-6), 439 (2002).

170 Humpolickova, J., Beranova, L., Stepanek, M., Benda, A., Prochazka, K., and Hof, M., J. Phys. Chem. B **112** (51), 16823 (2008).

171 Nettels, D., Hoffmann, A., and Schuler, B., J. Phys. Chem. B **112** (19), 6137 (2008).

172 Lleres David Swift Samuel Lamond Angus, I., Curr Protoc Cytom **Chapter 12**, Unit12 (2007).

173 Schatzel, K. and Peters, R., Proc. SPIE **1430**, 109 (1991).

174 Becker, W., *Advanced Time-Correlated Single Photon Counting Techniques*. (Springer, New York, 2005).

175 Park Dh Plapp, B. V., J Biol Chem **266** (20), 13296 (1991).

176 Plapp, B. V., J. Biol .Chem. **245** (7), 1727 (1970).

177 Hawkins, M. E., Pfleiderer, W., Balis, F. M., Porter, D., and Knutson, J. R., Anal. Biochem. **244** (1), 86 (1997).

178 Rusinova, E., Tretyachenko-Ladokhina, V., Vele, O. E., Senear, D. F., and Ross , J. B. A., Anal. Biochem. **308** (1), 18 (2002).

179 Gafni, A., Biochemistry **18** (8), 1540 (1979).

180 Bialik, C. N., Wolf, B., Rachofsky, E. L., Ross, J. B. A., and Laws, W. R., Biophys. J. **75** (5), 2564 (1998).

181 Gafni, A. and Brand, L., Biochemistry **15** (15), 3165 (1976).

182 Knutson, J. R., Walbridge, D. G., and Brand, L., Biochemistry **21** (19), 4671 (1982).

183 Kierdaszuk, B., Malak, H., Gryczynski, I., Callis, P., and Lakowicz , J. R., Biophys Chem **62** (1-3), 1 (1996).

184 Kierdaszuk, B., Malak, H., Gryczynski, I., Callis, P., and Lakowicz, J. R., Biophys. Chem. **62** (1-3), 1 (1996).

185 Moiroux, J. and Elving, P. J., J. Am. Chem. Soc. **102** (21), 6533 (1980).

186 Wu, Z. Y., Jing, W. G., and Wang, E., Electrochem. Commun. **1** (11), 545 (1999).

187 Katilius, E. and Woodbury, N. W., J. Biomed. Opt. **11** (4) (2006).

188 Bolten, M., Niermann, M., and Eime, r. W., Biochemistry **38** (38), 12416 (1999).

189 Pons, T., Moreaux, L., and Mertz , J., Phys. Rev. Lett. **89** (28) (2002).

190 Dombeck, D. A., Blanchard-Desce, M., and Webb, W. W., J. Neurosci. **24** (4), 999 (2004).

191 Barad, Y., Eisenberg, H., Horowitz, M., and Silberberg, Y., Appl. Phys. Lett. **70** (8), 922 (1997).

192 Muller, M., Squier, J., Wilson, K. R., and Brakenhoff, G. J., J .Microsc.-Oxf. **191**, 266 (1998).

193 Tolles Wm Nibler Jw Mcdonald Jr Harvey, A. B., Appl Spectrosc **31** (4), 253 (1977).

194 Volkmer, A., Cheng, J. X., and Xie, X. S., Phys. Rev. Lett. **87** (2) (2001).

195 Volkmer, A., J. of Phys. D: App. Phys. **38** (5) (2005).

196 Cheng, J. X., Volkmer, A., Book, L. D., and Sunney Xie, X., J. Phys. Chem. B **105** (7), 1279 (2001).

197 Ganikhanov, F., Evans, C. L., Saar, B. G., and Xie, X. S., Opt. Lett. **31** (12), 1872 (2006).

198 Cheng, J. X. and Xie, X. S., J. Phys. Chem. B **108** (3), 827 (2004).

199 Schie, I. W., Weeks, T., McNerney, G. P., Fore, S., Sampson, J. K., Wachsmann-Hogiu, S., Rutledge, J. C., and Huser, T., Opt. Express **16** (3), 2168 (2008).

200 Abbe, E., Arch. Mikr. Anat. **9**, 413 (1873).

201 Born, M. and Wolf, E., *Principles of Optics: Electromagnetic Theory of Propagation, Interference and Diffraction of Light*, 7th ed. (Cambridge University Press, Cambridge, 1999).

202 Dyba, M., Keller, J., and Hell, S. W., New. J. Phys. **7** (2005).

203 de Jonge, N., Peckys, D. B., Kremers, G. J., and Piston, D. W., Proc. Natl. Acad. Sci. U. S. A. **106** (7), 2159 (2009).

204 Rittweger, E., Rankin, B. R., Westphal, V., and Hell, S. W., Chem. Phys. Lett. **442** (4-6), 483 (2007).

205 Klar, T. A., Jakobs, S., Dyba, M., Egner, A., and Hell, S. W., Proc. Natl. Acad. Sci. U. S. A. **97** (15), 8206 (2000).

206 Willig, K. I., Kellner, R. R., Medda, R., Hein, B., Jakobs, S., and Hell, S. W., Nat. Methods **3** (9), 721 (2006).

207 Schroder Jan Benink Helene Dyba Marcus Los Georgyi, V., Biophys J **96** (1), L1 (2009).

208 Fouquet, W., Owald, D., Mertel, S., Kellner, R., Dyba, M., and Sigrist, S. J., J. Neurogenet. **23**, V15 (2009).

209 Willig, K. I., Rizzoli, S. O., Westphal, V., Jahn, R., and Hell, S. W., Nature **440** (7086), 935 (2006).

210 Alberts, B., Bray, D., Lewis, J., Raff, M., Roberts, K., and Watson, J. D., *Molecular Biology of the Cell*, 3rd ed. (Garland Publishing, New York, NY, 1994).

211 Blinova, K., Carroll, S., Bose, S., Smirnov , A. V., Harvey, J. J., Knutson, J. R., and Balaban, R. S., Biochemistry **44** (7), 2585 (2005).

212 Potma, E. O., de Boeij, W. P., van Haastert, P. J. M., and Wiersma , D. A., Proc. Natl. Acad. Sc.i U. S. A. **98** (4), 1577 (2001).

213 Shen, Y. R., *The Principles of Nonlinear Optics*. (John Wiley and Sons Inc., New York, 1984).

214 Cheng, J. X., Volkmer, A., and S., X. X., J. Opt. Soc. Am. B - Opt. Phys. **19** (6), 1363 (2002).

215 Griffiths, D. J., *Introduction to Quantum Mechanics*. (Prentice-Hall, Inc, Englewood Cliffs, New York, 1995).

216 Atkins, P., *Physical Chemistry*, 5th ed. (W.H. Freeman and Company, New York, 1994).

217 Einstein, A., Phys. Z. **18**, 121 (1917).

218 Schonle, A., Keller, J., Hark, B., and Hell, S. W., in *Handbook of Biomedical nonliar optical microscopy*, edited by B. R. Masters and P. T. C. So (Oxford University Press, Oxford, 2008).

219 Hell Sw Wichmann, J., Opt Lett **19** (11), 780 (1994).

220 Yue Kt Martin Cl Chen, D. N. P. S. D. C. R., Biochemistry **25** (17), 4941 (1986).

221 Rittweger, E., Han, K. Y., Irvine, S. E., Eggeling, C., and Hell, S. W., Nat. Photonics **3** (3), 144 (2009).

222 Fernandez-Suarez, M. and Ting , A. Y., Nat. Rev. Mol. Cell. Biol. **9** (12), 929 (2008).

223 Freudiger, C. W., Min, W., Saar, B. G., Lu, S., Holtom, G. R., He, C. W., Tsai, J. C., Kang, J. X., and Xie, X. S., Science **322** (5909), 1857 (2008).

224 Royer, C. A., Smith, W. R., and Beechem, J. M., Anal Biochem **191**, 287 (1990).

225 Royer, C. A. and Beechem, J. M., Methods in Enzymology **210**, 481 (1992).

226 Heilweil, E. J. and Hochstrasser, R. M., J. Chem. Phys. **82** (11), 4762 (1985).

227 Walczak, W. J., Xiao, J. M., Kopetz, E. S., Lease, K., Grau, H., Lee, S. P., Han, M. K., and Knutson, J. R., Biophys. J. **72/2**, A201 (1997).

228 Hu, M., Petrova, H., and Hartland, G. V., Chem. Phys. Lett. **391** (4-6), 220 (2004).

229 Pustovalov, V. K., Chem. Phys. Lett. **421** (1-3), 142 (2006).

230 Govorov, A. O., Zhang, W., Skeini, T., Richardson, H., Lee, J., and Kotov, N. A., Nanoscale Res. Lett. **1** (1), 84 (2006).

231 Jin, R. C., Wu, G. S., Li, Z., Mirkin, C. A., and Schatz, G. C., J. Am. Chem. Soc **125** (6), 1643 (2003).

232 Jain, P. K., Qian, W., and El-Sayed, M. A., J. Am. Chem. Soc. **128** (7), 2426 (2006).